SANTA CATARINA STATE UNIVERSITY – UDESC
JOINVILLE COLLEGE OF ENGENEERING – CCT
MECHANICAL ENGINEERING GRADUATE PROGRAM – PPGEM

VALÉRIA FARIAS DA LUZ

TOPOLOGY OPTIMIZATION OF COMPLIANT MECHANISMS IN HARMONIC REGIME

JOINVILLE
2024

VALÉRIA FARIAS DA LUZ

TOPOLOGY OPTIMIZATION OF COMPLIANT MECHANISMS IN HARMONIC REGIME

Master's Thesis submitted to the Mechanical Engineering Graduate Program at the Joinville College of Engeneering of Santa Catarina State University in fulfillment of the partial requirement for the Master's degree in Mechanical Engineering, area: Numerical Modeling and Simulation.

Adviser: Prof. Dr. Eduardo Lenz Cardoso.
Co-Adviser: Dr. Olavo M. Silva.

JOINVILLE
2024

VALÉRIA FARIAS DA LUZ

TOPOLOGY OPTIMIZATION OF COMPLIANT MECHANISMS IN HARMONIC REGIME

Master's Thesis submitted to the Mechanical Engineering Graduate Program at the Joinville College of Engeneering of Santa Catarina State University in fulfillment of the partial requirement for the Master's degree in Mechanical Engineering, area: Numerical Modeling and Simulation.

Adviser: Prof. Dr. Eduardo Lenz Cardoso.
Co-Adviser: Dr. Olavo M. Silva.

BANCA EXAMINADORA:

Prof. Dr. Eduardo Lenz Cardoso (presidente/orientador)
Universidade do Estado de Santa Catarina
Departamento de Engenharia Mecânica

Prof. Dr. Renato Pavanello
Universidade Estadual de Campinas

Prof. Dr. Carlos Eduardo De Souza
Universidade Federal de Santa Maria

Joinville, 19 de abril de 2024

ACKNOWLEDGEMENTS

The author would like to express the following acknowledgments:

To God for His constant support and blessings throughout my master's journey. His grace has been my strength, guiding me through challenges and illuminating my path.

To my father, Sergio Almeida da Luz, for being a wonderful father. Despite his physical absence, I express my deepest gratitude for his unwavering love, encouragement, and belief in my. His enduring presence in my heart continues to inspire and guide me, and I am forever grateful for the values and lessons he imparted upon me.

To my dear family, Nilva Medianeira Farias da Luz and Rosana Farias da Luz, for being my example of resilience and determination. Thank you for your patience, love, and support throughout my life.

To my dear fiancé, Lucas Henrique dos Santos Tavares, for being my safe haven and for all the support and love during these 4 years of dedication. Without you, I would not have been able to succeed.

To Prof. Eduardo Lenz Cardoso, for sharing so much of his knowledge and time with me, for all the support and guidance during the development of this research. To Dr. Olavo M. Silva, co-advisor, for accepting this challenge alongside us, enriching the analyses contained herein with great knowledge and expertise.

To my friends, Ana Carolina Nunes Duarte and Thamiris Lima Costa for all their patience in listening to my fears and frustrations during the final stretch of this work. In particular, I would like to express my gratitude to Verônica Caroline Herbst Pazda, a friend who began as a sister in our research group and evolved into a lifelong confidante.

To WEG and SENAI Innovation Institute for Manufacturing Systems, for supporting the development of this work, believing in the importance of the graduation and understanding the importance of this work.

To the Santa Catarina State University, specially to Mechanical Engineering Department in Joinville, and all the professors and professionals responsible for providing a high quality education.

ABSTRACT

Compliant mechanisms (CMs) are used to modify kinematic and/or kinetic relations by connecting actuators (inputs) and receptors (outputs) according to design requirements. Unlike traditional mechanisms, they do not have rigid body connectors (hinges), and their movements are solely due to elastic deformation, allowing a significant reduction in the number of parts. Determining the geometry of CMs may be too complex for traditional design methods, specially for complex modes of actuation. Therefore, optimization techniques are commonly used instead. The key aspects of using optimization to design compliant mechanisms is the proper definition of the objective function and functional constraints.

Among the many approaches to use optimization to the design of CMs is the Topology Optimization (TO). Most works in this field consider static equilibrium, however, many applications involve CMs subjected to non-static excitation. Thus, this work proposes a new formulation that takes into account the harmonic behavior in the TO of continuous structures. The goal is to maximize the harmonic amplitude of output displacements, such that a new objective function is proposed. The optimization problem also has constraints in the input displacements, the total amount of material (volume) and local harmonic stresses. An adaptive volume limit, recently proposed in the literature, is investigated to adjust the volume constraint.

The Augmented Lagrangian (AL) method is used to account for a large number of local stress constraints. The optimization problem is solved using the Globally Convergent Method of Method of Moving Assymptotes (GCMMA). The traditional Solid Isotropic Material with Penalization (SIMP) approach is used as a material model for stiffness, and a modified version is used to model mass. Singularities in stress parametrization are addressed by the QP relaxation.

Spatial filtering and nonlinear projection are used for complexity control and regulatization. Analytical sensitivities are obtained using the extended adjoint approach for harmonic problems. In this work, the design of an inverter mechanism is used to study the proposed formulation. The results demonstrate that the formulation is capable of generating mechanisms with continuous material distributions in lower frequencies, satisfying the constraints, minimizing the objective, and performing the required phase inversion in the inverter problem. Finally, the results present comparisons among different input parameters (constraints, design variables, and adjustment factors) and illustrate the sensitivity of the formulation to each defined parameter set.

Keywords: Optimization; Harmonic regime; Compliant mechanisms; Adaptive volume constraint.

RESUMO

Mecanismos flexíveis (CMs) são usados para modificar relações cinemáticas e/ou cinéticas conectando atuadores (entradas) e receptores (saídas) de acordo com os requisitos do projeto. Ao contrário dos mecanismos tradicionais, não possuem conectores de corpo rígido (dobradiças) e seus movimentos se devem unicamente à deformação elástica, o que permite uma redução significativa no número de componentes. Determinar a geometria dos CMs pode ser muito complexo para métodos de projeto tradicionais, especialmente para modos complexos de atuação. Portanto, técnicas de otimização são comumente usadas. Os principais aspectos do uso da otimização para projetar CMs são a definição adequada da função objetivo e das restrições.

Dentre as diversas abordagens para utilização da otimização no projeto de CMs está a Otimização Topológica (TO). A maioria dos trabalhos nesta área considera o equilíbrio estático, porém, muitas aplicações envolvem CMs submetidos a excitação não estática. Assim, este trabalho propõe uma nova formulação que leva em consideração o comportamento harmônico no TO de estruturas contínuas. O objetivo é maximizar a amplitude harmônica dos deslocamentos de saída, de modo que uma nova função objetivo seja proposta. O problema de otimização também possui restrições nos deslocamentos de entrada, na quantidade total de material (volume) e nas tensões harmônicas locais. Um limite de volume adaptativo, recentemente proposto na literatura, é investigado para ajustar a restrição de volume.

O método Lagrangiano Aumentado (AL) é usado para incluir o grande número de restrições de tensão locais. O problema de otimização é resolvido usando o Método Globalmente Convergente do Método de Assíntotas Móveis (GMMA). A abordagem tradicional de Material Isotrópico Sólido com Penalização (SIMP) é usada como modelo de material para rigidez, e uma versão modificada é usada para modelar massa. Singularidades na parametrização de tensão são abordadas pelo relaxamento QP.

Filtragem espacial e projeção não linear são usadas para controle de complexidade. As sensibilidades analíticas são obtidas usando a abordagem adjunta estendida para equações de equilíbrio harmônico. O projeto de um mecanismo inversor é utilizado para estudar a formulação proposta. Os resultados demonstram que a formulação foi capaz de gerar mecanismos com distribuições contínuas de materiais em frequências mais baixas, satisfazendo as restrições, minimizando o objetivo e realizando a inversão de fase necessária no problema do inversor. Finalmente, os resultados apresentam comparações entre diferentes parâmetros de entrada e ilustram a sensibilidade da formulação a cada conjunto de parâmetros definido.

Palavras-chave: Otimização; Regime harmônico; Mecanismos flexíveis; Restrição de volume adaptativa.

LIST OF FIGURES

LIST OF TABLES

LIST OF ABBREVIATIONS AND ACRONYMS

AL   Augmented Lagrangian

CM   Compliant Mechanisms

FEM   Finite Element Method

GA   Geometrical Advantage

GCMMA   Globally Convergent Method of Moving Assymptotes

KKT   Karush-Kuhn-Tucker

MA   Mechanical Advantage

ME   Mechanical Efficiency

MMA   Method of Moving Asymptotes

RB   Rigid-Body

SIMP   Solid Isotropic Material with Penalization

TO   Topology Optimization

LIST OF SYMBOLS

α	Mass proportional damping constant
β	Stiffness proportional damping constant
$\boldsymbol{\varepsilon}$	Infinitesimal strain tensor
$\dot{\boldsymbol{\varepsilon}}$	Rate of strain tensor
$\boldsymbol{\mu}$	Vector of KKT multipliers corresponding to the inequality constraints
γ	Specific mass of the material
ρ_l	cutoff value for the mass parametrization
$\boldsymbol{\rho}$	Vector of relative densities
ρ_e	Relative density of element e
$\bar{\sigma}$	Yield limit for the base material
$\boldsymbol{\sigma}$	Cauchy stress tensor
ω	Angular frequency of excitation
$\mathbf{b}$	Vector of body forces
$\mathbf{c}$	Penalization vector
$\mathbf{C}$	Damping matrix
$\mathbf{D}$	Constitutive tensor of the linear elastic material
f	Objective function
$\mathbf{H}$	Global-local transformation matrix
i	Complex component
$\mathbf{K}$	Static stiffness matrix
$\mathbf{K_D}$	Dynamic stiffness matrix
$\mathbf{L}$	Linear operator
L	Augmented Lagrangian Function
m	Number of constraints
$\mathbf{M}$	Mass matrix
n	Number of design variables
n_e	Number of elements
$\mathbf{N}$	Matrix of shape functions
p	Penalty exponent for the SIMP model for material
q	Penalty exponent for the SIMP model for stress

r_c	Penalty increase rate
r_f	Objective function adjustment factor
r_v	Rate of decrease in volume fraction limit
u_{in}	Input displacement
$\bar{u}_{in}$	Upper bound in the input displacement
u_{out}	Output displacement
$\mathbf{u}(t)$	Displacement vector
$\ddot{\mathbf{u}}(t)$	Acceleration vector
$\dot{\mathbf{u}}(t)$	Velocity vector
$\bar{v}$	Upper bound in volume constraint
$\mathbf{x}$	Vector of design variables

CONTENTS

1 INTRODUCTION

A mechanism is a device that converts input force and/or motion into output force and/or motion (HOWELL, 2001). There are two main types of mechanisms: rigid and flexible. Rigid mechanisms, the most common type, typically include movable components like gears, belts, cams, and bearings. Compliant mechanisms (CM), have been used by humans for centuries, predating the use of joints and other mechanical connecting elements. Unlike rigid mechanisms, compliant mechanisms achieve motion through the deformation of their flexible components (ZHU et al., 2020). They offer two key advantages over conventional rigid-link counterparts: the absence of relative motion among the components and the absence of overlapping elements (GALLEGO; HERDER, 2009).

The lack of relative motion eliminates sliding friction, addressing concerns such as wear, noise, and vibration, while also eliminating the need for lubrication. This results in lower maintenance requirements. Additionally, the absence of backlash reduces positioning errors, enhancing precision. The absence of overlapping elements reduces the number of parts, allowing single-piece production, simplifying assembly and reducing overall weight.

As a result, these characteristics promote compactness, miniaturization, and economic efficiency. Therefore, the component is well-suited for implementation in microscale or nanoscale manipulation systems (ZHU et al., 2020). Overall, these benefits encourage the exploration of more innovative designs and actuation arrangements, expanding the range of potential solutions (GALLEGO; HERDER, 2009).

There are various approaches to design CMs, as depicted in Figure 1: kinematic, building blocks, and structural optimization. Kinematic synthesis, explored in the early 1990s by authors such as Her and Midha (1987), Murphy, Midha and Howell (1996), and Howell and Midha (1994), leverages knowledge from Rigid-Body (RB) mechanisms to create CMs. This approach involves two primary methods: RB replacement and Freedom And Constraints Topologies (FACT). Rigid-Body replacement entails identifying a rigid body mechanism that fulfills the desired function and then transforming it into a compliant version (GALLEGO; HERDER, 2009). FACT is based on mapping a set of geometric entities in the freedom space to a constraint space, where the solution to the design problem can be found.

Figure 1 – Synthesis of Compliant Mechanisms.
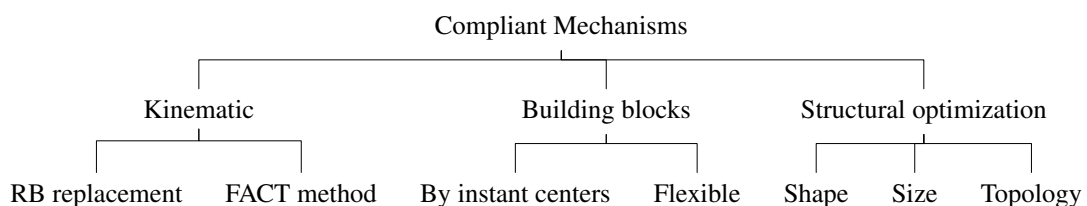
Source: Author production.

The building block concept is founded on the notion that a mechanism should consist of various sub-mechanisms, referred to as building blocks (ZHU et al., 2020). These building

blocks are designed based on simple functions, and by combining multiple CMs, it becomes possible to create a mechanism capable of performing more complex functions. The building blocks by instant centers is a conceptual design procedure that involves finding a mechanism capable of delivering a specified input displacement to the output with a desired displacement direction and geometric advantage. In the Flexible building block method, each building block possesses its characteristic stiffness matrix, formed by assembling the stiffness matrices of all the elements constituting the building block.

Optimization involves maximizing or minimizing a functional while respecting a set of constraints, by adjusting a set of design variables. When these variables and functions belong to structural quantities, the term "structural optimization" is used. This is the third approach to designing a CM.

Structural optimization can be carried out through three distinct approaches: shape, size, and topology. Shape optimization involves finding the optimal boundary within a fixed topology to extremize a given objective and best satisfy the functional constraints. In size or parametric optimization, the aim is to identify the optimal set of sizing variables (such as thickness, cross-section, diameters, etc.) in a predefined design that extremizes the objective function and fulfills the constraints (GALLEGO; HERDER, 2009).

Topology optimization (TO), the main focus of this study, is an approach that identifies the optimal material distribution within a fixed design domain. This distribution aims to minimize a given cost function while respecting a set of constraints (ZHU et al., 2020). A key strength of topology optimization lies in its flexibility to generate unconventional design solutions, as the consideration of material distribution expands the solution space when compared to both the shape and the parametric optimizations.

Figure 2 illustrates a simplified flowchart highlighting key aspects of topology optimization applied to the design of CMs. The objective function, the function undergoing extremization, is a crucial aspect. In the context of TO for CMs, it is noteworthy that there is no universally accepted objective function (ZHU et al., 2020). Therefore, each problem must have its own objective function and for its construction, a series of methodologies have been proposed over the years.

A comparative study by Deepak, Dinesh and Ananthasuresh (2008) explores five different formulations for TO of CMs. The approaches outlined in Figure 2 are among the most relevant. Mutual Strain Energy (MSE) and Strain Energy (SE) are combined to create a mechanism that is rigid to resist external forces and compliant to allow desired deformations, using a weighted linear combination. This formulation is employed in the works of (ANANTHASURESH; KOTA; GIANCHANDANI, 1994; NISHIWAKI et al., 1998).

Other possibility is to create an objective function to maximize the ratio of a parameter between the two regions of interest of the domain (input and output). This is the main idea for Geometrical Advantage (GA), a relationship between displacement (LARSEN; SIGMUND; BOUWSTRA, 1997a); Mechanical Efficiency (ME), relationship between work and Mechanical

Figure 2 – Topology optimization of compliant mechanisms.
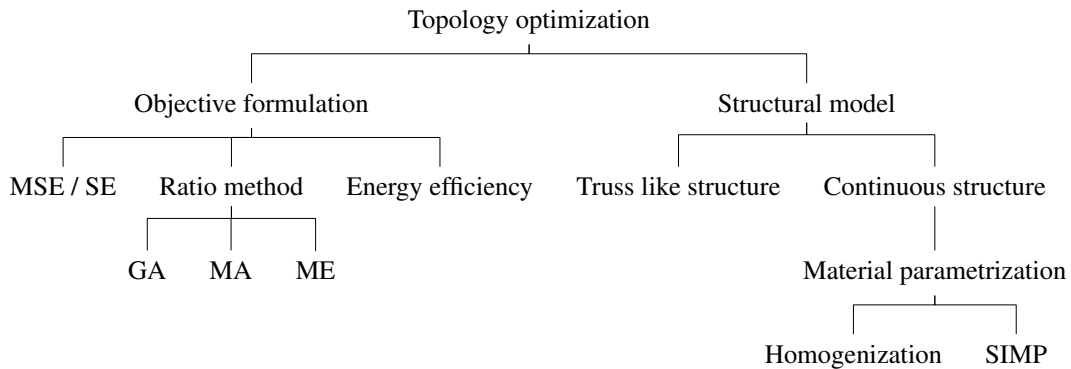
Source: Author production.

Advantage (MA), relationship between forces (LARSEN; SIGMUND; BOUWSTRA, 1997b).

Another group of studies use the concept of effective energy, addressing the compliant mechanism as an energy transformation device. The energy efficiency formulation calculates the ratio of the net energy transferred at the output to the net energy supplied at the input (HETRICK; KOTA, 1999). This transformation involves converting input force from the external environment into output deformation. The objective is to maximize effective energy, representing the efficiency of the mechanism's energy conversion (MIYAJIMA; NOGUCHI; YAMADA, 2022; DING et al., 2021; ZHU et al., 2020).

The structural model, in Figure 2, refers to the structural model used. This can be either discrete (one-dimensional beam or bar)(LARSEN; SIGMUND; BOUWSTRA, 1997b; FRECKER et al., 1997) or continuous (2D or 3D).

In the design of compliant mechanisms using continuum structures, two highlighted material parameterization models are the homogenization method and the Solid Isotropic Material with Penalization (SIMP) method. The homogenization method describe the material property by using microstructures, or unit cells, where the amount of material and its mechanical properties are functions of the geometry and the orientating of the unit cell (BENDSØE; KIKUCHI, 1988). The SIMP method is based on the rule of mixtures of two isotropic materials (base material and a weak phase) (BENDSØE; SIGMUND, 1999). In the current study, the SIMP approach will be used, alongside other forms of mass and stiffness parameterization, which will be further explained in the subsequent chapters.

After outlining various methods for developing compliant mechanisms, it's crucial to address the operating conditions of the component. Concerning the type of loading, TO of CMs has predominantly been applied to static design scenarios. However, few studies acknowledge that many mechanical applications involve varying loads over time, such as the rotation of electrical machinery, deformation of aircraft wings during flight, or even the resonance of a guitar string when played. An instance of dynamic loading is harmonic excitation, characterized by loading with constant amplitude, modulated by a periodic function of fixed frequency.

Designing a structure using the TO method under harmonic regime requires adjustments

to mass, stiffness and damping to achieve specific objectives. This adjustment aims to bring the resonance frequency closer to the fixed excitation frequency when the goal is to increase the amplitude of the dynamic response (maximization of frequency response), (MONTERO; SILVA; CARDOSO, 2020), or move the design away from it when the goal is to reduce the amplitudes (minimization of frequency response, as in (SHU et al., 2011)).

Reducing vibration response aims to prevent structural damage to the system, typically to avoid structural resonance and minimize vibration levels. Conversely, amplification mechanisms, achieved by maximizing dynamic response, find application in energy absorption systems or amplification of small amplitudes, like in piezoelectric actuators. In such systems, the mechanism amplifies displacement, strains or relative movement to facilitate energy absorption or exploit geometric advantages arising from motion combinations.

The focus of this study will be on the latter, where a compliant mechanism exposed to harmonic loading aims to establish the maximization of a displacement relation between two or more given points in the system for a specified frequency of interest.

While the majority of TO studies in the literature focus on the static regime (KANG; CHOI; PARK, 2001; JUNG; PARK, 2015; LEE; PARK, 2015; PARK, 2010); there has been a growing of research on the dynamic regime in recent years (VENINI, 2016; YANG; LI, 2012; YANG; LI, 2013; ZHU et al., 2017). As highlighted by Montero, Silva and Cardoso (2020), there is no singular methodology universally employed for TO of dynamic problems, be it modal, harmonic or transient. Harmonic analysis, the specific focus of this work, is employed when seeking to obtain the steady-state response of a structure subjected to periodic loading.

The study of topology optimization under harmonic regime began with Ma, Kikuchi and Hagiwara (1993), where the concept of dynamic compliance was introduced, in contrast to the widely used concept of static compliance. Min et al. (1999) obtained a minimum average value of dynamic compliance for different frequencies. Tcherniak (2002) revealed the occurrence of discontinuity problems when using only dynamic compliance, hence the need for the application of static compliance as a design constraint. Additionally, this work also introduced an external damper to prevent disconnection between structures. Olhoff and Du (2009) used the SIMP method to maximize the natural frequency or the interval between two consecutive natural frequencies of the structure using modal analysis. Zhang, Kang and Zhang (2016) applied robust TO concepts to account for uncertainties in harmonic excitation values and minimal dynamic compliance in their formulation.

Few works address the maximization of the harmonic response. Montero, Silva and Cardoso (2020) used a weight density norm to formulate the harmonic problem, for both minimization and maximization of the harmonic response. This norm allows the association of dynamic measures without considering any energy concept. They also discuss the need to maintain the static compliance in the formulation (weighted objective function considering the static compliance) to avoid disconnected structures and to also mitigate the instability of the derivatives when the harmonic frequency is the close to the resonance. Silva (2017) linked

dynamic flexibility to input power functions to design resonant structures.

As presented by Ma, Kikuchi and Hagiwara (1993), in the dynamic case, the derivatives of the objective and constraints may abruptly change sign during the optimization iterations. This phenomenon was also reported by Silva (2017), who observed intermittent changes in the sign of the derivatives when the optimized system is located to the left or to the right of a resonance frequency. The instability of the response near the resonance frequency can be mitigated through numerical control of the damping factor (VALENTINI; SILVA; CARDOSO, 2021; GIRALDO-LONDOÑO; AGUILÓ; PAULINO, 2021). Another option, presented by Al-Bazoon and Arora (2022), is to work with a partitioned algorithm: in the initial optimization cycles, simplifications of the model are made by transforming dynamic loads into equivalent static loads. After stabilizing the model, dynamic loads return to the formulation.

Compliant Mechanism design methods using TO generally rely on mechanisms with localized flexibility, causing localized stresses in these regions. Particularly for (near) resonant structures, stress levels are incorporated into the analysis as constraints during the optimization process, ensuring that the resulting structure can withstand the specified design loads. This becomes one of the most important constraints in the design of resonant structures and even more relevant in the design of a CM, where the objective is to maximize flexibility. One of the first works to describe the geometric change caused by the inclusion of stress constraints was Kirsch (1989), for truss-like structures, introducing the concept of stress singularity (degenerate sub-domains containing the optimal response). This problem was further discussed by Guo and Cheng (1997), Duysinx and Bendsøe (1998), Bruggi (2008) where it is shown that, as the design variables approach zero, the stress remains unchanged, thus preventing material removal from the domain. To allow "cleaning" the domain, some relaxation techniques were proposed, such as ε relaxation (GUO; CHENG, 1997) and qp relaxation (BRUGGI, 2008).

Furthermore, other specifics such as local stress constraints are also altered when the harmonic regime is addressed. In this case, the stress constraint should account for a consistent stress model, as the viscous behavior associated to the proportional damping model (damped stress, Section 2). Other very relevant issue associated to stress is the large number of local stress constraints, as stress is a local measure. This problem is usually addressed by aggregation techniques or by using the Augmented Lagragian approach (PEREIRA; CARDOSO, 2018).

Regardless of the chosen approach, a common and widely debated issue in the design of CM using TOP is the presence of hinges. In these locations, there is rotation around a small portion of the domain, detracting from the idea of a compliant mechanism having distributed flexibility. This fact makes the CM more similar to a rigid mechanism and increases local stresses. Therefore, an alternative is the inclusion of stress constraints (PEREIRA; CARDOSO, 2018; MIYAJIMA; NOGUCHI; YAMADA, 2022; STANKIEWICZ; DEV; STEINMANN, 2022). In addition, filtering is also a resource used in Pereira and Cardoso (2018) and Rodriguez et al. (2020), where the mechanism is prevented from having very thin regions in its domain, reducing stress concentration. Another extension in the formulation, aimed at suppressing hinges, involves

determining minimum dimensions for regions of concentrated flexibility (ZHANG; ZHONG; GUO, 2014). However, none of the mentioned approaches completely eliminates the presence of hinges, generating mechanism with distributed compliance. Instead, mechanisms with *de facto* hinges may emerge (SELTMANN; HASSE, 2023).

With the aim of eliminating hinges, several robust optimization proposals have been presented. Cardoso, Silva and Beck (2019) introduced a robust optimization method based on the variation of stiffness of the output springs, while Sigmund (2009) incorporated manufacturing uncertainties into their formulation, employing image processing operators (erode and dilate) for this purpose. Finally, Zhan and Luo (2019) developed a formulation based on minimizing the variation of output displacement under constraints of mean displacement and volume. The three methodologies have shown results indicating that increased structural stiffness of the compliant mechanism is accompanied by the disappearance of *de facto* hinges.

In most works on CM using TO, the constraint volume during synthesis is limited to a constant value. Typically, optimization approaches tend to accumulate a large amount of material in certain areas during the synthesis of Compliant Mechanisms (CMs) to make them nearly rigid. Compliance is then concentrated in smaller areas. In contrast to the known fixed volume constraint in CM topology optimization, an adaptive volume constraint is introduced in Seltmann and Hasse (2023), which aims to eliminate regions of concentrated flexibility. This proposal is also investigated in the present work.

1.1 CONTRIBUTION

This work concatenate three different topics: design of compliant mechanisms, topology optimization and harmonic loads. This combination poses several challenges. According to Zhao and Wang (2023), when it comes to the design of CMs, there are still several important challenges related to static behavior, such as highly nonlinear behavior, a large number of local stress constraints as well as singularity phenomena of stress parameterization. Regarding harmonic behavior, one can also add difficulties associated to the proper definition of the "real" measures needed to formulate the optimization problem, physical/numerical issues associated to resonances and mass parameterization (to cite just a few). Although not directly addressed in this work, the consideration of harmonic behavior and consistent local stress measures allows for the investigation of fatigue constraints.

The main highlights in this work are:

- design of Compliant Mechanisms under low-frequency harmonic regime;

- use of consistent local harmonic stress constraints;

- investigation of a new harmonic objective function with directional information;

- investigation of the adaptive volume constraint proposed by (SELTMANN; HASSE, 2023).

1.2 COMPUTATIONAL IMPLEMENTATION

The formulation developed in this work is implemented as a computer code using the Julia language (BEZANSON et al., 2017). Some parts of the code were implemented by the author, like the objective function, constraints, Augmented Lagrangian and sensitivity analysis. Other parts use the following third part libraries:

- Finite element code uses LFEM.jl package (CARDOSO, 2023a);

- Solution of linear systems of equations use the LinearSolve package. Thus, it is possible to choose among many different solvers (RACKAUCKAS, 2022);

- The Globaly Convergent Moving Asymptote method, GCMMA, Svanberg (2002), is from the NLopt package (JOHNSON, 2007);

- Filters and projections are from the LFilter.jl package (CARDOSO, 2023b);

- Visualization is performed by using Gmsh post processor (GEUZAINE; REMACLE, 2020).

The computer implementation, in its current form, is not meant to be fast. Nonetheless, it is possible to optimize some parts (mainly by reusing pre computed matrices) to speed up the execution.

1.3 THESIS OUTLINE

Chapter 1 offers a comprehensive overview and primary motivation behind the development of this work. Additionally, it presents a summary of the history of studies pertaining to the topics under evaluation, emphasizing the most significant methods and findings of the referenced works.

Chapter 2 begins by introducing the theoretical foundation. It offers an overview of elastodynamics and general optimization, followed by defining the main concepts of topology optimization.

The proposed formulation is presented in Chapter 3. This chapter presents the objective function proposed in this work, the constraints, the optimization approach combining the GCMMA with the Augmented Lagrangian method and the sensitivity analysis.

The results of the design cases considered in this work are presented and evaluated in Chapter 4. Finally, the work in concluded and suggestions for future research are presented in Chapter 5.

2 THEORETICAL FOUNDATION

This section aims to present a summary of the theoretical foundation used to develop this work. To this end, this section is divided into three subsections: elastodynamics, general optimization and topology optimization. These steps are shown in the Figure 3

Figure 3 – Synthesis of Theoretical Foundation.
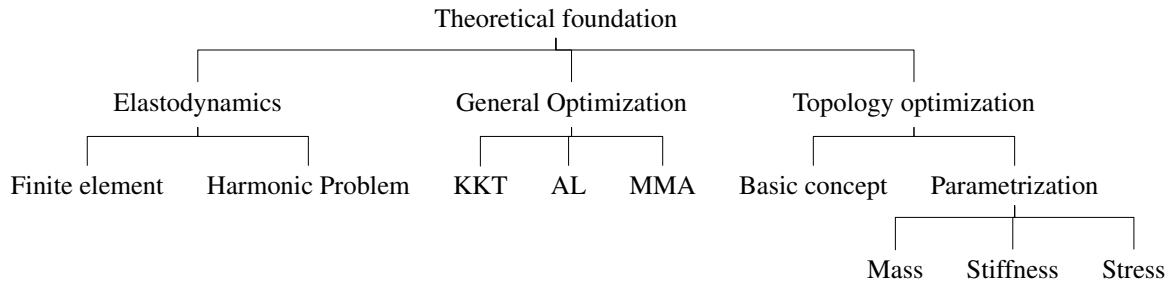
Source: Author production.

2.1 ELASTODYNAMICS

Applying the conservation of linear momentum over an infinitesimal portion of material of a continuous body subjected to external and internal loads

$$\nabla \cdot \boldsymbol{\sigma}(\mathbf{X},t) + \mathbf{b}(\mathbf{X},t) = \gamma(\mathbf{X})\ddot{\mathbf{u}}(\mathbf{X},t), \tag{1}$$

where $\boldsymbol{\sigma}(\mathbf{X},t)$ is the Cauchy stress tensor at the point $\mathbf{X}$, time t, $\mathbf{b}(\mathbf{X},t)$ is the vector of body forces at the point/time, $\gamma(\mathbf{X})$ is the specific mass of the material at the point and $\ddot{\mathbf{u}}(\mathbf{X},t)$ is the acceleration vector (MARSDEN; HUGHES, 1994).

Adding the contribution of viscous forces, a new term appears on the right side of Eq. (1)

$$\nabla \cdot \boldsymbol{\sigma}(\mathbf{X},t) + \mathbf{b}(\mathbf{X},t) = \gamma(\mathbf{X})\ddot{\mathbf{u}}(\mathbf{X},t) + \alpha\gamma(\mathbf{X})\dot{\mathbf{u}}(\mathbf{X},t), \tag{2}$$

where α is a material constant and $\dot{\mathbf{u}}(\mathbf{X},t)$ is the velocity vector at the point. The constant α represents a portion of the Rayleigh proportional damping.

The Cauchy stress tensor used in this work considers an additional viscous term,

$$\boldsymbol{\sigma}(\mathbf{X},t) = \mathbf{D}(\mathbf{X}) : \boldsymbol{\varepsilon}(\mathbf{X},t) + \beta\mathbf{D}(\mathbf{X}) : \dot{\boldsymbol{\varepsilon}}(\mathbf{X},t), \tag{3}$$

where $\mathbf{D}$ is the fourth order constitutive tensor of the linear elastic material, $\boldsymbol{\varepsilon}$ is the infinitesimal strain tensor at the point, $\dot{\boldsymbol{\varepsilon}}$ is its rate of change and β is a material coefficient (MONTERO, 2019).

The dependence with respect to position $\mathbf{X}$ and time t will be dropped, whenever possible, to simplify the notation.

We can relate infinitesimal strain to the displacement field using a linear (differential) operator $\mathbf{L}$ and the infinitesimal strain rate tensor

$$\boldsymbol{\varepsilon} = \mathbf{L}(\mathbf{u}) \tag{4}$$

and

$$\dot{\boldsymbol{\varepsilon}} = \mathbf{L}(\dot{\mathbf{u}}). \tag{5}$$

Replacing Eq. (3), (4), (5) into Eq. (2) results in

$$\boldsymbol{\nabla} \cdot (\mathbf{D} : (\mathbf{L}(\mathbf{u} + \beta \dot{\mathbf{u}}))) + \mathbf{b} = \gamma \ddot{\mathbf{u}} + \alpha \gamma \dot{\mathbf{u}}. \tag{6}$$

To derive the weak form of Eq. (6), we introduce an approximated vector field $\tilde{\mathbf{u}}$, leading to the formation of a residue $\mathbf{r}$

$$\mathbf{r} = \boldsymbol{\nabla} \cdot (\mathbf{D} : (\mathbf{L}(\tilde{\mathbf{u}} + \beta \dot{\tilde{\mathbf{u}}}))) + \mathbf{b} - \gamma \ddot{\tilde{\mathbf{u}}} - \alpha \gamma \dot{\tilde{\mathbf{u}}}. \tag{7}$$

Through the inner product of the residue with a test function vector field, denoted as $\mathbf{w}$, we establish weak convergence as

$$\int_{\Omega} \mathbf{w} \cdot \mathbf{r} d\Omega \rightharpoonup 0 \tag{8}$$

where Ω is the domain. Substituting Eq. (7) into Eq. (8) results in

$$\int_{\Omega} \mathbf{w} \cdot [\boldsymbol{\nabla} \cdot (\mathbf{D} : (\mathbf{L}(\tilde{\mathbf{u}} + \beta \dot{\tilde{\mathbf{u}}})))] d\Omega + \int_{\Omega} \mathbf{w} \cdot \mathbf{b} d\Omega - \int_{\Omega} \mathbf{w} \cdot \gamma \ddot{\tilde{\mathbf{u}}} d\Omega - \int_{\Omega} \mathbf{w} \cdot \alpha \gamma \dot{\tilde{\mathbf{u}}} d\Omega = 0. \tag{9}$$

Performing integration by parts on the first term of Eq. (9) yields

$$\int_{\Omega} \mathbf{w} \cdot [\boldsymbol{\nabla} \cdot (\mathbf{D} : (\mathbf{L}(\tilde{\tilde{u}} + \beta \dot{\tilde{\mathbf{u}}})))] d\Omega = \int_{\Gamma_t} \mathbf{w} \cdot \mathbf{t} d\Gamma_t - \int_{\Omega} \mathbf{L}(\mathbf{w}) : \mathbf{D} : (\mathbf{L}(\tilde{\mathbf{u}} + \beta \dot{\tilde{\mathbf{u}}})) d\Omega, \tag{10}$$

where Γ_t is the boundary of Ω with prescribed Neumann conditions, and $\mathbf{t}$ is the vector of the forces acting on Γ_t.

After simplifying the last term in Eq. (10) by expressing it in its vector equivalent quadratic form, Eq. (9) yields a comprehensive expression for the weak form problem. Letting $\tilde{\mathbf{u}}$ be written as $\mathbf{u}$ to simplify the notation, the weak form is provided as

$$\int_{\Omega} \mathbf{L}(\mathbf{w}) : \mathbf{D} : (\mathbf{L}(\tilde{\mathbf{u}} + \beta \dot{\tilde{\mathbf{u}}})) d\Omega + \int_{\Omega} \mathbf{w} \cdot \gamma \ddot{\mathbf{u}} d\Omega + \int_{\Omega} \mathbf{w} \cdot \alpha \gamma \dot{\mathbf{u}} d\Omega = \int_{\Omega} \mathbf{w} \cdot \mathbf{b} d\Omega$$
$$+ \int_{\Gamma_t} \mathbf{w} \cdot \mathbf{t} d\Gamma_t. \tag{11}$$

2.1.1 Finite Element Discretization

Consider a finite element e, a vector field $\mathbf{u}$ describes the displacements within the element via nodal discrete values $\mathbf{U}_e$ in the form

$$\mathbf{u} = \mathbf{N}\mathbf{U}_e, \tag{12}$$

where $\mathbf{N}$ is a matrix containing interpolation shape functions, local to element e and zero outside its domain Ω_e. To map the global vector $\mathbf{U}$ to its local values $\mathbf{U}_e$, an localization operator $\mathbf{H}_e$ is used such as

$$\mathbf{U}_e = \mathbf{H}_e\mathbf{U}. \tag{13}$$

In a similar manner, the vector field $\mathbf{w}$, velocities $\dot{\mathbf{u}}$ and accelerations $\ddot{\mathbf{u}}$ all follow the same interpolation and discretization, such that

$$\mathbf{w} = \mathbf{N}\mathbf{W}_e, \tag{14}$$

$$\dot{\mathbf{u}} = \mathbf{N}\dot{\mathbf{U}}_e, \tag{15}$$

and

$$\ddot{\mathbf{u}} = \mathbf{N}\ddot{\mathbf{U}}_e. \tag{16}$$

Using Voigt's notation and substituting the interpolation expressions in Eq. (11), results in

$$\sum_e \left(\int_{\Omega_e} \mathbf{L}_V\left(\mathbf{N}\mathbf{W}_e\right) \cdot \mathbf{D}\left(\mathbf{L}_V\left(\mathbf{N}\mathbf{U}_e\right)\right) \right) d\Omega_e + \int_{\Omega_e} \mathbf{N}\mathbf{W}_e \cdot \gamma\mathbf{N}d\Omega_e\ddot{\mathbf{U}}_e$$

$$+ \int_{\Omega_e} \mathbf{N}\mathbf{W}_e \cdot \alpha\gamma\mathbf{N}d\Omega_e\dot{\mathbf{U}}_e = \sum_e \left(\int_{\Omega_e} \mathbf{N}\mathbf{W}_e \cdot \mathbf{b}d\Omega_e + \int_{\Gamma_e} \mathbf{N}\mathbf{W}_e \cdot \mathbf{t}d\Gamma_e \right), \tag{17}$$

in which Ω_e and Γ_e are the volume and boundary of an element e. The constitutive tensor $\mathbf{D}$ is now represented as a matrix and the differential operator is now

$$\mathbf{L}_v = \begin{bmatrix} \frac{\partial}{\partial x} & 0 \\ 0 & \frac{\partial}{\partial y} \\ \frac{\partial}{\partial y} & \frac{\partial}{\partial x} \end{bmatrix} \tag{18}$$

for compatibility with Voigt's notation (in 2D). Now it is possible to write the inner product $\mathbf{w} \cdot \mathbf{u}$ as $\mathbf{w}^T \mathbf{u}$, such that Eq. (17) results in

$$
\sum_e \left(\mathbf{W}_e^T \int_{\Omega_e} \mathbf{L}_V \left(\mathbf{N}^T \right) \mathbf{D} \mathbf{L}_V \left(\mathbf{N} \right) d\Omega_e \mathbf{U}_e + \mathbf{W}_e^T \int_{\Omega_e} \mathbf{L}_V \left(\mathbf{N}^T \right) \mathbf{D} \mathbf{L}_V \left(\mathbf{N} \right) d\Omega_e \dot{\mathbf{U}}_e + \right.
$$
$$
\left. \mathbf{W}_e^T \int_{\Omega_e} \mathbf{N}^T \gamma \mathbf{N} d\Omega_e \ddot{\mathbf{U}}_e + \mathbf{W}_e^T \int_{\Omega_e} \mathbf{N}^T \alpha \gamma \mathbf{N} d\Omega_e \dot{\mathbf{U}}_e \right) =
$$
$$
\sum_e \left(\mathbf{W}_e^T \int_{\Omega_e} \mathbf{N}^T \mathbf{b} d\Omega_e + \mathbf{W}_e^T \int_{\Gamma_e} \mathbf{N}^T \mathbf{t} d\Gamma_e \right), \tag{19}
$$

where the local matrices of the element are given as

$$
\mathbf{K}_e = \int_{\Omega_e} \mathbf{L}_V \left(\mathbf{N} \right)^T \mathbf{D} \mathbf{L}_V \left(\mathbf{N} \right) d\Omega_e, \tag{20}
$$

$$
\mathbf{M}_e = \int_{\Omega_e} \mathbf{N}^T \gamma \mathbf{N} d\Omega_e, \tag{21}
$$

$$
\mathbf{C}_e = \alpha \mathbf{M}_e + \beta \mathbf{K}_e, \tag{22}
$$

and

$$
\mathbf{F}_e = \int_{\Gamma_e} \mathbf{N}^T \mathbf{t} d\Gamma_e - \int_{\Omega_e} \mathbf{N}^T \mathbf{b} d\Omega_e, \tag{23}
$$

where $\mathbf{K}_e$, $\mathbf{M}_e$ and $\mathbf{C}_e$ are respectively the stiffness, mass and damping matrices of the element, $\mathbf{F}_e$ is the force vector of the element and ^{T} is the transpose operator. At this point, it becomes clear that the proportionality constants α and β are actually the constants of the Rayleigh proportional damping.

Simplifying Eq. (19) with the local matrices of the element and using the localization operator results in

$$
\sum_e \left((\mathbf{H}_e \mathbf{W})^T \mathbf{M}_e \mathbf{H}_e \dot{\mathbf{U}} + (\mathbf{H}_e \mathbf{W})^T \mathbf{C}_e \mathbf{H}_e \dot{\mathbf{U}} + (\mathbf{H}_e \mathbf{W})^T \mathbf{K}_e \mathbf{H}_e \mathbf{U} \right) = \sum_e (\mathbf{H}_e \mathbf{W})^T \mathbf{F}_e \tag{24}
$$

or

$$
\mathbf{W}^T \mathbf{M} \ddot{\mathbf{U}} + \mathbf{W}^T \mathbf{K} \dot{\mathbf{U}} + \mathbf{W}^T \mathbf{K} \mathbf{U} = \mathbf{W}^T \mathbf{F}, \tag{25}
$$

where

$$\mathbf{M} = \sum_e \mathbf{H}_e^T \mathbf{M}_e \mathbf{H}_e, \tag{26}$$

$$\mathbf{K} = \sum_e \mathbf{H}_e^T \mathbf{K}_e \mathbf{H}_e, \tag{27}$$

and

$$\mathbf{C} = \sum_e \mathbf{H}_e^T \mathbf{C}_e \mathbf{H}_e, \tag{28}$$

are the global mass, stiffness and damping matrices, respectively, while

$$\mathbf{F} = \sum_e \mathbf{H}_e^T \mathbf{F}_e, \tag{29}$$

is the global force vector. Since $\mathbf{W}^T$ is present in all terms of Eq. (25), it is possible to satisfy the equilibrium equation with the following condition

$$\mathbf{W}^T \left(\mathbf{M}\ddot{\mathbf{U}} + \mathbf{C}\dot{\mathbf{U}} + \mathbf{K}\mathbf{U} - \mathbf{F} \right) = \mathbf{W}^T \mathbf{0}, \tag{30}$$

resulting in a system of linear equations

$$\mathbf{M}\ddot{\mathbf{U}}(t) + \mathbf{C}\dot{\mathbf{U}}(t) + \mathbf{K}\mathbf{U}(t) = \mathbf{F}(t), \tag{31}$$

with initial conditions

$$\dot{\mathbf{U}}(0) = \mathbf{V}^0 \tag{32}$$

e

$$\mathbf{U}(0) = \mathbf{U}^0. \tag{33}$$

Damping is an information that is generally estimated or requires a series of experimental tests to be defined. One usual way to represent damping is through proportional damping or Rayleigh damping, where the damping matrix is described as the linear combination of the mass and stiffness matrices,

$$\mathbf{C} = \alpha\mathbf{M} + \beta\mathbf{K}, \tag{34}$$

where both α and β were introduced in the continuous formulation Eq. (2) and (3). In this manner, it is possible to define constant values for these two coefficients. However, throughout the optimization process, the values of these parameters must be altered given that the stiffness and mass matrices are changed with each iteration. A sub model of this type of damping is obtained when $\alpha = 0$ such that

$$\mathbf{C} = \beta \mathbf{K}. \tag{35}$$

One method of defining β in a non-arbitrary manner was proposed by Silva, Neves and Lenzi (2019), where the stiffness constant is proportional to the excitation frequency

$$\beta = \frac{2}{\omega}, \tag{36}$$

where ω is the fixed angular excitation frequency of the problem. Continuing the development, Montero, Silva and Cardoso (2020) presented the damping value through its relation to a damping ratio ζ, the stiffness matrix $\mathbf{K}$, and the frequency ω,

$$\mathbf{C} = \frac{2\zeta}{\omega} \mathbf{K}. \tag{37}$$

In this way, it is possible to enforce an approximate value of ζ during the optimization.

2.1.2 Incompatible four-node quadrilateral isoparametric element

The finite element analysis is performed using the LFEM.jl library. Two dimensional plane stress elements with four nodes and incompatible "bubble" form functions are used in all examples. This selection is due to the fact that the simple four-node isoparametric element does not produce accurate results for bending (parasitic shear) (MARSDEN; HUGHES, 1994).

Since its establishment, the use of incompatible lower-order elements has reduced the need for reduced integration and the use of very high-order isoparametric elements (BATHE, 1996). The standard four-node quadrilateral isoparametric element has 8 degrees of freedom (DOFs); however, the incompatible elements incorporate an additional 4 artificial degrees of freedom. As a result the $\mathbf{K}$ matrix shown in Eq. (27) (12x12 size) can be condensed into an 8x8 matrix. This results in a better description of the behavior of "thin" regions under bending without a high computational cost (MARSDEN; HUGHES, 1994). Details about this finite element can be found at (PEREIRA, 2017).

2.1.3 Harmonic Problem

Consider a structure with linear response excited by a set of harmonic forces, such that the amplitude varies over time according to a fixed frequency, in the form

$$\mathbf{F}(t) = \mathbf{F}_0 e^{i\omega t}, \tag{38}$$

where $\mathbf{F}_0$ is the force vector containing the amplitudes, ω is the angular frequency of excitation and i is the complex component $\sqrt{-1}$. Based on the hypothesis of linearity of the system and considering that the response due to the initial conditions has already been dissipated, the response of the permanent displacements can be written as

$$\mathbf{U}(t) = \mathbf{U}_0 e^{i\omega t}, \tag{39}$$

where $\mathbf{U}_0$ is the complex vector of global displacements.

Velocity and acceleration are the first and second time derivatives of Eq.(39), respectively

$$\dot{\mathbf{U}}(t) = i\omega \mathbf{U}_0 e^{i\omega t}, \tag{40}$$

and

$$\ddot{\mathbf{U}}(t) = -\omega^2 \mathbf{U}_0 e^{i\omega t}. \tag{41}$$

Substituting these expressions into the global equilibrium equation, Eq. (31), results in

$$\left(-\omega^2 \mathbf{M} + i\omega \mathbf{C} + \mathbf{K}\right) \mathbf{U}_0 e^{i\omega t} = \mathbf{F}_0 e^{i\omega t}, \tag{42}$$

or

$$\mathbf{K_D} \mathbf{U}_0 = \mathbf{F}_0, \tag{43}$$

with

$$\mathbf{K_D} = -\omega^2 \mathbf{M} + i\omega \mathbf{C} + \mathbf{K}, \tag{44}$$

known as the dynamic stiffness matrix. Thus, the displacements $\mathbf{U}_0$ at a given angular frequency ω can be obtained by solving the linear system of equations in Eq. (42). This vector is complex, with the real part representing the amplitude of the displacement and the imaginary part its phase.

The viscous stress, Eq. (3), at a superconvergent point k of a finite element e can be particularized for the harmonic case as

$$\boldsymbol{\sigma}_{e,k} = \mathbf{D}_{e,k} \mathbf{B}_{e,k} \mathbf{H}_e (\mathbf{U}_0 + i\beta \omega \mathbf{U}_0), \tag{45}$$

where $\mathbf{D}_{e,k}$ is the constitutive matrix of the material at point k of the element e, $\mathbf{B}_{e,k}$ is the derivative matrix of the interpolation functions and $\mathbf{H}_e$ is a global-local localization matrix for the element e.

2.2 GENERAL OPTIMIZATION

In general, optimization consists in extremizing a functional $f(\mathbf{x})$, dependent on a set of design variables $\mathbf{x}$ while respecting a set of functional constraints $g_j(\mathbf{x})$ and $h_j(\mathbf{x})$

$$
\begin{cases}
\min & f(\mathbf{x}) \\
S.t. & \\
& g_j(\mathbf{x}) \leq \overline{g}_j \quad \text{for } j = 1, ..., m_g \\
& h_j(\mathbf{x}) = \overline{h}_j \quad \text{for } j = 1, ..., m_h \\
& \underline{x} \leq x_i \leq \overline{x} \quad \text{for } i = 1, ..., n
\end{cases}
\tag{46}
$$

where m_g is the number of inequality constraints g_j, m_h the number of equality constraints h_j, n is the number of design variables and $\overline{a}$ and $\underline{a}$ are the upper and lower bounds of a given variable or function a.

The function being minimized is called the objective function, the variables in the function are called the design variables and the domain of the design variables is called the search space.

2.2.1 Karush-Kuhn-Tucker Conditions

The essential conditions for finding a stationary point in an optimization problem are referred to as the Karush-Kuhn-Tucker (KKT) conditions. These conditions are derived by taking the partial derivatives of the Lagrangian function with respect to the design variables, Lagrange and Kuhn-Tucker multipliers. As stated by Arora (2007), the Lagrangian function for the optimization problem in Eq. (46) is

$$
\mathscr{L}(\mathbf{x}, \boldsymbol{\lambda}_L, \boldsymbol{\mu}) = f(\mathbf{x}) + \sum_{j=1}^{m_h} \lambda_{L_j} h_j(\mathbf{x}) + \sum_{j=1}^{m_g} \mu_j g_j(\mathbf{x})
\tag{47}
$$

where $\boldsymbol{\lambda}_L$ is the vector of Lagrange multipliers associated with each equality constraint h_j, and $\boldsymbol{\mu}$ is the vector containing the Kuhn-Tucker multipliers corresponding to each inequality constraint g_j.

The problem is considered solved when a stationary point is identified, meeting the Karush-Kuhn-Tucker (KKT) conditions. Assuming $f(\mathbf{x})$, $h_j(\mathbf{x})$, and $g_j(\mathbf{x})$ are twice differentiable at the local optimum point $(\mathbf{x}^*, \boldsymbol{\lambda}_L^*, \boldsymbol{\mu}^*)$, the KKT conditions are fulfilled when the following conditions are met:

- Stationarity

$$
\frac{df(\mathbf{x}^*)}{dx_m} + \sum_{j=1}^{n_h} \lambda_{L_j}^* \frac{dh_j(\mathbf{x}^*)}{dx_m} + \sum_{j=1}^{n_g} \mu_j^* \frac{dg_j(\mathbf{x}^*)}{dx_m} = 0, \quad \forall m = 1..n
\tag{48}
$$

- Primal feasibility

$$h_j(\mathbf{x}^*) = \overline{h}_j, \quad \forall j = 1..m_h \tag{49}$$

and

$$g_j(\mathbf{x}^*) = \overline{g}_j, \quad \forall j = 1..m_g \tag{50}$$

- Dual feasibility

$$\mu_j^* \geq 0, \quad \forall j = 1..m_g \tag{51}$$

- Complementary Slackness

$$\mu_j^* g_j(\mathbf{x}^*) = 0, \quad \forall j = 1..m_g \tag{52}$$

- Regular point: The gradients of the active constraints are linearly independent at $\mathbf{x}^*$.

If these conditions are satisfied, $\mathbf{x}^*$ is a local optimum.

2.2.2 Method of Moving Asymptotes (MMA) and its Globally Convergent version (GCMMA)

Equation (46) is usually comprised of non-linear and implicit functions of the design variables $\mathbf{x}$, making the direct use of the KKT conditions nearly impractical for general optimization problems. On the other hand, it is known that some specific optimization problems have closed or easier to compute solutions. Examples with known solutions are linear programming, where the functions are linear and quadratic programming, where the objective function is quadratic and the constraints are linear. Due to this fact, it is common to approximate the original problem given by Eq. (46) by a sequence of approximate problems with the desired mathematical structure. Theses approximations are known as sequential programming. In this regard, it is known that sequential convex approximations (like linear and quadratic) can be formulated as special cases of a more general form of approximations. One of the main used convex and separable approximations is the Method of Moving Asymptotes, or MMA, first presented in Svanberg (1987). The convex approximations are controlled by the movement of asymptotes $\mathbf{L}$ and $\mathbf{U}$, giving the method some flexibility when compared to fixed approximations (like the purely linear). Consider the general optimization problem of Eq. (46), but written with the same notation of Svanberg (1987)

$$P \begin{cases} \min & f_0(\mathbf{x}) \\ S.t. & \\ & f_i(\mathbf{x}) \leq \overline{f}_i \quad \text{for } i = 1, ..., m \\ & \underline{x} \leq x_j \leq \overline{x} \quad \text{for } j = 1, ..., n \end{cases} . \tag{53}$$

At each iteration, functions f_i are approximated by

$$\tilde{f}_i(\mathbf{x}) = r_i^k + \sum_{j=1}^{n} \left(\frac{p_{ij}^k}{U_j^k - x_j} + \frac{q_{ij}^k}{x_j - L_j^k} \right) \tag{54}$$

where

$$p_{ij}^k = \begin{cases} \left(U_{ij}^k - x_j^k\right)^2 \frac{\partial f_i}{\partial x_j} & if \quad \frac{\partial f_i}{\partial x_j} > 0 \\ 0 & if \quad \frac{\partial f_i}{\partial x_j} \leq 0 \end{cases}, \tag{55}$$

$$q_{ij}^k = \begin{cases} 0 & if \quad \frac{\partial f_i}{\partial x_j} \geq 0 \\ -\left(x_j^k - L_{ij}^k\right)^2 \frac{\partial f_i}{\partial x_j} & if \quad \frac{\partial f_i}{\partial x_j} < 0 \end{cases} \tag{56}$$

and

$$r_i^k = f_i(\mathbf{x}^k) - \sum_{j=1}^{n} \left(\frac{p_{ij}^k}{U_j^k - x_j^k} + \frac{q_{ij}^k}{x_j^k - L_j^k} \right). \tag{57}$$

With such convex and separable approximations, problem P given by Eq. (53) is approximated by

$$P_{MMA}^k \begin{cases} \min & \tilde{f}_0(\mathbf{x}) \\ S.t. & \\ & \tilde{f}_i(\mathbf{x}) \leq \overline{f}_i \quad \text{for } i = 1, ..., m \\ & \underline{x} \leq x_j \leq \bar{x} \quad \text{for } j = 1, ..., n \end{cases}. \tag{58}$$

Application of first order stationary conditions given by Eq. (48) leads to an explicit relation between primal variables $\mathbf{x}$ and dual variables $\boldsymbol{\mu}$ such that it is possible to solve an equivalent dual problem

$$\mathscr{D}^k \begin{cases} \max & l(\boldsymbol{\mu}) \\ S.t. & \\ & \mu_j \geq 0 \quad j = 1, ..., n \end{cases}, \tag{59}$$

which can be efficiently solved when the number of constraints (dual variables) is not large.

This iterative method can be summarized as

- Step 0: Choose an initial point $\mathbf{x}^0$ and set the iteration index k=0.

- Step 1: Given an iteration point $\mathbf{x}^k$, calculate $f_i(\mathbf{x}^k)$ and the gradients $\nabla_{\mathbf{x}} f_i(\mathbf{x}^k)$ for $i = 0, 1, ..., m$.

- Step 2: Generate a sub problem $\mathbf{P}_{MMA}^k$ by using, in P, the approximated functions $\tilde{f}_i$, based on the calculations from step 1.

- Step 3: Solve $\mathbf{P}^k_{MMA}$ by means of the dual problem, Eq. (59), and let the optimal solution of this sub problem be the next iteration point $\mathbf{x}^{k+1}$. Let $k = k+1$ and go to step 1.

This method is widely employed due to its flexibility in representing non-linear equations. The original version of MMA performed adequately in practice but lacked global convergence and occasionally failed on certain problems (SVANBERG, 2002). Consequently, a modified (conservative) version of MMA, known as GCMMA (Globally Convergent MMA), is proposed. This new version ensures global convergence and demonstrates superior speed compared to previous versions, outperforming them both theoretically and practically. The GCMMA method for solving problems comprises "outer" and "inner" iterations, where each generated iteration point is a feasible solution with a lower objective value than the preceding one. The index k is employed to represent the outer iteration number, whereas the index l is utilized to denote the inner iteration.

This method utilizes the first three steps identical to those presented previously; however, if $\tilde{f}_i^{(k,l)}(x^k) \geq f_0(x^k)$ is violated, inner iterations are executed. This means that a new sub problem is generated and solved, with new approximation functions $\tilde{f}_i^{(k,l+1)}(x^k)$, still aiming to satisfy $\tilde{f}_i^{(k,l+1)}(x^k) \geq f_0(x^k)$, but being more conservative than $\tilde{f}_i^{(k,l)}(x^k)$ for those indices for which the above inequality was violated. These inner iterations are repeated until $\tilde{f}_i^{(k,l)}(x^k) \geq f_0(x^k)$ for all $i - 0, 1, ...m$, which always occurs after a finite number of inner iterations (SVANBERG, 2002).

Nonetheless, both MMA and GCMMA tend to perform sub optimally when the number of constraints approaches the number of design variables. In these scenarios, the inclusion of alternative methods in the formulation can be considered, such as the Augmented Lagrangian (AL).

2.2.3 Augmented Lagrangian (LA)

Topology optimization problems with local stress constraints are known to have a very large number of non-linear constraints (MIYAJIMA; NOGUCHI; YAMADA, 2022). One common approach to address this kind of problem is to use the Augmented Lagrangian Approach (STANKIEWICZ; DEV; STEINMANN, 2022; VALENTINI; SILVA; CARDOSO, 2021). Although not unique, the concept of the AL can be described through

$$L^k(\mathbf{x}) = f(\mathbf{x}) + \sum_{j=1}^{m_{LA}} L^k_{g_j}(\mathbf{x}) \tag{60}$$

where $L^k(\mathbf{x})$ is a joint function of the original objective function $f(\mathbf{x})$ and of a functional comprising a set of constraints. This functional is a linear combination of functions

$$L^k_{g_j}(\mathbf{x}) = \frac{c^k_j}{2} \left\langle \frac{\mu^k_j}{c} + \frac{g_j(\mathbf{x})}{\bar{g}_j} - 1 \right\rangle^2 \tag{61}$$

where $\langle a \rangle = \max(a, 0)$, c_j^k are penalizations and μ_j^k is multipliers associated to each constraint j at outer iteration k and m_{LA} is the number of constraints used to build the functional.

The AL method employs two loops, internal and external. Within the internal loop, the problem is tackled while keeping μ_j^k and c_j^k constant until the optimal solution is reached. Upon reaching this point, updates to the penalty parameters and multipliers are executed following the approach outlined in Birgin and Martínez (2014). In their study, the authors highlight the lack of consensus within the Augmented Lagrangian framework regarding whether updates at each external iteration should target the multipliers, the penalty parameters, or both. Consequently, this work adopts the recommendation proposed in Birgin and Martínez (2014) to update both simultaneously.

The penalty update depends on a test between the constraint values and penalties from the previous iteration with the current iteration. Defining

$$V_j^k = \max\left(g_j^k(\mathbf{x}), -\frac{\mu_j^k}{c_j^k} \right), \quad j = 1...m_{LA}, \tag{62}$$

if the value of V_j^k is greater than the value of the same variable in the previous iteration ($V_j^k > V_j^{k-1}$), the penalty is updated as

$$c_j^{k+1} = r_c c_j^k, \quad j = 1...m_{LA}, \tag{63}$$

where r_c is the penalty increase rate. Otherwise, penalization $c_j^{k+1} = c_j^k$.

The update of the Lagrange multipliers is performed at the end of each iteration,

$$\mu_j^{k+1} = \left\langle \mu_j^k + c_j^k g_j^k(\mathbf{x}) \right\rangle, \quad j = 1...m_{LA}. \tag{64}$$

2.3   TOPOLOGY OPTIMIZATION

There are three main types of structural optimization: shape, size, and topology. Each employs its own method to maximize or minimize the objective function. However, topology optimization is the one that offers the greatest flexibility in generating non-conventional solutions.

Topology optimization (TO) is used to obtain the best material distribution in a fixed design domain Ω minimizing or maximizing an objective function while respecting a set of constraints and boundary conditions, Figure 4.

Its designation as "structural" stems from the fact that the optimized structure is achieved under the condition that the problem satisfies the governing equations describing the physical phenomena and the objective functions and/or constraints have some physical meaning (MIYAJIMA; NOGUCHI; YAMADA, 2022).

Figure 4 – Design domain.
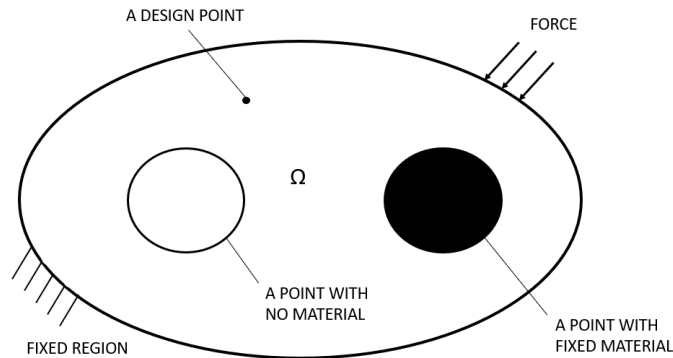
Source: Author production.

2.3.1 Material parameterization

One of the key aspects to any TO formulation is the material parameterization, *i.e.*, how the material distribution is considered as design variables in the optimization problem. The literature in topology optimization is rich in many different material parameterizations, such homogenization (BENDSØE; KIKUCHI, 1988), level set (JUNIOR; FANCELLO; SILVA, 2020) and SIMP (BENDSØE; SIGMUND, 1999).

This work uses the Solid Isotropic Material with Penalization (SIMP) parameterization, where the material distribution is represented by a simplified rule of mixtures between an isotropic base material and void. This rule of mixture is parameterized by using a relative material density (or just relative density) ρ at each point of Ω. When using finite elements to discretize Ω, one can assume that element e has effective constitutive tensor for the elastic properties $\mathbf{D}_e$ given by

$$\mathbf{D}_e = \rho_e^p \mathbf{D}_e^0, \tag{65}$$

where ρ_e is the relative density at element e, p is a penalty exponent and $\mathbf{D}_e^0$ the constitutive matrix for the elastic properties of the base material.

The SIMP parameterization is largely employed in static problems, since the only material properties of interest are the Young's modulus and the Poisson's ratio (used to build $\mathbf{D}^0$). In harmonic problems, other very important material property is the mass. Nonetheless, it is known that the simple extension of Eq. (65) to the mass parameterization is not the best approach.

During topology optimization of modal/harmonic/transient problems, some elements may present low relative densities even for large exponent p in the SIMP parameterization. These regions may suffer artificial vibration modes and frequencies (spurious or void modes), and it is known that those vibration modes appear due to the high mass/stiffness ratio of the elements when the naive mass parameterization is used (NEVES; RODRIGUES; GUEDES, 1995).

Olhoff and Du (2009) proposed an alternative parameterization to alleviate this problem. The modified mass parameterization is given by
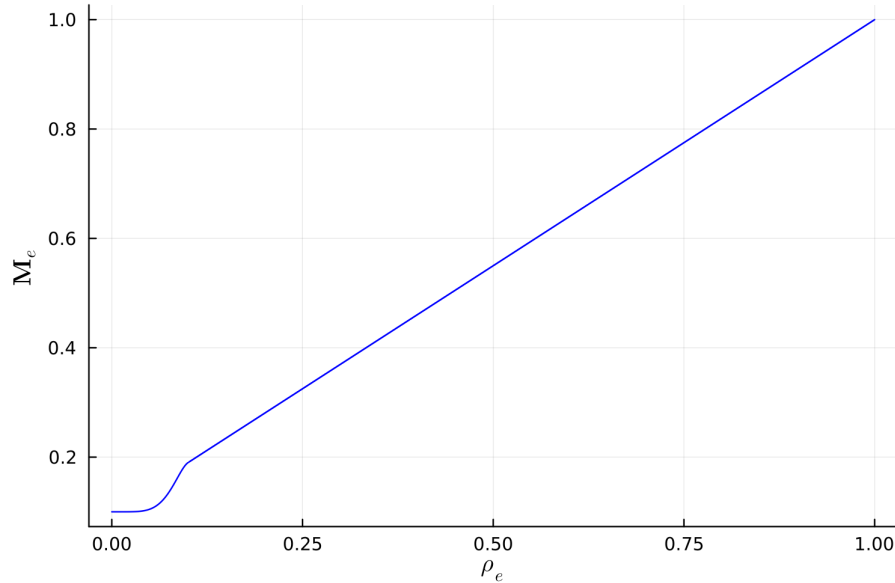
Figure 5 – Mass parameterization function proposed by Olhoff and Du (2009).

$$
\mathbf{M}_e = \begin{cases} (\rho_l + (1 - \rho_l)\rho_e)\mathbf{M}_e^0, & \text{if } \rho_l < \rho_e \leq 1.0 \\ (\rho_l + (C_1\rho_e^6 + C_2\rho_e^7))\mathbf{M}_e^0, & \text{if } \rho_e \leq \rho_l \end{cases},
\tag{66}
$$

where $\mathbf{M}_e$ is the effective mass matrix of element e, $\mathbf{M}_e^0$ is the mass matrix of the base material, ρ_l is a cutoff relative density used to change the behavior of the mass/stiffness ratio. Constants C_1 and C_2 are given by

$$
C_1 = -\frac{6\rho_l - 6}{\rho_l^5}
\tag{67}
$$

and

$$
C_2 = \frac{5\rho_l - 5}{\rho_l^6},
\tag{68}
$$

and a cutoff value of $\rho_l = 0.1$ is used in this work (SILVA, 2017). The behavior of this parametrization is shown in Fig. 5.

2.3.2 Filter and projection

Mesh dependence is both a physical and mathematical problem, as it is known that the optimal solution for the distribution of an isotropic material consists of creating infinitesimal reinforcements (structures of the rank type). Therefore, the more refined the finite element discretization, for example, the greater the number of design variables and the smaller the size of the reinforcements in the optimized topology. In these cases, spatial filters are used to approximately impose a scale control to prevent the optimization from creating reinforcements

smaller than the filtering radius. In general, we can indicate this operation as a mapping between a set of design variables $\mathbf{x}$ (also called mathematical variables) to a set of filtered variables $\tilde{\boldsymbol{\rho}}$

$$\mathbf{x} \overset{Filter}{\rightarrow} \tilde{\boldsymbol{\rho}}. \tag{69}$$

The spatial filter used in this work is based on the weighted average between the mathematical variables $\mathbf{x}$ of neighboring elements of e as

$$\tilde{\rho}_e = \frac{\sum\limits_{i \in \Omega_{Ne}} w_{e,i} x_i}{\sum\limits_{i \in \Omega_{Ne}} w_{e,i}}, \tag{70}$$

where $w_{e,i}$ are the weights and Ω_{Ne} is the set of neighbors of the element e. This neighborhood is determined by a radius R, such that

$$\Omega_{Ne} = \{i \mid d_{i,e} \leq R\} \tag{71}$$

where $d_{i,e}$ is the distance between the centroids of elements e and i and

$$w_{e,i} = 1 - \frac{d_{i,e}}{R}. \tag{72}$$

However, the fact that we use filters and also a continuous material parameterization means that the optimal solution contains many filtered variables with intermediate values. The most used solution in the literature consists of performing some smooth approximation for the Heaviside operator, such that the variables assume values close to 0 or 1. This operation is generally called projection and is performed after the filtering step, such that

$$\mathbf{x} \overset{Filter}{\rightarrow} \tilde{\boldsymbol{\rho}} \overset{Projection}{\rightarrow} \boldsymbol{\rho} \tag{73}$$

where $\boldsymbol{\rho}$ are the relative densities that will be used to describe the distribution of the material (evaluate equilibrium, objective and constraints).

The projection used in this work is the smooth approximation of the translated Heaviside function

$$\rho_e = H(\tilde{\rho}_e - \eta) \approx \frac{\tanh \beta_p \eta + \tanh \beta_p(\tilde{\rho}_e - \eta)}{\tanh \beta_p \eta + \tanh \beta_p(1 - \eta)} \tag{74}$$

where $\eta = 0.5$ is the value where the transition between 0 and 1 must occur and β_p is an adjustment factor for the Heaviside approximation (the higher the value of β_p, the closer to the real Heaviside) (WANG; LAZAROV; SIGMUND, 2011).

2.3.3 Stress Constraints

Stress analysis is essential for any structural design, as it avoids designing a structure that cannot withstand the applied loads. However, its application presents two difficulties: the fact that stress is a local measure (dimension problem) and may generate irregular feasible spaces (singularity problem). Furthermore, the imposition of stress constraints generally leads to the presence of multiple local minima within the feasible set. This introduces a significant dependency of the solution on the initial starting point provided to the minimization algorithm (BRUGGI, 2008).

The high number of constraints (dimension problem) makes it difficult to use local constraints in traditional optimizers, as it involves high computational time and increased instability in the solution (PEREIRA; CARDOSO, 2018). This problem can be addressed through the use of aggregation strategies (such as regional norms), targeting a small number of constraint (BRUGGI, 2008; LE et al., 2010). As shown by Pereira and Cardoso (2018), the local constraint, using the Augmented Lagrangian Approach, yields superior results in hinge elimination and thus will be the strategy employed in this study.

The stress-constrained TO is highly nonlinear with respect to the design variables. Also, it is known that degenerate (singular) solutions with dimension smaller than the original problem may be the true optimal point (KIRSCH, 1989). To reverse this situation it is necessary to use some sort of relaxation (GUO; CHENG, 1997; BRUGGI, 2008). Again, a SIMP like parameterization for the effective stress can be written as

$$\boldsymbol{\sigma}_e = \rho_e^p \boldsymbol{\sigma}_e^0, \tag{75}$$

where $\boldsymbol{\sigma}_e^0$ is the nominal stress at element e. This parameterization is shown to lead to the singularity problem by Duysinx and Bendsøe (1998), Guo and Cheng (1997), Bruggi (2008) such that Bruggi (2008) proposed an alternative (relaxed) form as

$$\boldsymbol{\sigma}_e = \rho_e^{p-q} \boldsymbol{\sigma}_e^0, \tag{76}$$

where $q < p$ is an additional exponent. This is the approach used in this work.

2.3.4 Localized (lumpled) compliance

The design of compliant mechanisms is performed by the suitable placement of regions with proper compliances. Thus, some regions will be stiffer (as, for example, next to the output ports and forces) and some regions will be more flexible. Nonetheless, regions with lumped compliance are not desired, since they usually have large stresses.

Figure 6 presents the three ways in which localized compliance can be presented in a CM.

Figure 6(a) shows an artificial and pathological solution usually found in many references. This single node connection between two adjacent elements is known as hinge, since elasticity does not have rotational degrees of freedom and, therefore, this type of connection has no rotational stiffness. Those hinges are undesired since an ideal compliant mechanism should be a continuous part (PEREIRA; CARDOSO, 2018).

The second form, *de facto* hinges, has a slightly less lumped compliance, in which the edges of the elements are in contact but a region of defined compliance can still be determined, as shown in Figure 6(b). Regions with distributed compliance are shown in Figure 6(c).

Figure 6 – Different forms of lumped compliance: (a) one-node connected hinges; (b) *de facto* hinges; (c) distributed compliance.
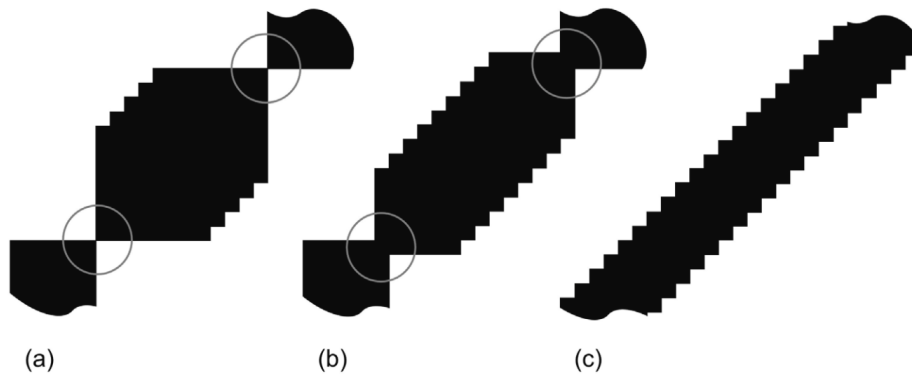
Source: Seltmann and Hasse (2023)

The literature presents different approaches to avoid the appearance of hinges. One of the proposed alternatives are geometric approaches such as the use of filters (SIGMUND, 2007) or constraints on minimum dimensions for compliance regions (ZHANG; ZHONG; GUO, 2014) and (LIANG; SUN; CHENG, 2020). Another commonly used method addresses hinges connected to a single node by applying local or global stress constraints. These constraints can be implemented directly or incorporated into the objective function (PEREIRA; CARDOSO, 2018). Stankiewicz, Dev and Steinmann (2022) presents a solution to this issue, combining the AL approach with MMA to introduce local stress constraints, which proves to be the most efficient option among the methods analyzed.

All previously described approaches may, in some cases, prevent one-node connected hinges. However, none of them are suitable for designing mechanisms with distributed compliance. According to Seltmann and Hasse (2023), there is limited literature addressing distributed compliance. Existing approaches in this area typically involve weighting various requirements within the objective function, resulting in arbitrary outcomes. A different approach is proposed by Cardoso and Fonseca (2004), based on energy balance between inputs, outputs and elastic energy stored in the compliant parts.

Recently, Seltmann and Hasse (2023) proposed the use of an adaptive volume constraint. The idea is quite simple, where the upper bound of the volume constraint is changed (reduced) if the stress constraints are not satisfied. This reduction in the upper limit of the volume fraction

is performed alongside the moving limits used in the sequential linear programming approach used by the authors. Although the proposal lacks mathematical development, the results in this reference motivated the use of similar approach in the present work. The implementation of the adaptive volume constraint is developed in Section 3.

3 PROBLEM FORMULATION

This section aims to present the formulation proposed and developed in this work. Sigmund (2009), Zhu et al. (2020), Senne, Gomes and Santos (2022) present some common benchmark problems for CM design using topology optimization. Figure 7 shows two common benchmarks: the inverter and the gripper. The inverter mechanism is used as a case study in this work, since the phase (direction) between the input and the output presents a challenge for harmonic problems. However, once the formulation is validated, it can be applied to any compliant mechanism.

Figure 7 – Design domain of topology optimization mechanisms: (a) inverter and (b) gripper.

(a)   (b)
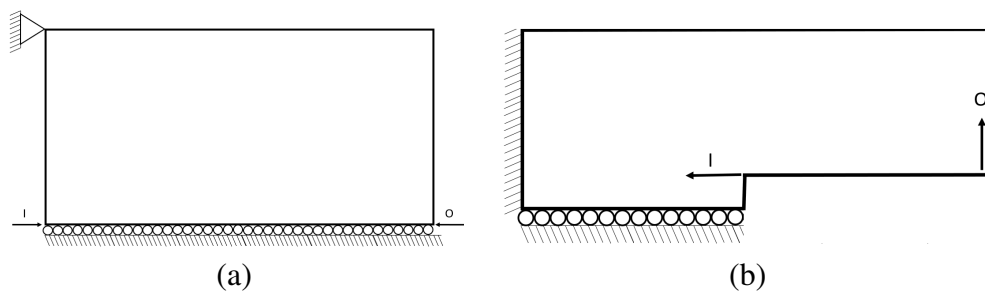
Source: Based on Zhu et al. (2020)

Figure 8 illustrates the classical boundary conditions for an inverter mechanism. In this configuration, there is an assigned input region for external forces and an output region where a specific behavior is expected. Typically, a point load is applied at the input, and a spring, representing the stiffness of the external environment, is present at the output. The domain is modeled through symmetry in the horizontal plane.

According to Deepak, Dinesh and Ananthasuresh (2008), the design of compliant mechanisms is intrinsically linked to applications where an output is known. In the absence of an output spring or load, the topology optimization algorithm lacks motivation to establish a material connection to the output point. As it will be discussed in this chapter, the material connection is a major issue in modal, harmonic and transient problems, due to the frequency response being highly dependent on stiffness and mass distribution.

Although the representation depicted in Figure 8 is one of the most simplified for a compliant mechanism, the harmonic formulation allows for various additions to the boundary conditions, such as springs, dampers, masses, forces and imposed displacements or velocities at different nodes in the domain.

There are many optimization problems developed for the design of CMs in static regime. Based on the formulation presented by Pereira and Cardoso (2018)

Figure 8 – Inverter mechanism.
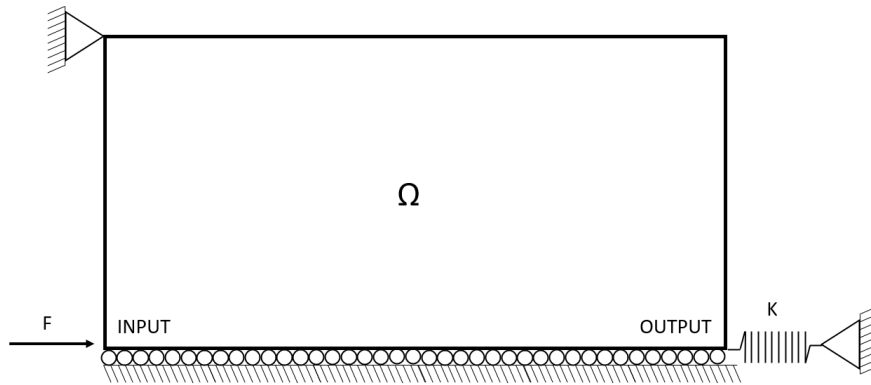
Source: Author production.

$$\begin{cases} \min \quad -u_{out}(\mathbf{x}), \\ S.t. \\ \quad \mathbf{K}(\mathbf{x})\mathbf{U}(\mathbf{x}) = \mathbf{F}(\mathbf{x}) \\ \\ \quad u_{in}(\mathbf{x}) \leq \bar{u}_{in} \\ \quad V(\mathbf{x}) \leq \bar{v} \\ \quad \sigma_e(\mathbf{x}) \leq \bar{\sigma} \qquad \text{for } e = 1,...,n \\ \quad \underline{\mathbf{x}} \leq \mathbf{x} \leq \bar{\mathbf{x}} \end{cases} \tag{77}$$

where u_{out} is the output displacement, u_{in} the input displacement, $\bar{u}_{in}$ the upper bound in the input displacement, V is the volume, $\bar{v}$ the upper bound in volume constraint, σ_e is the equivalent von-Mises stress for element e, $\bar{\sigma}$ is the yield limit for the base material, n is the number of finite elements, $\mathbf{x}$ is a design variables with it is lower limits $\underline{\mathbf{x}}$ and upper limits $\bar{\mathbf{x}}$. This formulation uses a simple objective function, which aims to maximize the displacement magnitude of an inverter mechanism, in other words, to minimize the negative of this value.

As previously mentioned, Eq. (77) intends to represent a static problem. However, when our objective is to propose a formulation for the harmonic regime, a series of modifications need to be made, as presented in the theoretical foundation section. Next, the steps necessary to convert this formulation to the harmonic regime will be discussed.

3.1 EQUILIBRIUM EQUATIONS

The first modification is the change from the static equilibrium equation to the complex valued harmonic equilibrium equation, Eq. (43) and Eq. (44)

$$\mathbf{K_D}\mathbf{U}_0 = \mathbf{F}_0, \tag{78}$$

with

$$\mathbf{K_D} = -\omega^2\mathbf{M} + i\omega\mathbf{C} + \mathbf{K}. \qquad (79)$$

This change makes the problem dependent on the frequency, the damping and the mass, along with the stiffness, such that there are more material properties involved in the optimization procedure. Thus, the change from static to harmonic equilibrium is not direct, since characteristics like inertia, damping and driven frequency are now relevant to the optimization.

3.2   CONSTRAINTS

After determining the objective function, this section presents the equations used to calculate volume, displacement and local stress constraints.

3.2.1   Volume constraint

The volume constraint does not have variables that are modified by the change from static to harmonic regime. This constraint is given by

$$g_v(\mathbf{x}) = \frac{V(\mathbf{x})}{\bar{v}} - 1. \qquad (80)$$

where $V = \sum_j^n \rho_j v_j^0$ is the sum of the effective element volumes.

3.2.2   Input displacement constraint

When considering harmonic problems, the input displacement u_{in} is now a complex valued function of the design variables. Thus, the harmonic constraint can be written as

$$g_{in}(\mathbf{x}) = \frac{|u_{in}|}{\bar{u}_{in}} - 1 \qquad (81)$$

where $|u_{in}|$ is the absolute value of the complex input displacement and $\bar{u}_{in}$ its upper value. This simple modification makes the harmonic constraint much like the static one.

3.2.3   Local stress constraints

For the stress constraint, the expression remains the same as the static case, being the ratio between the equivalent stress of the element e at the superconvergent point k by its limit value $\bar{\sigma}$

$$g_\sigma(\mathbf{x}) = \frac{\sigma_{e,k}}{\bar{\sigma}} - 1. \qquad (82)$$

However, the stress calculation is updated for the harmonic regime, as shown in Eq. (45)

$$\boldsymbol{\sigma}_{e,k} = \mathbf{D}_{e,k}\mathbf{B}_{e,k}\mathbf{H}_e(\mathbf{U}_0 + i\beta\omega\mathbf{U}_0), \tag{83}$$

such that it depends on the solution of the harmonic equilibrium problem, along with the direct dependence of the damping factor β and the angular frequency. Also, the stress in harmonic regime is a complex-valued function.

Assuming ductile and isotropic material, one can obtain the local, real valued, von-Mises stress of Eq. (77) by using (SURHONE; TIMPLEDON; MARSEKEN, 2010)

$$\sigma_{e,k} = \sqrt{\boldsymbol{\sigma}_{e,k}^H \mathbf{V} \boldsymbol{\sigma}_{e,k}} \tag{84}$$

where $\boldsymbol{\sigma}_{e,k}$ is the stress, $\boldsymbol{\sigma}_{e,k}^H$ denotes its complex conjugate and $\mathbf{V}$ is the Voigt matrix. Other issues like the singularity and the large number of local stress constraints are addressed by using the QP-relaxation and the Augmented Lagrangian approach.

3.3 OBJECTIVE FUNCTION

In a harmonic system, the output displacement value is represented by a complex number. The complex nature of the displacements encodes both amplitude (real part) and phase (imaginary part),

$$u_{out} = \Re(u_{out}) + i\Im(u_{out}) = u_{out_R} + iu_{out_I}, \tag{85}$$

such that one cannot simply state that the minimization of the negative output displacement results in an inverter mechanism. For example, for excitation frequencies below the first resonance frequency the input displacement is in phase with the input force and one can assume that making the output displacement negative is a good objective function for an inverter mechanism (assuming a positive input force). Nonetheless, in harmonic problems one must cope with the complex nature of displacement (real and imaginary parts) as well as phase inversions. Thus, one cannot simply extend the formulation presented in Eq. (77) by using only the absolute value of the output displacement, since information about relative phase (between input and output) is necessary to ensure the inverter behavior.

An alternative investigated in the early stages of this work was to maintain the objective function presented in Eq. (77) while adding a phase constraint between the input and output displacements. This formulation was shown to be unsatisfactory due to discontinuity problems. However, as it was one of the first formulations tested and served as the basis for the formulation developed in the following comments, it is presented in Appendix A for reference.

After discarding the feasibility of phase control through a constraint, the research turned to the development of a formulation that encompasses an objective function capable of incorporation both information: the magnitude of the output displacement and the relative phase between the displacements of interest.

3.3.1 Geometric advantage for harmonic problems

The first approach adopted for the objective function was the ratio between the input and the output displacement. This operation brings the relative phase information to the formulation. Such operation can also be interpreted as an extension of the geometric advantage concept to the harmonic case. The optimization problem is

$$
\begin{cases}
\min & GA_H \\
S.t. & \\
& \mathbf{K_D(x)U(x) = F(x)} \\
& g_{in}(\mathbf{x}) \leq 0 \\
& g_v(\mathbf{x}) \leq 0 \\
& g_{\sigma_{e,k}}(\mathbf{x}) \leq 0 \\
& \underline{\mathbf{x}} \leq \mathbf{x} \leq \bar{\mathbf{x}}
\end{cases}
\tag{86}
$$

where GA_H is the objective function.

The concept of geometrical advantage is the ratio of the output by the input displacements. The original definition is straightforward for static problems, since both quantities are real numbers. A natural extension of this measure for harmonic (complex valued) problems, is

$$
GA_H = \Re\left(\frac{u_{out}}{u_{in}}\right) = \Re\left(\frac{u_{out_R} + iu_{out_I}}{u_{in_R} + iu_{in_I}}\right) = \frac{u_{in_R}u_{out_R} + u_{in_I}u_{out_I}}{|u_{in}|^2}.
\tag{87}
$$

It is important to stress that the direct ratio of the real part of both the input and the output displacements caries no information about the phase. For this reason, we first evaluate the ratio and then extract the real part.

This objective function was tested for different frequencies. Figure 9 depicts the input and output displacements for the 500 Hz configuration. It can be seen that the largest absolute values in both input and output displacements are at the resonance frequency, 388 Hz. Nonetheless, as depicted in Fig. 10, the proposed objective function (Ga_H) has, indeed, a minimum value at 500 Hz (the desired, or the excitation frequency).

Analyzing the objective function presented earlier and shown in Figure 10, it quantifies the geometric advantage through the ratio between output and input displacement. Since the optimizer was constrained by the input displacement, the only way to increase the objective function would be to increase the (negative of the) absolute value of the output displacement, thus ensuring the optimized geometric advantage. This is the intended behavior.

However, the optimizer adopted a different path: instead of increasing the output displacement, it reduced the input displacement (it is possible observe from the graph presented in Figure 9 that the input displacement at the frequency of 500 Hz is much lower than in other regions). The culprit is the term $\frac{1}{|u_{in}|^2}$.

Figure 9 – Dynamical behavior for the optimized topology obtained using Eq. (87) and excitation at 500 Hz.
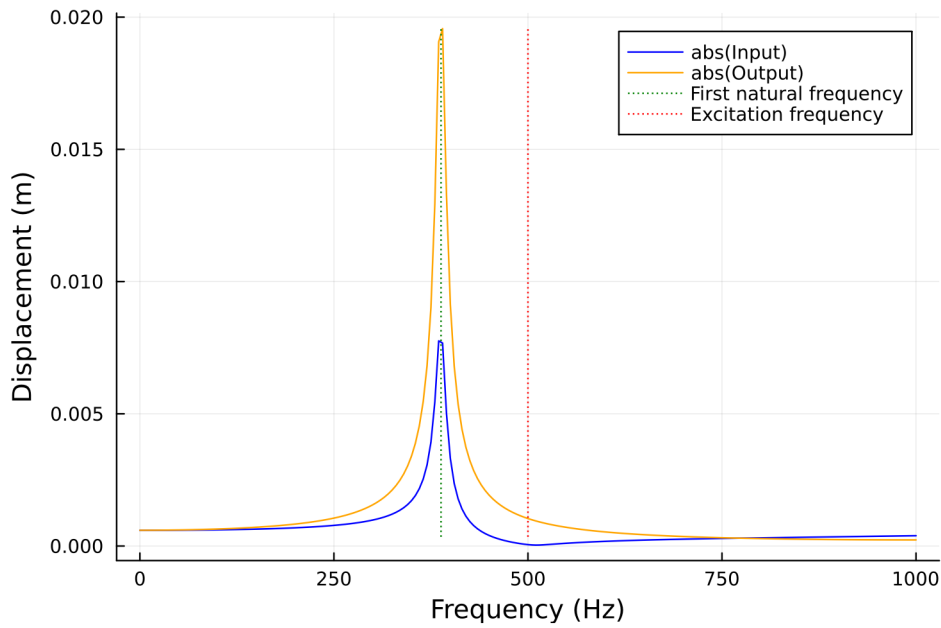
Source: Author production.

Figure 10 – Behavior of the objective function given by Eq. (87) and excitation at 500 Hz.
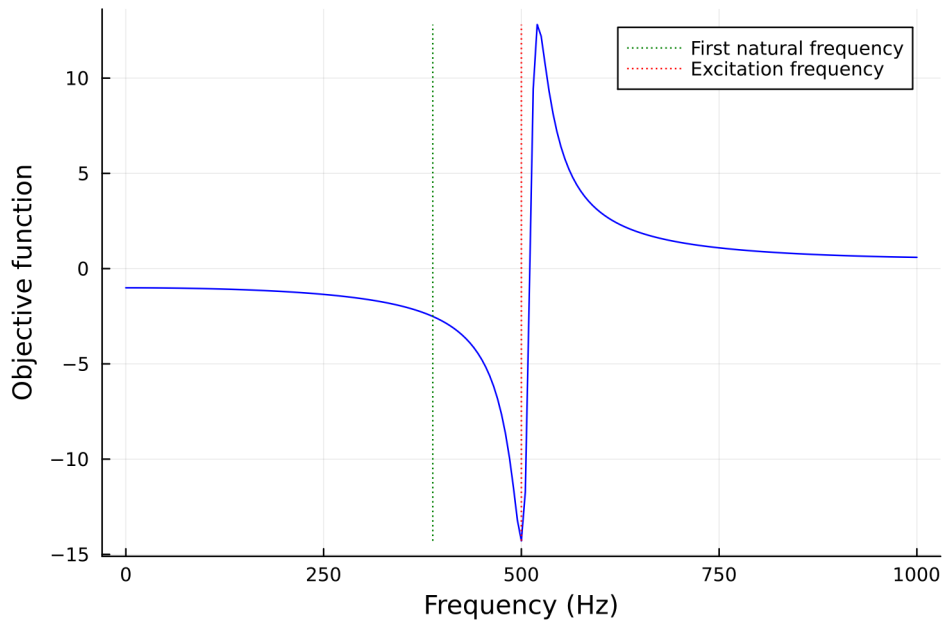
Source: Author production.

If the objective function were altered, removing the denominator from the previous expression, we would have the desired response. Nonetheless, such modification changes the original definition and, thus, its physical meaning must be investigated.

3.3.2 Time average product

The definition of the current proposal came from the observation of the results of the previous formulation. The new objective function is given by

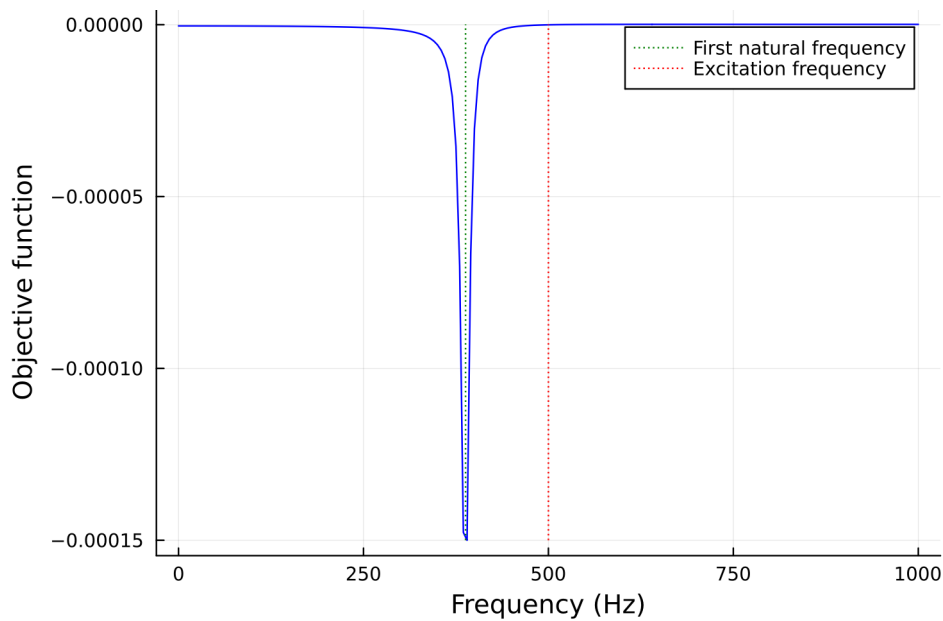$$f(\mathbf{x}) = u_{in_R}u_{out_R} + u_{in_I}u_{out_I},$$ (88)

the numerator of Eq. (87). Figure 11 shows the behavior of this objective function when used with the same data of Figure 10. Now, the peak is exactly at the resonance, as intended.

Figure 11 – Objective value for the new objective function defined in Eq. (88).

Source: Author production.

To understand the physical meaning of this expression, we define two harmonic quantities with period T and real parts

$$X_R = |X_0|cos(\omega t + \phi_X) = \Re(X_0 \exp^{i(\omega t + \phi_X)})$$ (89)

and

$$Y_R = |Y_0|cos(\omega t + \phi_Y) = \Re(Y_0 \exp^{i(\omega t + \phi_Y)})$$ (90)

where $\bar{X}$ and $\bar{Y}$ are complex amplitudes of the quantities, ϕ the phase and ω the angular frequency. In nature, the real part of a measure represented in the harmonic form is what really "exists". The time average in the interval $t \in [t_0, t_0 + T]$, the effective value of the product (XY), is given by

$$(X_R Y_R)_{av} = \frac{1}{T} \int_{t_0}^{t_0+T} X_R Y_R dt,$$ (91)

or

$$(X_R Y_R)_{av} = \frac{1}{T} \int_{t_0}^{t_0+T} |X_0| cos(\omega t + \phi_X) |Y_0| cos(\omega t + \phi_Y) dt. \tag{92}$$

The following trigonometric rule is useful in this case

$$cos(\alpha)cos(\beta) = \frac{1}{2}cos(\alpha - \beta) + \frac{1}{2}cos(\alpha + \beta), \tag{93}$$

such that

$$(X_R Y_R)_{av} = \frac{1}{T} \int_{t_0}^{t_0+T} |X_0||Y_0| \left(\frac{1}{2}cos(2\omega t + \phi_x + \phi_y) + \frac{1}{2}cos(\phi_x - \phi_y) \right) dt. \tag{94}$$

The first cosine in Eq. (94) vanishes after integration, such that

$$(X_R Y_R)_{av} = |X_0||Y_0|\frac{1}{2}cos(\phi_x - \phi_y) = \frac{1}{2}\Re\left(X_0 Y_0 e^{i(\phi_x - \phi_y)} \right) \tag{95}$$

rewriting,

$$(X_R Y_R)_{av} = \frac{1}{2}\Re\left(X_0 e^{i(\phi_x)} Y_0 e^{i(-\phi_y)} \right) \tag{96}$$

such that,

$$(X_R Y_R)_{av} = \frac{1}{2}\Re(XY^*), \tag{97}$$

in which the symbol $*$ represents complex conjugate of a number. Equation (97) represents the effective value of the product of two real-time-varying measures X and Y.

In this context, the proposed objective function

$$f(\mathbf{x}) = u_{in_R} u_{out_R} + u_{in_I} u_{out_I} \tag{98}$$

can be related to

$$(u_{in} u_{out})_{av} = \frac{1}{2}\Re\{u_{in} u_{out}^*\} = \frac{1}{2}\Re\{(u_{in_R} + i u_{in_I})(u_{out_R} - i u_{out_I})\}, \tag{99}$$

$$(u_{in} u_{out})_{av} = \frac{1}{2}\Re\{u_{in_R} u_{out_R} - i u_{in_R} u_{out_I} + i u_{in_I} u_{out_R} + u_{in_I} u_{out_I}\}. \tag{100}$$

or

$$(u_{in} u_{out})_{av} = \frac{1}{2}\left(u_{in_R} u_{out_R} + u_{in_I} u_{out_I} \right) = \frac{1}{2}f(\mathbf{x}). \tag{101}$$

Therefore, the objective function used for the topologies presented in this work is given by twice the time average of the product for u_{in} and u_{out}

$$f(\mathbf{x}) = u_{in_R} u_{out_R} + u_{in_I} u_{out_I} = 2(u_{in} u_{out})_{av}. \tag{102}$$

3.4 COMPUTER IMPLEMENTATION

After establishing the objective function and constraints, this section will present the steps that will constitute the optimization algorithm. The flowchart of the optimization procedure used in this work is shown in Figure 12. The first step consists of defining the initial parameters of: design domain, boundary conditions, material properties, excitation frequency, AL parameters, GCMMA parameters, damping, constraint limits and initial design variables. The initial parameters used will be presented in the results section.

With all the initial information obtained, the optimization process begins. There is one main loop (external), represented by k. The first iteration of the loop starts with $\boldsymbol{\mu} = \mathbf{0}$, given $\mathbf{x}^0$ (initial point) and $\mathbf{c}$ (initial penalties) as well as a "large" damping ratio $\zeta = \zeta_{ini}$. The LA procedure depicted in the theory section is used, with both $\mathbf{c}^k$ and $\boldsymbol{\mu}^k$ being updated at the end of each external loop.

The damping continuation is performed during the first $n_{damping}$ external iterations, until $\zeta = \zeta_{tar}$. The decrease in ζ is assumed as linear. The adaptive volume constraint starts to be employed for $k > n_{damping}$. At each iteration, the upper limit is decreased as

$$\bar{v}^{k+1} = \max\left(\bar{v}_{min}, \bar{v}^k - r_v\right) \tag{103}$$

in which r_v is the rate of decrease in fraction and $\bar{v}_{min}$ is the lower bound on $\bar{v}$, if at least one stress constraint is violated.

The outer loop may exits in two ways: either the number of iterations exceeds the threshold value n_{max} or it satisfies the convergence criterion

$$\text{Convergence} \begin{cases} k > n_{damping} \\ max(g_\sigma(\mathbf{x})) \leq \bar{g}_\sigma \\ max(g_{in}(\mathbf{x})) \leq \bar{g}_{in} \\ norm(\mathbf{x}^k - \mathbf{x}^{k-1}) \leq \overline{norm} \end{cases} \tag{104}$$

where $\bar{g}_\sigma$ and $\bar{g}_{in}$ are the limit value for stress and displacement input constraint, and $norm(\mathbf{x}^k - \mathbf{x}^{k-1})$ represents the variation between the variables of the last two iterations, so the optimizer only exits the loop after a constant result between the last two steps. The $\overline{norm}$ value was determined by the author and represents the variation of no more than 10% in the design variables of 5% of the elements in the mesh.

3.4.1 Optimization problem

As stated in the theoretical foundation section, the GCMMA method employs an iterative approach that approximates a non-linear problem to convex functions, bounded by the positions of two set of moving asymptotes and moving limits. In this work we use the GCMMA presented by Gomes-Ruggiero, Sachine and Santos (2011) and implemented through the NLopt.jl package.

Figure 12 – Optimization algorithm flowchart.
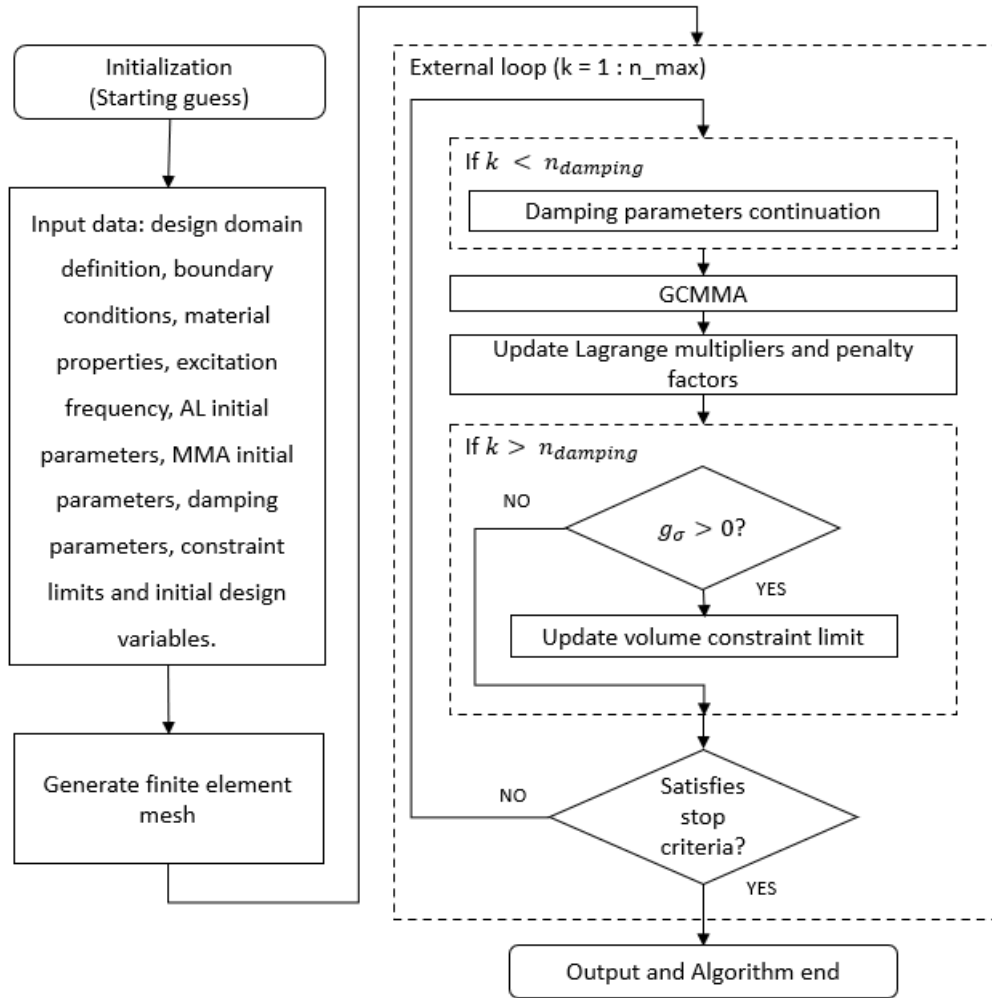
Source: Author production.

The solution of the GCMMA sub-problem is iterative and, although it is not explicit in the computer code developed in this work, represents another internal loop to the main algorithm.

The GCMMA method is employed with the objective function already modified by the AL function. This objective function encapsulates the relationship between input and output displacements in Eq. (88) and the stress constraint outlined in Eq. (82) as shown in

$$
P^k \begin{cases}
\min & L^k(\mathbf{x}) = r_f f^k(\mathbf{x}) + L^k_\sigma(\mathbf{x}) \\
S.t. & \mathbf{K}_D(\mathbf{x})\mathbf{U}(\mathbf{x}) = \mathbf{F}(\mathbf{x}) \\
& g^k_{in}(\mathbf{x}) \leq \bar{g}_{in} \\
& g^k_v(\mathbf{x}) \leq \bar{g}_v \\
& \underline{\mathbf{x}} \leq \mathbf{x}^k \leq \bar{\mathbf{x}}
\end{cases}
\tag{105}
$$

where r_f is a scaling factor to equalize the magnitude of the two terms and

$$L_\sigma^k(\mathbf{x}) = \sum_j^n \frac{c_j^k(\mathbf{x})}{2} \left\langle \frac{\mu_j^k(\mathbf{x})}{c_j^k(\mathbf{x})} + \frac{g_{\sigma_j}^k(\mathbf{x})}{\bar{g}_\sigma} - 1 \right\rangle^2 \tag{106}$$

where n is the number of design variables.

By examining Eq. (88) and noting that the input displacement constraint is usually on the order of mm, we determine that the value of $f(\mathbf{x})$ is approximately 10^{-6} m. Adding to this consideration the possibility of the stress constraint exceeding a unit value, we observe a significant discrepancy in magnitudes between the two terms of $\mathscr{L}^k(\mathbf{x})$. In such scenarios, normalizing $f(\mathbf{x})$ by its initial value, $f^0(\mathbf{x})$, could serve as a method to normalize the first term. However, this adjustment primarily affects the initial iterations. In the case of an inverter mechanism, as iterations progress, $f(\mathbf{x})$ tends towards zero during the inversion process. Hence, alongside the initial normalization, incorporating the scaling factor r_f becomes imperative.

To employ the GCMMA method, as shown in Eq. (54), it is necessary to calculate the functions, AL and constraint functions, at the point of interest and their respective derivatives. The derivatives of the functions intuitively should be with respect to their independent variable $\mathbf{x}$. However, as shown in Eq. 73, this formulation use filtering and projection. Thus, the design variables $\mathbf{x}$ are related to the filtered variables $\tilde{\boldsymbol{\rho}}$, which in turn are related to the relative density variables $\boldsymbol{\rho}$. In this way, we can develop the sensitivity analysis of a function f_i with respect to x_l as

$$\frac{df_i(\mathbf{x})}{dx_l} = \frac{\partial \tilde{\rho}_o}{\partial x_l} \frac{\partial \rho_m}{\partial \tilde{\rho}_o} \frac{df_i(\mathbf{x})}{d\rho_m} \tag{107}$$

with implicit sum in m and o. As the derivatives $\frac{\partial \boldsymbol{\rho}}{\partial \tilde{\boldsymbol{\rho}}}$ and $\frac{\partial \tilde{\boldsymbol{\rho}}}{\partial \boldsymbol{x}}$ are constants matrices, we will present only the derivatives with respect to the relative densities $\frac{df_i(\mathbf{x})}{d\rho_m}$.

The sensitivity analyses is presented separately for the objective function of the GCMMA, represented by the LA function ($L^k(\mathbf{x})$), and for the GCMMA constraints ($g_{in}^k(\mathbf{x})$ and $g_v^k(\mathbf{x})$). Both analyses need the derivative of displacement with respect to relative density $\frac{d\mathbf{U}}{d\rho_m}$, which is computationally expensive. Therefore, in both analyses, the adjoint method is used.

3.4.2 Sensitivity analysis of the AL function

For quantify the sensitivity of the objective function in relation to the design variables, two equilibrium equations will be added to the AL function

$$\Phi(\mathbf{x}) = L(\mathbf{x}) + \frac{1}{2}\boldsymbol{\lambda}_1^T (\mathbf{K}_D(\mathbf{x})\mathbf{U}_D(\mathbf{x}) - \mathbf{F}) + \frac{1}{2}\boldsymbol{\lambda}_2^T (\mathbf{K}_D^*(\mathbf{x})\mathbf{U}_D^*(\mathbf{x}) - \mathbf{F}^*). \tag{108}$$

As demonstrated in Appendix B

$$\frac{d\Phi}{d\rho_m} = \frac{\partial L}{\partial \rho_m} + \Re\left(\boldsymbol{\lambda}^T \frac{d\mathbf{K}_D}{d\rho_m}\mathbf{U} + \boldsymbol{\lambda}^T \frac{d\mathbf{F}^*}{d\rho_m}\right) \tag{109}$$

where $\boldsymbol{\lambda}$ is obtained by solving the adjoint problem

$$\mathbf{K}_D \boldsymbol{\lambda} = \left(i\frac{\partial L}{\partial \mathbf{U}_I} - \frac{\partial L}{\partial \mathbf{U}_R}\right). \tag{110}$$

In this way, the adjoint problem is evaluated by grouping all partial derivatives. In the next subsections, the components of the adjoint problem of the objective function $f(\mathbf{x})$ and the stress constraint $L_\sigma^k(\mathbf{x})$ will be presented.

3.4.2.1 Objective function

The partial derivative of the objective function presented in Eq. (88) can be expressed as

$$\frac{df(\mathbf{x})}{d\rho_m} = \frac{d}{d\rho_m}\left(u_{in_R}(\mathbf{x})u_{out_R}(\mathbf{x}) + u_{in_I}(\mathbf{x})u_{out_I}(\mathbf{x})\right), \tag{111}$$

or

$$\frac{df(\mathbf{x})}{d\rho_m} = \frac{du_{in_R}}{d\rho_m}u_{out_R} + u_{in_R}\frac{du_{out_R}}{d\rho_m} + \frac{du_{in_I}}{d\rho_m}u_{out_I} + u_{in_I}\frac{du_{out_I}}{d\rho_m}. \tag{112}$$

Using localization vectors $u_{in} = \mathbf{L}_{in}^T\mathbf{U}$ and $u_{out} = \mathbf{L}_{out}^T\mathbf{U}$

$$\frac{df(\mathbf{x})}{d\rho_m} = \mathbf{L}_{in}^T\frac{d\mathbf{U}_R}{d\rho_m}u_{out_R} + u_{in_R}\mathbf{L}_{out}^T\frac{d\mathbf{U}_R}{d\rho_m} + \mathbf{L}_{in}^T\frac{d\mathbf{U}_I}{d\rho_m}u_{out_I} + u_{in_I}\mathbf{L}_{out}^T\frac{d\mathbf{U}_I}{d\rho_m} \tag{113}$$

such that

$$\frac{df(\mathbf{x})}{d\rho_m} = \underbrace{\left(u_{out_R}\mathbf{L}_{in}^T + u_{in_R}\mathbf{L}_{out}^T\right)}_{\frac{\partial f}{\partial \mathbf{U}_R}^T}\frac{d\mathbf{U}_R}{d\rho_m} + \underbrace{\left(u_{out_I}\mathbf{L}_{in}^T + u_{in_I}\mathbf{L}_{out}^T\right)}_{\frac{\partial f}{\partial \mathbf{U}_I}^T}\frac{d\mathbf{U}_I}{d\rho_m}. \tag{114}$$

Substituting the terms of Eq. (114) into Eq. (110) results in

$$\mathbf{K}_D\boldsymbol{\lambda}_f = i\left(u_{out_I}\mathbf{L}_{in}^T + u_{in_I}\mathbf{L}_{out}^T\right) - \left(u_{out_R}\mathbf{L}_{in}^T + u_{in_R}\mathbf{L}_{out}^T\right) \tag{115}$$

or

$$\mathbf{K}_D\boldsymbol{\lambda}_f = -u_{in}^*\mathbf{L}_{out}^T - u_{out}^*\mathbf{L}_{in}^T \tag{116}$$

where $\boldsymbol{\lambda}_f$ is adjoint vector associated to the objective function.

3.4.2.2 Stress constraint

Rewriting Eq. (106) with terms related to the stress variables

$$L_\sigma = \sum_e \frac{c_e}{2n_e} \left\langle \frac{\mu_e}{c_e} + \frac{\sigma_e}{\bar{\sigma}} - 1 \right\rangle^2, \tag{117}$$

where it is assumed that each element has an associated stress constraint.

The sensitivity of L_σ with respect to a design variable ρ_m is

$$\frac{dL_\sigma}{d\rho_m} = \sum_e \frac{c_e}{4n} \left\langle \frac{\mu_e}{c_e} + \frac{\sigma_e}{\bar{\sigma}} - 1 \right\rangle \frac{1}{\bar{\sigma}} \frac{d\sigma_e}{d\rho_m}. \tag{118}$$

The stress state at a point, in Voigt notation, is given by

$$\boldsymbol{\sigma}_e = f_e(1 + i\omega\beta)\mathbf{S}_e \left(\mathbf{U}_R + i\mathbf{U}_I\right) \tag{119}$$

where

$$\mathbf{S}_e = \mathbf{C}_e \mathbf{B}_e \mathbf{A}_e \mathbf{H}_e. \tag{120}$$

The relaxation function f_e is given, in the QP relaxation, by

$$f_e = \rho_e^{p-q}, \tag{121}$$

with $q < p$.

Expanding the stress into its real and imaginary components

$$\boldsymbol{\sigma}_e = f_e \mathbf{S}_e \left(\mathbf{U}_R - \beta\omega\mathbf{U}_I\right) + i f_e \mathbf{S}_{ek(\mathbf{U}_I + \beta\omega\mathbf{U}_R)} \tag{122}$$

with

$$\boldsymbol{\sigma}_e = \boldsymbol{\sigma}_{eR} + i\boldsymbol{\sigma}_{eI}. \tag{123}$$

As the equivalent stress is

$$\sigma_e = \sqrt{\boldsymbol{\sigma}_e^H \mathbf{V} \boldsymbol{\sigma}_e} \tag{124}$$

and the stress is complex, we observe that

$$\sigma = \sqrt{\boldsymbol{\sigma}_R^T \mathbf{V} \boldsymbol{\sigma}_R + \boldsymbol{\sigma}_I^T \mathbf{V} \boldsymbol{\sigma}_I} \tag{125}$$

and the indices $_e$ are dropped to simplify the notation. Thus, the equivalent stress is denoted by σ (without bold) and the stress state by $\boldsymbol{\sigma}$.

Proceeding with the derivative of the equivalent stress

$$\frac{d\sigma}{d\rho_m} = \frac{1}{\sigma}\left(\boldsymbol{\sigma}_R^T \mathbf{V}\frac{d\boldsymbol{\sigma}_R}{d\rho_m} + \boldsymbol{\sigma}_I^T \mathbf{V}\frac{d\boldsymbol{\sigma}_I}{d\rho_m}\right),$$ (126)

since $\mathbf{V}$ is symmetric. The derivatives of the components of the stress state, Eq. (122), are

$$\frac{d\boldsymbol{\sigma}_R}{d\rho_m} = \frac{df_e}{d\rho_m}\mathbf{S}\left(\mathbf{U}_R - \beta\omega\mathbf{U}_I\right) + f_e\mathbf{S}\left(\frac{d\mathbf{U}_R}{d\rho_m} - \beta\omega\frac{d\mathbf{U}_I}{d\rho_m}\right)$$ (127)

and

$$\frac{d\boldsymbol{\sigma}_I}{d\rho_m} = \frac{df_e}{d\rho_m}\mathbf{S}\left(\mathbf{U}_I + \beta\omega\mathbf{U}_R\right) + f_e\mathbf{S}\left(\frac{d\mathbf{U}_I}{d\rho_m} + \beta\omega\frac{d\mathbf{U}_R}{d\rho_m}\right).$$ (128)

So, we obtain

$$\frac{dL_\sigma}{d\rho_m} = \sum_e \frac{c_e}{4n}\left\langle\frac{\mu_e}{c_e} + \frac{\sigma_e}{\overline{\sigma}} - 1\right\rangle\frac{1}{\overline{\sigma}}\frac{1}{\sigma_e}\frac{df_e}{d\rho_m}\left(\boldsymbol{\sigma}_R^T\mathbf{VSU}_R - \right.$$
$$\left.\beta\omega\boldsymbol{\sigma}_R^T\mathbf{VSU}_I + \boldsymbol{\sigma}_I^T\mathbf{VSU}_I + \omega\beta\boldsymbol{\sigma}_I^T\mathbf{VSU}_I\right),$$ (129)

which can be simplified to

$$\frac{dL_\sigma}{d\rho_m} = \sum_e \frac{c_e}{4n}\left\langle\frac{\mu_e}{c_e} + \frac{\sigma_e}{\overline{\sigma}} - 1\right\rangle\frac{1}{\overline{\sigma}}\frac{df_e}{d\rho_m}\frac{1}{f_e}\sigma_e.$$ (130)

The partial derivatives with respect to displacement are

$$\frac{dL_\sigma}{\partial\mathbf{U}_R}^T = \sum_e \frac{c_e}{4n}\left\langle\frac{\mu_e}{c_e} + \frac{\sigma_e}{\overline{\sigma}} - 1\right\rangle\frac{1}{\overline{\sigma}}\frac{1}{\sigma_e}f_e\left(\boldsymbol{\sigma}_R^T\mathbf{VS} + \beta\omega\boldsymbol{\sigma}_I^T\mathbf{VS}\right)^T$$ (131)

and

$$\frac{\partial L_\sigma}{\partial\mathbf{U}_I}^T = \sum_e \frac{c_e}{4n}\left\langle\frac{\mu_e}{c_e} + \frac{\sigma_e}{\overline{\sigma}} - 1\right\rangle\frac{1}{\overline{\sigma}}\frac{1}{\sigma_e}f_e\left(\boldsymbol{\sigma}_I^T\mathbf{VS} - \beta\omega\boldsymbol{\sigma}_R^T\mathbf{VS}\right)^T.$$ (132)

After some simplifications,

$$\mathbf{K}_D\boldsymbol{\lambda}_\sigma = -\sum_e \frac{c_e}{4n}\left\langle\frac{\mu_e}{c_e} + \frac{\sigma_{ek}}{\overline{\sigma}} - 1\right\rangle\frac{1}{\overline{\sigma}}\frac{1}{\sigma_e}f_e(1 + i\omega\beta)\boldsymbol{\sigma}_e^H\mathbf{VS}_e.$$ (133)

The part related to stress constraints can be grouped into adjoint problem of the LA function of the GCMMA through the Eq. (110) since the adjoint problem is linear.

3.4.3 Sensitivity analysis of the GCMMA constraints

In this study, GCMMA incorporates constraints on input displacement and volume presented in Eq. (80) and (81).

3.4.3.1 Volume constraint

The derivative of the volume constraint can be defined through

$$\frac{dg_v(\mathbf{x})}{d\rho_m} = \frac{\partial g_v(\mathbf{x})}{\partial \rho_m} + \frac{\partial g_v^T(\mathbf{x})}{\partial \mathbf{U}_R}\frac{d\mathbf{U}_R}{d\rho_m} + \frac{\partial g_v^T(\mathbf{x})}{\partial \mathbf{U}_I}\frac{d\mathbf{U}_I}{d\rho_m}. \tag{134}$$

as the volume is independent of displacements, and the volume of each element depends only on the relative density variable of the element

$$\frac{dg_v(\mathbf{x})}{d\rho_m} = \frac{\sum_e \frac{d\rho_e}{d\rho_m}v_e}{\bar{v}} = \frac{v_m}{\bar{v}}. \tag{135}$$

3.4.3.2 Displacement constraint

The derivative of the input displacement constraint can be defined through

$$\frac{dg_{in}(\mathbf{x})}{d\rho_m} = \frac{1}{\bar{u}|u_{in}|}\left(u_{in_R}\frac{du_{in_R}}{d\rho_m} + u_{in_I}\frac{du_{in_I}}{d\rho_m}\right). \tag{136}$$

Using a localization vector $\mathbf{L}_{in}^T$

$$\frac{dg_{in}(\mathbf{x})}{d\rho_m} = \frac{1}{\bar{u}|u_{in}|}\left(u_{in_R}\mathbf{L}_{in}^T\frac{d\mathbf{U}_R}{dx_m} + u_{in_I}\mathbf{L}_{in}^T\frac{d\mathbf{U}_I}{dx_m}\right) \tag{137}$$

such that

$$\frac{\partial g_{in}(\mathbf{x})}{\partial \mathbf{U}_R} = \frac{1}{\bar{u}|u_{in}|}u_{in_R}\mathbf{L}_{in}^T, \tag{138}$$

$$\frac{\partial g_{in}(\mathbf{x})}{\partial \mathbf{U}_I} = \frac{1}{\bar{u}|u_{in}|}u_{in_I}\mathbf{L}_{in}^T \tag{139}$$

and

$$\frac{\partial g_{in}(\mathbf{x})}{\partial \rho_m} = 0. \tag{140}$$

Using the same formulation presented in Eq. (110), we obtain the expression for the adjoint problem of the constraints of GCMMA

$$\mathbf{K}_D\boldsymbol{\lambda}_{g_{in}} = \left(i\frac{1}{\bar{u}|u_{in}|}u_{in_I}\mathbf{L}_{in}^T - \frac{1}{\bar{u}|u_{in}|}u_{in_R}\mathbf{L}_{in}^T\right) \tag{141}$$

or

$$\mathbf{K}_D\boldsymbol{\lambda}_{g_{in}} = \frac{-u_{in}^*}{\bar{u}|u_{in}|}\mathbf{L}_{in}^T. \tag{142}$$

4 RESULTS AND DISCUSSIONS

In this section, the results of the proposed formulation will be presented. The test case of the design of an inverter mechanism is used to assess the formulation, specially the inversion between inputs and outputs. Figure 8 presents the classic inverter mechanism, with the input and output regions, as well as symmetry and boundary conditions. The force and output springs are distributed to better represent the interactions with the external media. The domain Ω has n_f non design elements with fixed relative densities of $\rho = 1$ (solid). The regions around the input force, output and the upper left boundary conditions are not considered in the evaluation of the local stress constraints, since these regions may present artificial stress concentration. Thus, the color maps showing the stress constraints present null values in these regions.

Figure 13 – Boundary conditions of the inverter mechanism.
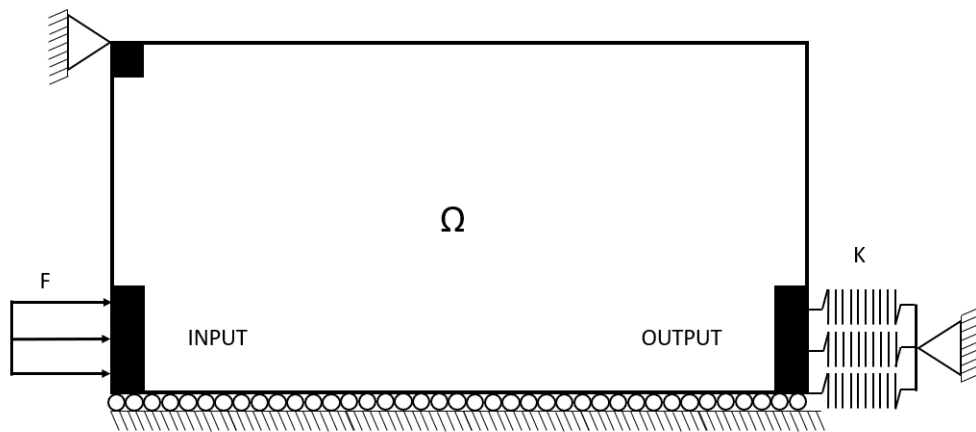
Source: Author production.

The parameters defining the domain, material and boundary conditions are shown in Table 1. Table 2 outlines the constraint limit values, relaxation and damping parameters. Table 3 lists the initial parameters regarding the optimization (some different values can be used for specific examples and are presented along the text).

The notation $a\mathbf{1}$ is used in this chapter to represent a vector with all entries equal to a.

A series of analyses were conducted to assess the behavior of proposed formulation under different conditions. These will be presented in the respective order:

- analysis of the inclusion of adaptive volume constraint in the formulation,

- evaluation of the behavior of the formulation regarding different starting points,

- comparison of results for different frequencies, and

- evaluation of behavior upon relaxation of constraints.

A common procedure when evaluating the performance of topology optimization formulations and computer implementations is to show the convergence plots for the objective

Table 1 – Geometry and mesh parameters.

Variable	Value	Description
n_x	180	Divisions along the length
n_y	90	Divisions along the height
L_x	1.0×10^{-1} m	Domain length
L_y	5.0×10^{-2} m	Domain height
L_z	5.0×10^{-3} m	Thickness
n_e	1.62×10^4	Number of elements in domain
n_f	7	Number of fixed elements (filled) in the domain
E	3.0×10^9 Pa	Young's modulus
ν	0.4	Poisson coefficient
F_{in}	2.0×10^2 N	Total input force
K_{out}	1.0×10^5 N/m	Total output stiffness

Table 2 – Fixed and initial parameters.

Variable	Value	Description
$\bar{u}_{in}$	2.0×10^{-3} m	Limit input displacement
$\bar{v}_{initial}$	3.0×10^{-1}	Initial limit volume fraction
$\bar{v}_{min}$	1.5×10^{-1}	Minimum limit volume fraction
$\bar{\sigma}$	40.0 MPa	Yield (limit) stress
ζ_{ini}	3.0×10^{-1}	Initial value for the damping ratio (ζ)
ζ_{tar}	2.0×10^{-2}	Target value for ζ
p	3.0	SIMP exponent
q	1.5	Stress relaxation exponent
β_p	1.0	Adjust factor for the Heaviside projection

Table 3 – Parameters used in the optimization.

Variable	Value	Description
R	0.0025	Spatial filter's radius
$\mathbf{x}_{initial}$	$\bar{v}_{initial}\mathbf{1}$	Vector of initial design variables
$n_{damping}$	15	Number of iterations for continuation of damping
n_{max}	2.0×10^2	Number of external iterations in the LA
n_{GCMMA}	1.0×10^3	Number of internal iterations in the optimizer
$\mathbf{c}_{initial}$	$(1.0 \times 10^1)\mathbf{1}$	AL initial penalty vector
$\mathbf{c}_{max}$	$(1.0 \times 10^3)\mathbf{1}$	AL maximum penalty vector
$\boldsymbol{\mu}_{initial}$	$(0.0)\mathbf{1}$	AL initial multipliers vector
r_c	1.1	Penalty increase rate
r_f	1.0×10^3	Objective function adjustment factor
r_v	5.0×10^{-3}	Rate of decrease in volume fraction
$\bar{g}_\sigma$	1.0×10^{-3}	Limit value for stress constraint
$\bar{g}_{in}$	1.0×10^{-3}	Limit value for input displacement constraint
$\overline{norm}$	6.36×10^{-1}	Limit value for norm between the design variables

functions and/or the constraints along the iterations of the optimization. This is hard to show in the formulation used in this work, since there are external iterations (associated to the Augmented Lagrangian Method) and internal iterations (associated to the GCMMA). To make things worst,

the mathematical nature of the joint objective function L^k changes between two external iterations (LA), since the penalties and the Lagrange multipliers are changed to account for the constraint violation. Thus, there is no guarantee of a steady decrease in the joint objective function L^k associated to the LA. Also, as the internal optimization problem (GCMMA) is solved by using an external library, we have no access to its internal iteration history. Thus, the convergence graphs are not shown herein.

4.1 ADAPTIVE VOLUME CONSTRAINT

The first analysis presented aims to analyze the behavior of the adaptive volume constraint in the formulation presented in Eq. (105). An excitation frequency of 300 Hz is used to compare the traditional fixed volume constraint and the proposed approach. The results for other frequencies are shown in Appendix C.

4.1.1 Fixed volume constraint

Table 4 shows the distributions of design variables and stress constraint values in some selected iterations. It can be seen a smooth change in the material distribution throughout the iterations. In all these topologies, the material is concentrated in the "arm" that connects the mechanism to the output port. There are two regions of lumped compliance in the extremities of this "arm", with higher stresses than the surrounding. This material concentration in the stiffer "arm" is used by the optimizer to distribute the "excess" of material without compromising the CM.

Table 4 – Topologies and distribution of stress constrains for 300 Hz without volume fraction variation.

Iteration	$k = 15$	$kS = 30$	$k = 68$
Distribution of ρ in domain			
Distribution of g_σ			
Scale			
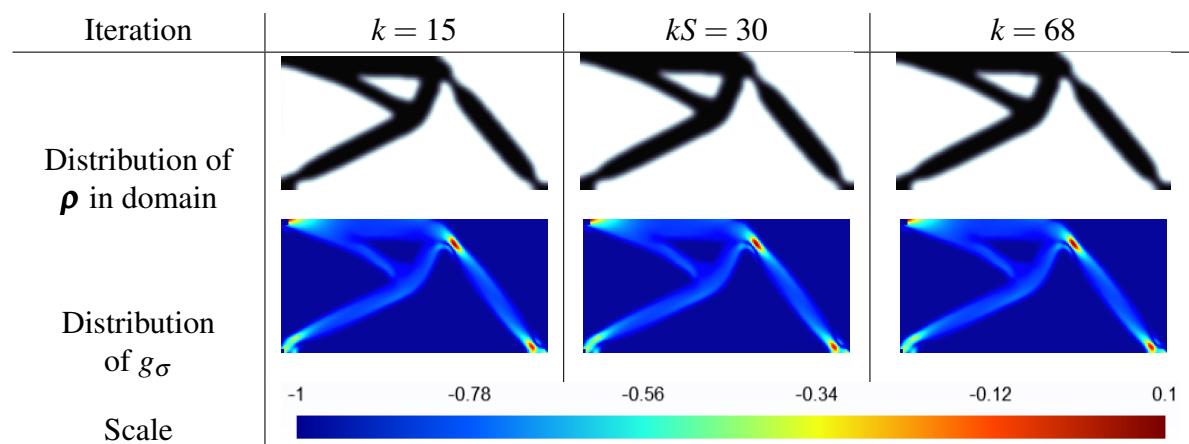
Source: Author production.

The optimization process generates changes in the material distribution at each iteration to satisfy all constraints and minimize the objective function. Iterations 15 and 30, presented in Table 4, show mechanisms that have the volume and displacement constraints satisfied (constraints directed applied in GCMMA), but with the stress constraint violated (constraints

included in the formulation using the LA). Iteration 68 presents a mechanism satisfying all imposed constraints, with objective function of $-2.97 \times 10^{-6} m^2$. However, it is evident that the two regions of lumped stress persisted throughout the optimization process.
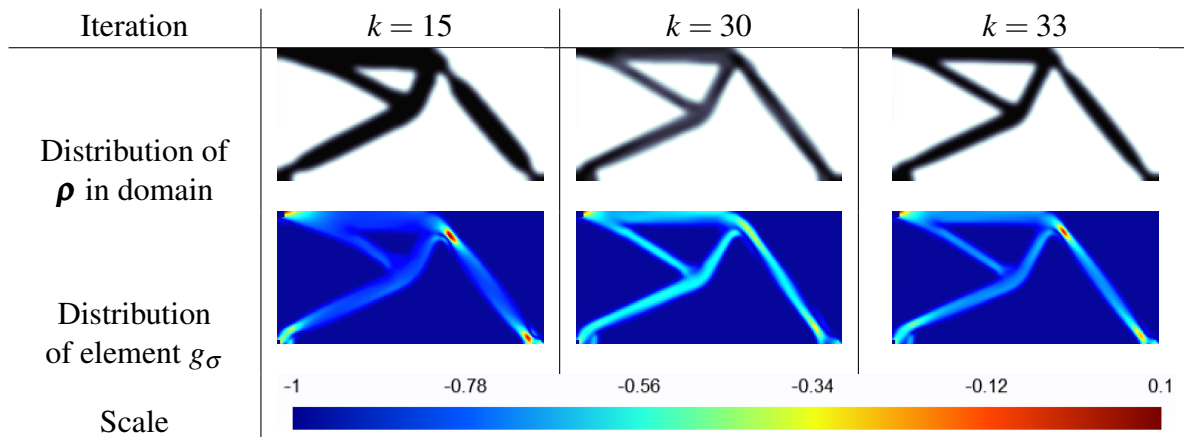
One of the known issues in topology optimization with fixed volume constraint is the fact that the designer does not know the ideal limit $\bar{v}$ in advance. Thus, some trial and error are commonly used to assess a proper value. The topology depicted in the last column of Tab. 4 has large amount of material in regions with low stress levels (negative values of g_σ), attesting that the upper limit used in this case may be excessive. The use of these stiff regions allows the optimizer to use some regions with lumped compliance, maximizing the output displacement but hindering the design of a fully compliant mechanism.

4.1.2 Adaptive volume constraint

Table 5 presents the material distribution and stress constraint for the same frequency of 300 Hz used in the previous example, but using the adaptive volume constraint.

The results in the first column ($k = 15$) of Tab. 4 and Tab. 5 are the same, since the adaptivity starts after iteration 15. From iteration $n_{damping}$ onward, only the stress constraint had not been satisfied, prompting the optimizer to gradually reduce the threshold volume fraction $\bar{v}$ until convergence at iteration 33, with $\bar{v} = 0.235$.

Table 5 – Topologies and distribution of stress constrains with excitation frequency of 300 Hz and adaptive volume constraint.

Iteration	$k = 15$	$k = 30$	$k = 33$
Distribution of ρ in domain			
Distribution of element g_σ			
Scale			

Source: Author production.

The optimized objective function value is $-2.74 \times 10^{-6} m^2$, very close to the one obtained in the previous analysis. Despite the close objectives, one can observe a significant change in the material distribution and the consequent distribution of compliance as the limit volume fraction decreases. Other consequence is the smoother stress distribution.

Furthermore, a result with significant computational gains was obtained, as in 33 iterations the optimizer was already able to meet all its stopping criteria, while the previous analysis required 68 iterations. It is possible to highlight that the region of concentrated compliance still exists and represents the region with the highest stress value, as it reflects a characteristic of

the proposed objective function. However, this modification provided a much more uniform distribution of strain energy and, consequently, stress.

The same analysis carried out in this section was performed for frequencies of: 0, 100, 200, 400, 500Hz and 600 Hz and are presented in the Appendix C, where it is possible to observe the behavior of the 300 Hz test case.
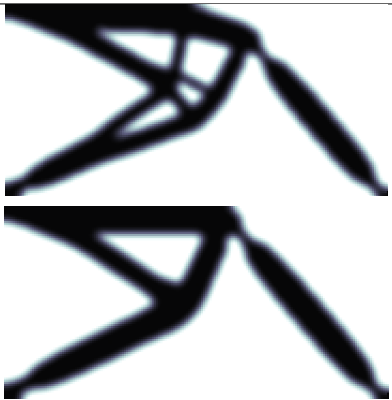
4.2 NON-CONVEX PROBLEM

Topology optimization typically exhibits a non-convex nature, implying that there may exist more than one viable solution or what we refer to as local minima. Therefore, depending on the chosen initial values, $\mathbf{x}_{initial}$, different final topologies can be obtained (SILVA, 2017). Additionally, another source of non-convexity for our formulation is the local stress constraint (SELTMANN; HASSE, 2023). Therefore, the formulation proposed in this work may encounter different local minima depending on the initial design variables.

The results presented in the previous sections used the initial values presented in Table 3, where $\mathbf{x}_{initial} = \mathbf{1}\bar{v}_{initial}$. To evaluate non-convexity, the optimization process will be carried out for the vector of design variables starting at $\mathbf{1}$ and $\mathbf{1}\bar{v}_{initial}$. Additionally, we will present the results separately for fixed and variable volume constraints to ensure that volume adaptivity does not influence our evaluation.

Tables 6 and 7 present the CMs obtained for 100 Hz. Table 6 shows the results for fixed volume fraction and Tab. 7 the results using the adaptive volume constraint. Both mechanisms satisfy the input displacement constraint ($|u_{in}| = \bar{u}_{in}$).

Table 6 – Topologies with excitation frequency of 100 Hz and initial design variables without adaptive volume constraint.

$\mathbf{x}_{initial}$	$f(x)[m^2]$	$max(g_\sigma)$	Distribution of ρ in domain
$\mathbf{1}$	-2.76×10^{-6}	2.80×10^{-1}	
$\mathbf{1}\bar{v}_{initial}$	-2.80×10^{-6}	1.23×10^{-1}	

Source: Author production.

Table 6 shows two mechanisms that reached the maximum number of iterations n_{max} while satisfying the volume constraint but violating the stress constraint. Despite having different

Table 7 – Topologies with excitation frequency of 100 Hz and initial design variables with adaptive volume constraint.

$\mathbf{x}_{initial}$	$f(x)[m^2]$	$max(g_\sigma)$	$\bar{v}_{final}$	Distribution of $\boldsymbol{\rho}$ in domain
1	-2.57×10^{-6}	$g_\sigma < 0$	0.235	
$\mathbf{1}\bar{v}_{initial}$	-2.63×10^{-6}	$g_\sigma < 0$	0.240	

Source: Author production.

stress constraint violation values, they present the same regions with lumped compliance (and stress).

Table 7 shows two different designs that successfully met the volume and stress constraints. Both designs show a much improved compliance distribution, obtained due to the reduction in $\bar{v}$ when compared to the results obtained without the adaptive constraint.

Harmonic analyses were performed to assess the dynamic behavior of the results presented in Table 7. These analyses spanned frequencies from 0 to 1000 Hz, using the parameters in Table 1 and 2. Figure 14 illustrates the objective function, Eq. (98), computed for each harmonic analysis (frequency). Figure 14 depicts overlapping behaviors of the two mechanisms, indicating that despite presenting different designs, they manifest the same objective function behavior.

The results show that despite the non-convex formulation, the variation of the initial design variables did not present significant variations in the objective function obtained by the mechanisms. Therefore, the other topologies presented will be developed from the initial variable vector

$$\mathbf{x}_{initial} = \mathbf{1}\bar{v}_{initial}. \tag{143}$$

However, as shown previously, the present work uses a non-convex formulation and the variation of the initial design variable vector may be a necessary resource for the design of CM.

Figure 14 – Harmonic response graph of the objective function applied to the mechanisms presented in Table 7 with the design variable vectors ($\mathbf{x}_{initial}$): A equal to **1** and B equal to $\mathbf{1}\bar{v}_{initial}$.
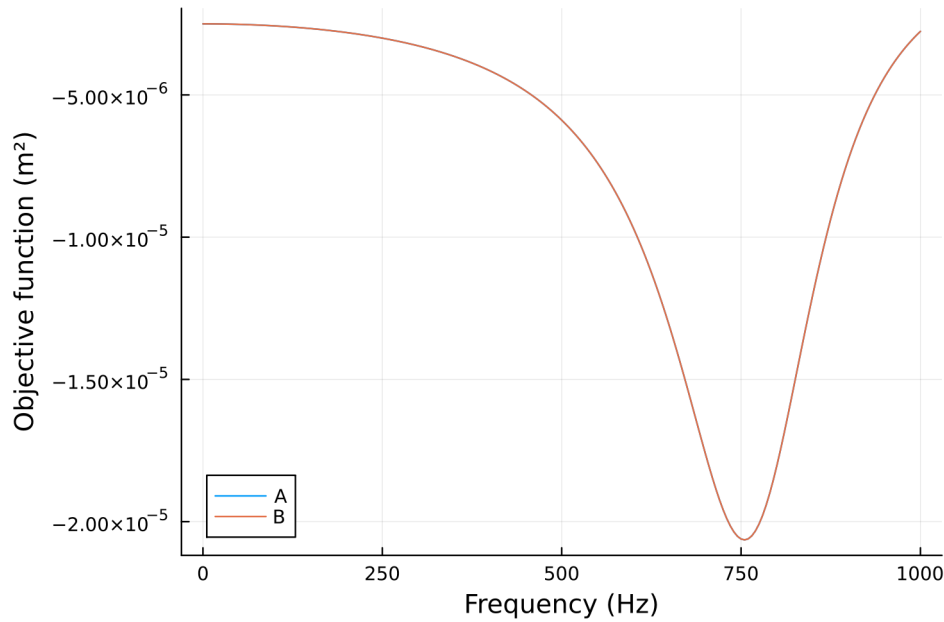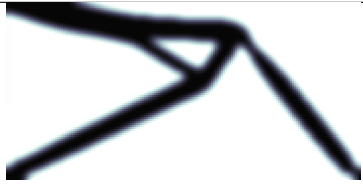

Source: Author production.

4.3 COMPARISON AMONG FREQUENCIES

This work aims to present a formulation for the design of CMs subject to harmonic regimes. Based on this premise, the set of frequencies at which it will be evaluated is relevant information. To define the range of analysis, we use TO for static case as a reference.

This optimization utilized the parameters presented in Table 1, 2 and 3, and the excitation frequency of the input force is 0 Hz. Table 8 presents the compilation of this result, which show the satisfaction of constraints with volume adaptive and objective function minimization.

Table 8 – Topology optimization results for the static case.

$f(x)[m^2]$	$|u_{in}|[m]$	$\bar{v}_{final}$	$max(g_\sigma)$	Distribution of $\boldsymbol{\rho}$ in domain
-2.67×10^{-6}	2.00×10^{-3}	0.225	$g_\sigma(\mathbf{x}) < 0$	

Source: Author production.

The first vibration modes and frequencies of this mechanism were obtained through a modal analysis. The first vibration mode of the mechanisms manifests the movement reversal behavior, which constitutes the focus of this study. Figure 15 shows the undeformed and deformed mechanism for the first vibration frequency of 693.8 Hz. As the initial objective of the formulation, we chose to study 'low frequencies', a term that in this work will be defined

as frequencies below the first natural frequency of the reference mechanism. Therefore, this study will focus its evaluation on excitation frequencies ranging from 0 to 600 Hz. The analysis will be performed in 100 Hz intervals, as illustrated in Table 9.

Figure 15 – Inverter mechanism for the static case: (a) undeformed and (b) deformation mode of the first natural frequency.

<div align="center">(a)   (b)</div>
<div align="center">Source: Author production.</div>

All presented results use adaptive volume fraction constraint and satisfy the input displacement, the volume and the stress constraints. Also, the first mode for all designs show the inversion behavior between the input and the output.
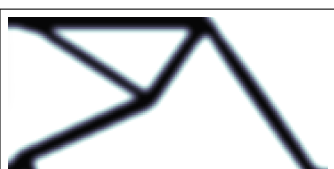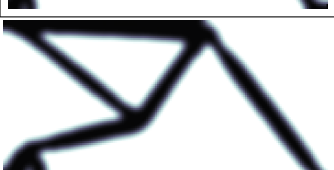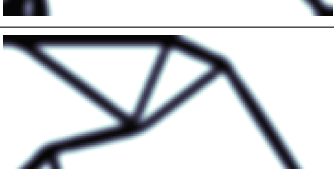
The CMs presented in Table 9 were obtained with the standard parameters (Tables 1, 2 and 3) with the exception of the 400 and 600 Hz cases, which will be analyzed separately in the next subsection.

One can observe that despite different excitation frequencies, Table 9 shown highly similar topologies and, furthermore, very close objective functions. This fact becomes even more evident when analyzing Figure 16, which illustrates the behavior of the mechanisms through harmonic analysis over a wide range of frequencies.

As the main goal when designing a CM is to maximize the displacement, one obvious consequence in harmonic problems would be to closely match the excitation frequency with one of the resonance frequencies of the optimized topology. Nonetheless, when designing an inverter, the optimizer must also use some vibration mode with the intended inversion between the input and the output. This condition, alone, restricts the set of modes that the optimizer can use during the optimization. Another important question when matching the excitation frequency with some of the resonance frequencies of the optimized system is the fact that the input displacements and the stresses can also be amplified, thus violating the constraints. This is specially important in low frequencies, since the vibration modes tend to be more global when compared to higher frequencies. Thus, the resonance will amplify both the output and the input displacement, as well as the stresses, at the same time (Fig. 9).

This behavior can be observed in the sweep shown in Fig. 16. The objective function for each design of Tab. 9 is evaluated in the frequency range from 0 to 1000 Hz. It can be seen that all the designs are far away from the first resonance frequency (the first natural frequency for each design is shown alongside the excitation frequency). Also, the mechanisms exhibit very small objective functions compared to values near their resonance frequencies. The reason why

Table 9 – Comparison of topology optimization results for different frequencies.

Freq. (Hz)	$f(x)[m^2]$	$\bar{v}_{final}$	r_f	$\mathbf{c}_{initial}$	Distribution of $\boldsymbol{\rho}$ in domain
0 (static)	-2.48×10^{-6}	0.225	1×10^3	$(1 \times 10^1)\mathbf{1}$	
100	-2.57×10^{-6}	0.235	1×10^3	$(1 \times 10^1)\mathbf{1}$	
200	-2.67×10^{-6}	0.240	1×10^3	$(1 \times 10^1)\mathbf{1}$	
300	-2.74×10^{-6}	0.235	1×10^3	$(1 \times 10^1)\mathbf{1}$	
400	-2.45×10^{-6}	0.195	$\boxed{1 \times 10^0}$	$(1 \times 10^1)\mathbf{1}$	
500	-3.05×10^{-6}	0.235	1×10^3	$(1 \times 10^1)\mathbf{1}$	
600*	-2.38×10^{-6}	0.185	1×10^3	$\boxed{(5 \times 10^1)\mathbf{1}}$	

*The results presented for a frequency of 600 Hz were obtained with $\mathbf{x}_{initial} = \mathbf{1}$.
Source: Author production.

all the designs are not close to the first resonance is due to the constraint satisfaction, since all constraints are active at the optimum.

Figure 17 illustrates the input and output displacement curves for the mechanism obtained for 200 Hz. The limit imposed by the input displacement constraint is clearly discernible.

In addition to the displacement constraint, the volume and stress constraints were also active at the optimum in all cases. This fact is corroborated by the values of the final volume fraction and the maximum stresses of the mechanism, both equal to or very close to their defined limits.

Figure 16 – Objective function resulting from the harmonic analysis of the mechanisms in Table 9 in the frequency range from 0 to 1000 Hz. The natural frequency of the design is shown alongside each excitation frequency.
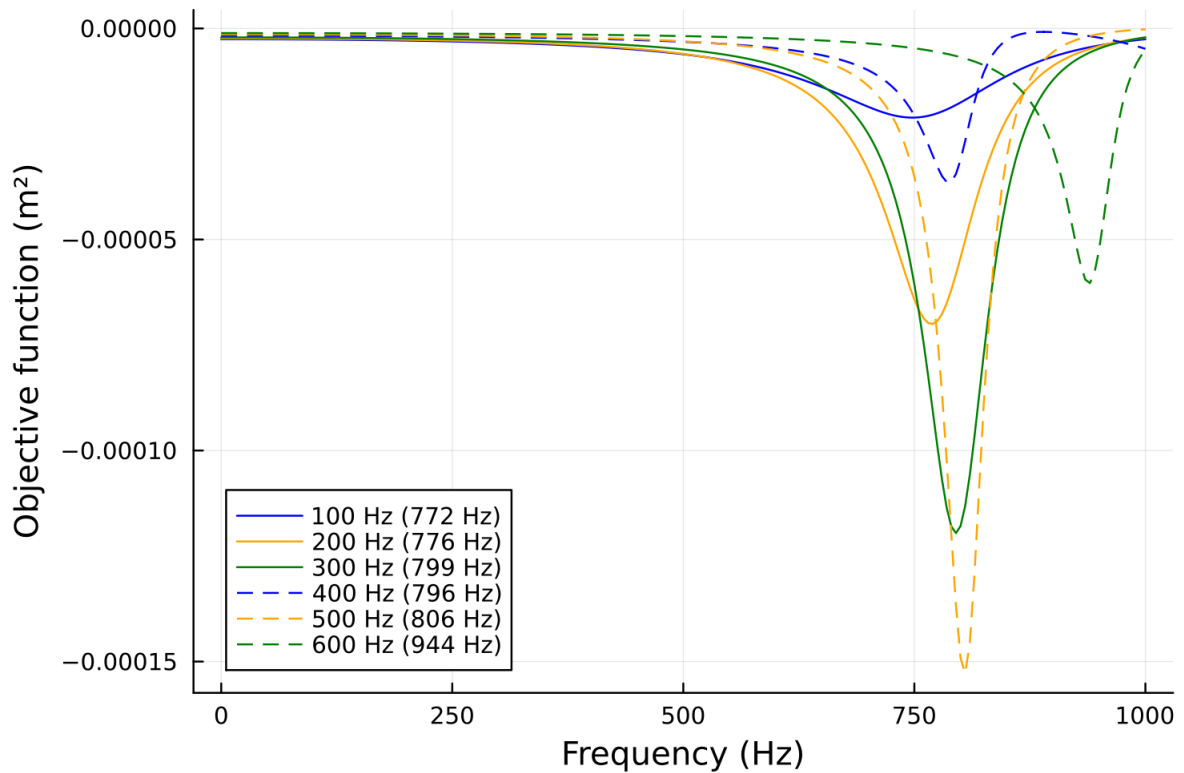
Source: Author production.

The results for 400Hz and 600Hz were obtained with some modified initial parameters. The investigation performed to obtain these parameters is explained in the following.

4.3.1 Parameter tuning for 400Hz and 600Hz

It is common for some adjustments to be necessary in formulations that have constants arbitrarily chosen by the user.

Analysis at 400 Hz required modifications to the value of r_f to achieve a continuous topology. The results of this analysis with standard and modified values are presented in Table 10, were each row corresponds to a different value of r_f. The first result (row 1), obtained with the default values, showed apparently different behavior from the subsequent two. The parameters in the last row lead to the successful design.

Interestingly, the first three designs shown similar material distributions in the first iterations.

The result in the first row was initially driven by the stress constraints and, consequently, the volume adaptive constraint was activated. Thus, the first topology had its volume fraction reduced to the minimum value $\bar{v}_{min}$ without being able to form a continuous mechanism.

The second and third rows show a very small value of the objective function, since the output displacement is close to zero. Interestingly, the design satisfies the constraints and

Figure 17 – Harmonic displacements for the mechanisms obtained for an excitation frequency of 200 Hz.
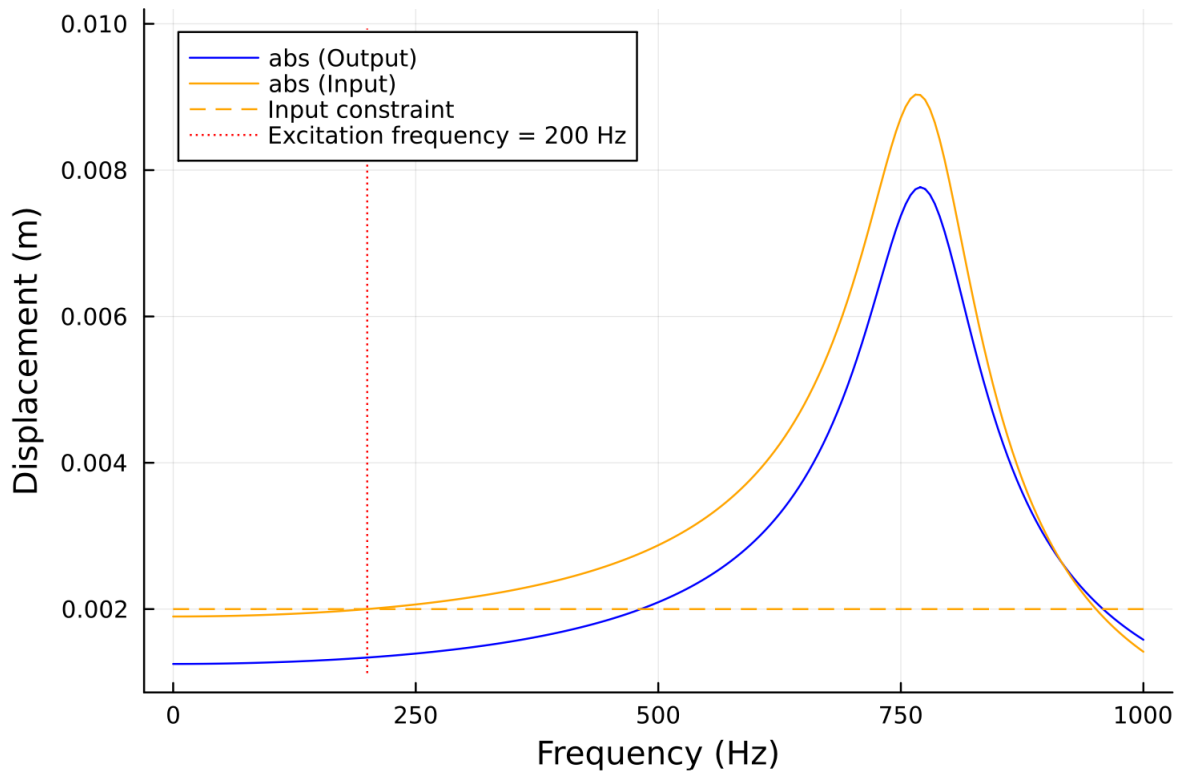
Source: Author production.

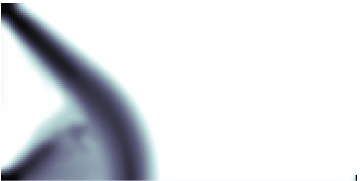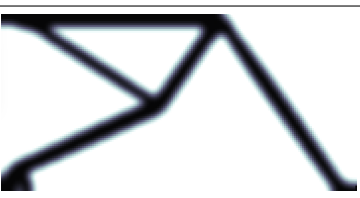converge in few iterations ($k = n_{damping}$).

The value r_f is used in the Augmented Lagrangian, Equation (105), where it acts as the weight of the objective function when summed to the stress constraint terms. Its value can change the relative importance of the objective function and the stress constraints. Thus, different values can lead to different behaviors regarding the optimization. In the second and in the third rows, the optimizer gave more importance to the objective function, but the initial point and the driving frequency lead to very small displacements in the first iterations. The stresses are also satisfied in the first iteration, such that the second term of the LA is zero. Thus, the optimizer gave a large weight to a zero function and the optimization converged to a local minima.

The result in the fourth row has the smallest value of r_f, thus giving less importance to the initial displacements.

Table 11 presents two valid mechanisms for the frequency of 400 Hz. The first is the same as previously presented in Table 10, while the second is a new result obtained by modifying the initial starting point (vector of design variables). Both designs are feasible, with very similar shapes.

Table 12 presents the results for 600 Hz. The first row of Table 12 showcases the outcomes obtained with the parameters used in previous analyses (Tables 1, 2, and 3). It can be observed that the distribution formed a continuous mechanism, respecting the input displacement and volume constraints but violating the stress constraint.

Table 10 – Results of topology optimization for the 400 Hz frequency varying the adjustment factor (r_f).

$f(\mathbf{x})[m^2]$	$\overline{v}_{final}$	r_f	$max(g_\sigma)$	Distribution of $\boldsymbol{\rho}$ in domain
-2.20×10^{-6}	0.150	1×10^3	1.25×10^1	
-2.60×10^{-14}	0.300	1×10^2	$g_\sigma(\mathbf{x}) < 0$	
-4.39×10^{-15}	0.300	1×10^1	$g_\sigma(\mathbf{x}) < 0$	
-2.45×10^{-6}	0.190	1×10^0	$g_\sigma(\mathbf{x}) < 0$	

Source: Author production.
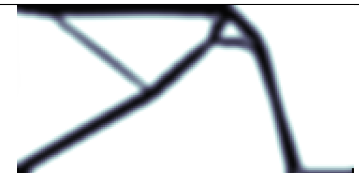
Table 11 – Valid topology optimization results for 400 Hz.
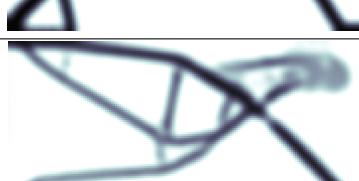
$f(\mathbf{x})[m^2]$	$\mathbf{x}_{initial}$	$\overline{v}_{final}$	r_f	Distribution of $\boldsymbol{\rho}$ in domain
-2.45×10^{-6}	$\mathbf{1}\overline{v}_{initial}$	0.190	1×10^0	
-2.43×10^{-6}	$\mathbf{1}$	0.185	1×10^3	

Source: Author production.

To enhance the importance of the stress constraint, the employed strategy was to increase the initial penalization value $\mathbf{c}_{inicial}$. However, this action resulted in discontinuous structures when using the adaptive volume reduction.

Therefore, a variation in the initial optimization point $\mathbf{x}_{initial}$ became necessary. These two modifications generated a continuous structure that satisfied all constraints and is highlighted in Table 12 (fourth row).

Table 12 – Results of topology optimization for the 600 Hz frequency varying the initial design variables ($\mathbf{x}_{initial}$) and penalty vector ($\mathbf{c}_{initial}$).
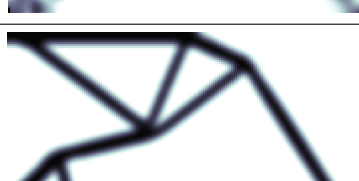
$f(\mathbf{x})[m^2]$	$\mathbf{x}_{initial}$	$\bar{v}_{final}$	$\mathbf{c}_{initial}$	$max(g_\sigma)$	Distribution of $\boldsymbol{\rho}$ in domain
-1.95×10^{-6}	$\mathbf{1}\bar{v}_{initial}$	0.150	$(1.0 \times 10^1)\mathbf{1}$	1.71×10^0	
-8.24×10^{-6}	$\mathbf{1}$	0.150	$(1.0 \times 10^1)\mathbf{1}$	2.20×10^1	
-5.14×10^{-6}	$\mathbf{1}\bar{v}_{initial}$	0.150	$(5.0 \times 10^1)\mathbf{1}$	1.20×10^1	
-2.38×10^{-6}	$\mathbf{1}$	0.185	$(5.0 \times 10^1)\mathbf{1}$	$g_\sigma(\mathbf{x}) < 0$	
-7.45×10^{-6}	$\mathbf{1}\bar{v}_{initial}$	0.150	$(1.0 \times 10^2)\mathbf{1}$	5.87×10^0	

Source: Author production.

4.4 RELAXATION OF CONSTRAINTS

The previous results shown that the designs were far from the first resonance due to the fact that all the constraints were active. Thus, this section will present the results obtained from the relaxation of the constraints.

The first results section has already addressed the impact of the volume fraction on the formulation. Therefore, this section will focus on the input displacement and stress constraints.
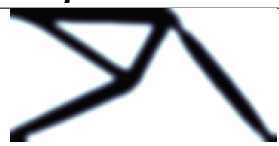
4.4.1 Relaxation of the input displacement constraint

This section aims to present the behavior of the formulation considering two conditions of input displacement constraint. The first is the standard constraint used in previous cases, $|\bar{u}_{in}| = 2.0 \times 10^{-3}$ m, and the second is $|\bar{u}_{in}| = 5.0 \times 10^{-3}$ m. The remaining parameters used in this section are presented in Tables 1, 2, and 3. An excitation frequency of 200 Hz is used.

Table 13 presents some results obtained through topology optimization for the case with

the standard constraint and for the case with the relaxed constraint. Upon examining the final volume fraction values, it can be inferred that the case with the relaxed constraint maintained its stress constraint violated until reaching the minimum determined value for this magnitude ($\bar{v}_{min}$).
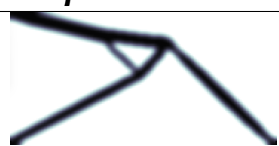
Table 13 – Results of the topology optimization for the excitation frequency of 200 Hz with the relaxation of input displacement constraint limits.

$f(\mathbf{x})$	$|u_{in}|$	$\bar{v}_{final}$	$max(g_\sigma)$	Distribution of $\boldsymbol{\rho}$ in domain
-2.67×10^{-6}	2.00×10^{-3}	0.24	$g_\sigma(\mathbf{x}) < 0$	
-1.07×10^{-5}	5.00×10^{-3}	0.15	6.39×10^{-1}	

Source: Author production.

An alternative for this situation could be to reduce the minimum volume fraction limit, $\bar{v}_{min}$, from 0.15 to 0.10. Through Table 14, it can be observed that this change in the volume limit was significant for reducing the violation of the stress constraint, but not sufficient for its satisfaction. In support of this assertion, Table 15 displays the distribution of stress constraints, illustrating how the third case exhibits a much more evenly distributed compliance than the others.
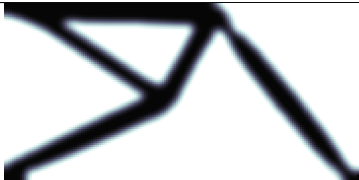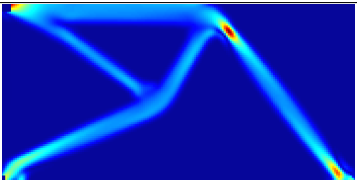
Table 14 – Results of the topological optimization for the excitation frequency of 200 Hz with the variation of the minimum limit volume fraction.

$f(\mathbf{x})$	$|u_{in}|$	$\bar{v}_{final}$	$max(g_\sigma)$	Distribution of $\boldsymbol{\rho}$ in domain
-1.07×10^{-5}	5.00×10^{-3}	0.15	6.39×10^{-1}	
-7.06×10^{-6}	5.00×10^{-3}	0.10	9.74×10^{-2}	

Source: Author production.

The value of the objective function is typically a crucial aspect of analysis; however, this can be a biased result since the objective function presented in Equation (98) is composed of the multiplication of input displacement by output displacement. Therefore, increasing the input displacement constraint is expected to increase the objective function. A more objective metric is the evaluation of this value across frequencies to observe the relationship between the excitation frequency and the natural frequency of the mechanism.

Table 15 – Results of the topology optimization for the excitation frequency of 200 Hz with the variation of the minimum limit volume fraction and input displacement constraint limits.
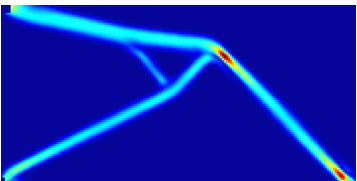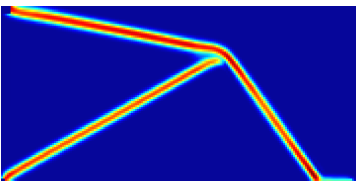
| $\|u_{in}\|$	$\bar{v}_{final}$	Distribution of $\boldsymbol{\rho}$ in domain	Distribution of element stress constraint
2.00×10^{-3}	0.24		
5.00×10^{-3}	0.15		
5.00×10^{-3}	0.10		

Source: Author production.

Figure 18 illustrates the objective function value of the mechanisms presented in Table 13 that have variations in the input displacement constraint. As shown in Table 13, the mechanisms with relaxed constraints do not represent valid mechanisms as their stress constraint is violated. Figure 18 displays the objective function curves and the values of the first natural frequency of the mechanism. Additionally, the deformed image of the first mode is presented, which in both cases presents inversion.

Figure 19 depicts the behavior of the mechanism presented in the last row of Table 14. Similar to the second mechanism, this one also continued to violate the stress constraint. Through a comparison among the three mechanisms, the third one exhibits the most evenly distributed compliance. However, this distribution did not result in an improvement in the objective function. In this case, however, the violation is present in a significant portion of its elements, as indicated in Table 15. This distributed compliance alters the vibration modes. In Figure 19, the first two vibration modes are local modes which, despite being closer to the excitation frequency, do not represent an increase in the objective function. The third vibration mode (998 Hz) corresponds to the motion reversal mode and thus, embodies the highest amplitude of the objective function.

4.4.2 Relaxation of the stress constraint

As observed in Table 15, the stress constraint is a crucial measure in determining the feasibility of a structure, rendering the two mechanisms obtained with relaxed input displacement constraint unfeasible. The analysis of stress constraint relaxation is presented in Table 16 and

Figure 18 – Displacements obtained through harmonic analysis for the mechanisms obtained with an excitation frequency of 200 Hz with the relaxation of the input displacement constraint limits.
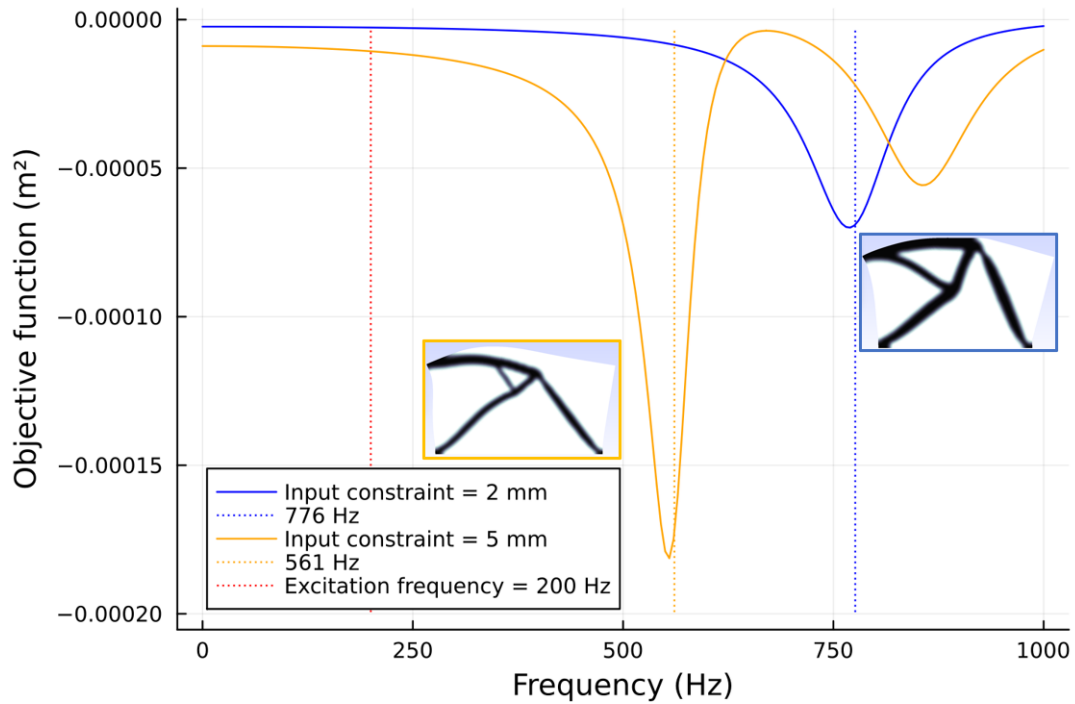
Source: Author production.

Figure 19 – Displacements obtained through a harmonic analysis for the mechanisms obtained with an excitation frequency of 200 Hz with a 2 mm input displacement constraint $|\bar{u}_{in}|$ and a 0.10 limit on volume fraction $\bar{v}_{min}$.
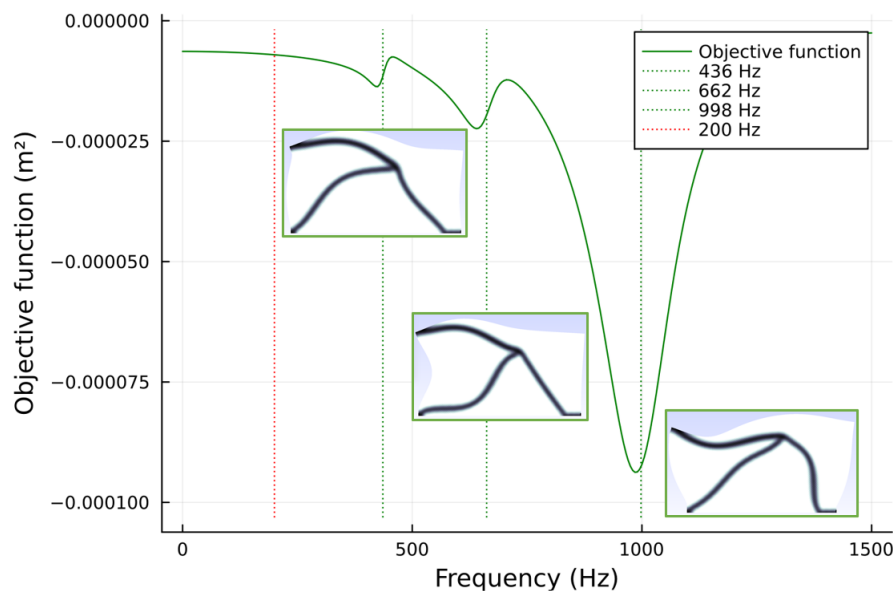
Source: Author production.

was conducted using the same frequency and parameters as in the previous subsection. It can be noted that this relaxation in the stress constraint rendered the reduction of volume fraction unnecessary, and consequently, the compliance remained more concentrated at the hinges. Unlike

the previous results, these mechanisms have all their constraints satisfied and active.

Table 16 – Results of the topology optimization for the excitation frequency of 200 Hz with the variation of stress constraint limit.
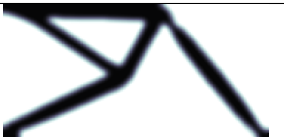
Iteration (k)	$f(\mathbf{x})$ [m^2]	$|u_{in}|$[m]	$\bar{v}_{final}$	$\overline{\sigma}$ [MPa]	Distribution of $\boldsymbol{\rho}$ in domain
33	-2.67×10^{-6}	2.0×10^{-3}	0.24	40.0	
16	-2.87×10^{-6}	2.0×10^{-3}	0.30	60.0	

Source: Author production.

As depicted in the algorithm flowchart (Figure 12 and Eq. (104)), the constraint serves as a stopping criterion for the optimization. Thus, upon observing Table 16, it is evident that the number of iterations required for optimization with the relaxation of the stress constraint is reduced.

Table 17 presents three viable mechanisms, each satisfying design constraints, derived from variations in input displacement and stress constraints. Figure 20 illustrates the behavior of these mechanisms through the objective function across a frequency range. It is evident that the relaxation of constraints allowed for the approximation between the first natural vibration frequencies and the excitation frequency. In essence, when allowed by their constraints, the mechanisms are optimized for configurations nearer to their resonance.

Table 17 – Results of the topological optimization for the excitation frequency of 200 Hz with the variation of stress constraint limit.

Condition	$f(\mathbf{x})$ [m^2]	$|u_{in}|$[m]	$\bar{v}_{final}$	$\overline{\sigma}$ [MPa]	Distribution of $\boldsymbol{\rho}$ in domain
A	-2.67×10^{-6}	2.0×10^{-3}	0.24	40.0	
B	-2.87×10^{-6}	2.0×10^{-3}	0.30	60.0	
C	-1.15×10^{-5}	5.0×10^{-3}	0.190	60.0	

Source: Author production.

Figure 20 – Displacements obtained through a harmonic analysis for the mechanisms obtained with an excitation frequency of 200 Hz with the variation of the input displacement and stress constraint limits.
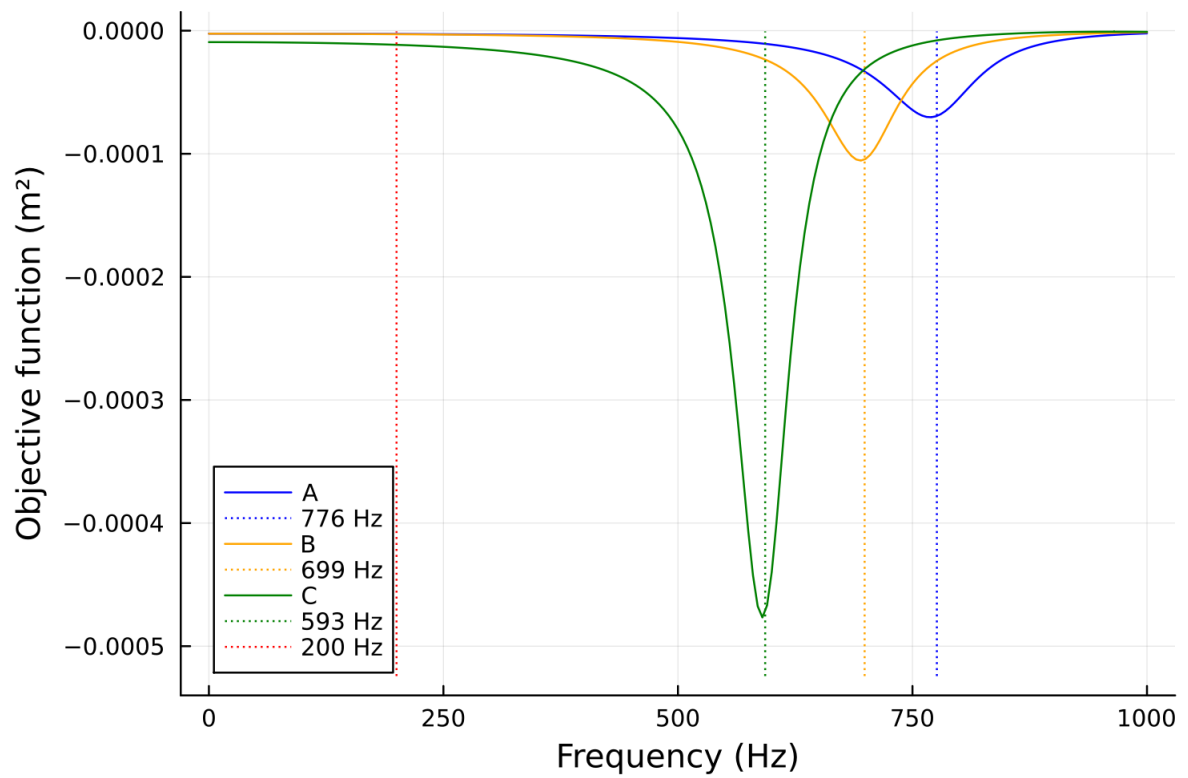
Source: Author production.

5 CONCLUSION

The purpose of this study is to present a formulation aimed at designing a compliant mechanism under harmonic regime, operating at low frequencies. This formulation is subject to constraints on input displacement, volume and local stresses. The constraints on input displacement and volume are integrated into the formulation through the Globally Convergent Method of Method of Moving Assymptotes (GCMMA), while the stress constraint is incorporated through the Augmented Lagrangian (AL) function. The AL function is a tool used to facilitate the inclusion of a large number of local stress constraints.

The objective function employed in this formulation is based on the time-averaged value to relate the real and imaginary parts of input and output displacements. Developed to meet the specificity of an inverter mechanism design, this function, along with the input displacement constraint, achieves its purpose by incorporating information regarding the output displacement amplitude and the relative phase between input and output displacements into the formulation.

An adaptability approach of the volume fraction limit is incorporated, linked to the stress constraint. This approach has proven effective, designing mechanisms that satisfy the stress constraints by utilizing a smaller portion of the available volume within the domain. The results indicate that, under the analyzed conditions, the violation of the stress constraint was associated with the concentration of compliance, particularly in regions of material narrowing (hinges). Thus, the reduction in the volume fraction contributed to enhancing the distribution of compliance throughout the domain, thereby satisfying the stress constraints.

Results are presented for the formulation over a frequency range from 0 to 600 Hz, all satisfying constraints, minimizing the objective function and demonstrating a motion inversion behavior. Some mechanisms required adjustments in the parameters: objective function adjustment factor (r_f), AL initial penalty vector ($\mathbf{c}_{initial}$) and vector of initial design variables ($\mathbf{x}_{initial}$). This need for adjustments represents an opportunity for refinement of the formulation, as these parameters, when employed in topology optimization methods, necessitate careful adjustments with physical significance.

Overall, the evaluation of the formulation across the excitation frequencies proved satisfactory for the only test case analyzed in this work, the inverter mechanism. However, it did not result in the outcome of resonant structures that would have further maximized the output displacement. This can be attributed to the constraints which are active in the optimized solutions.

The impact of relaxing the constraints on input displacement and stress was analyzed and validated. The relaxation of the upper limits of these two measures facilitated the maximization of the output displacement and, furthermore, the approximation of the natural vibration frequency to the excitation frequency used in the formulation.

5.1   FUTURE WORK

The following items have been identified as potential areas for improvement in future work:

- Study other examples of flexible mechanisms;

- Developing an adjustable model for the parameters r_f and $\mathbf{x}_{initial}$, thereby achieving a formulation less sensitive to the input parameters;

- Improving the computational code to reduce the cost associated with each analysis;

- Study of this formulation applied to frequencies above the first natural frequency, referred to as "high frequencies";

- Study algorithms to enforce material continuity, specially in higher frequencies.

BIBLIOGRAPHY

AL-BAZOON, M.; ARORA, J. S. Discrete variable optimization of structures subjected to dynamic loads using equivalent static loads and metaheuristic algorithms. **Optimization and Engineering**, v. 64, p. 643–687, 2022.

ANANTHASURESH, G.K.; KOTA, S.; GIANCHANDANI, Y. A Methodical Approach To the Design of Compliant Micromechanisms. **Solid-State Sensors, Actuators, and Microsystems Workshop**, p. 189–192, 1994.

ARORA, J. S. **Optimization of structural and mechanical systems.** [S.l.]: World Scientific, 2007.

BATHE, Klaus-Jurgen. **Finite Element Procedures**. [S.l.]: Prentice Hall, 1996.

BENDSØE, Martin Philip; KIKUCHI, Noboru. Generating optimal topologies in structural design using a homogenization method. **Computer Methods in Applied Mechanics and Engineering**, v. 71, n. 2, p. 197–224, 1988. ISSN 00457825.

BENDSØE, M. P.; SIGMUND, O. Material interpolation schemes in topology optimization. **Archive of Applied Mechanics**, v. 69, n. 9-10, p. 635–654, 1999. ISSN 09391533.

BEZANSON, Jeff et al. Julia: A fresh approach to numerical computing. **SIAM Review**, SIAM, v. 59, n. 1, p. 65–98, 2017. Disponível em: <https://epubs.siam.org/doi/10.1137/141000671>.

BIRGIN, E. G.; MARTÍNEZ, J. M. **Practical Augmented Lagrangian Methods for Constrained Optimization**. [S.l.: s.n.], 2014. ISBN 9781611973358.

BRUGGI, Matteo. On an alternative approach to stress constraints relaxation in topology optimization. **Structural and Multidisciplinary Optimization**, v. 36, n. 2, p. 125–141, 2008. ISSN 1615147X.

CARDOSO, Eduardo Lenz. **CodeLenz/LFEM.jl**. [S.l.]: GitHub, 2023.

CARDOSO, Eduardo Lenz. **CodeLenz/LFilter.jl**. [S.l.]: GitHub, 2023.

CARDOSO, Eduardo Lenz; FONSECA, Jun Sérgio Ono Fonseca. Strain energy maximization approach to the design of fully compliant mechanisms using topology optimization. **Latin American Journal of Solids and Structures**, v. 1, p. 263–275, 2004. Disponível em: <www.lajss.org>.

CARDOSO, E. L; SILVA, G. A. da; BECK, A. T. Robust topology optimization of compliant mechanisms with uncertainties in output stiffness. **International Journal for Numerical Methods in Engineering**, v. 119, n. 6, p. 532–547, 2019. ISSN 10970207.

DEEPAK, Sangamesh R.; DINESH, M.; ANANTHASURESH, G. K. A comparative study of the formulations for topology optimization of compliant mechanisms. **Proceedings of the ASME 2009 Design Engineering Technical Conference & Computers and Information in Engineering Conference IDETC/CIE 2008**, v. 1, 2008. ISSN 19424302.

DING, Senmao et al. Isogeometric topology optimization of compliant mechanisms using transformable triangular mesh (TTM) algorithm. **Structural and Multidisciplinary Optimization**, Structural and Multidisciplinary Optimization, v. 64, n. 4, p. 2553–2576, 2021. ISSN 16151488.

DUYSINX, P.; BENDSøE, M. P. Topology optimization of continuum structures with local stress constraints. **International Journal for Numerical Methods in Engineering**, v. 43, n. 8, p. 1453–1478, 1998.

FRECKER, M I et al. Topological Synthesis of Compliant Mechanisms Using Multi-Criteria Optimization. **ASME**, v. 119, n. June 1997, p. 238–245, 1997.

GALLEGO, Juan A; HERDER, Just. Synthesis methods in compliant mechanisms: an overview. **Proceedings of the ASME 2009 Design Engineering Technical Conference & Computers and Information in Engineering Conference IDETC/CIE 2009**, v. 2, n. 86845, 2009.

GEUZAINE, Christophe; REMACLE, Jean-Francois. **Gmsh**. 2020. Disponível em: <http://http://gmsh.info/>.

GIRALDO-LONDOÑO, Oliver; AGUILÓ, Miguel A.; PAULINO, Glaucio H. Local stress constraints in topology optimization of structures subjected to arbitrary dynamic loads: a stress aggregation-free approach. **Structural and Multidisciplinary Optimization**, v. 64, n. 6, p. 3287–3309, 2021. ISSN 16151488.

GOMES-RUGGIERO, Márcia A.; SACHINE, Mael; SANTOS, Sandra A. Solving the dual subproblem of the method of moving asymptotes using a trust-region scheme. **Computational and Applied Mathematics**, v. 30, n. 1, p. 151–170, 2011. ISSN 18070302.

GUO, X.; CHENG, G. D. S-relaxed approach in structural topology optimization. **Structural Optimization**, n. 1972, p. 258–266, 1997.

HER, I.; MIDHA, A. A compliance number concept for compliant mechanisms, and type synthesis. **Journal of Mechanical Design, Transactions of the Automation in Design.**, v. 109, p. 348–355, 1987. ISSN 10500472.

HETRICK, Joel A.; KOTA, Sridhar. An energy formulation for parametric size and shape optimization of compliant mechanisms. **Journal of Mechanical Design**, v. 121, n. June 1999, p. 229–234, 1999.

HOWELL, Larry L. **Compliant Mechanisms**. [S.l.]: A Wiley-Interscience Puclication, 2001. 1 p.

HOWELL, L. L.; MIDHA, A. A method for the design of compliant mechanisms with small-length flexural pivots. **Journal of Mechanical Design**, v. 116, n. 1, p. 280–290, 1994. ISSN 10500472.

JOHNSON, Steven G. **The NLopt nonlinear-optimization package**. 2007. <https://github.com/stevengj/nlopt>.

JUNG, Ui-Jin; PARK, Gyung-Jin. A new method for simultaneous optimum design of structural and control systems. **Computers & Structures**, Elsevier BV, v. 160, p. 90–99, nov. 2015.

JUNIOR, Hélio Emmendoerfer; FANCELLO, Eduardo; SILVA, Emilio. Stress-constrained level set topology optimization for compliant mechanisms. **Computer Methods in Applied Mechanics and Engineering**, v. 362, 04 2020.

KANG, Byung-Soo; CHOI, Woo-Seok; PARK, Gyung-Jin. Structural optimization under equivalent static loads transformed from dynamic loads based on displacement. **Computers & Structures**, Elsevier BV, v. 79, n. 2, p. 145–154, jan. 2001.

KIRSCH, U. Optimal topologies of truss structures. **Computer Methods in Applied Mechanics and Engineering**, v. 72, n. 1, p. 15–28, 1989. ISSN 00457825.

LARSEN, Ulrik Darling; SIGMUND, Ole; BOUWSTRA, Siebe. Design and fabrication of compliant micromechanisms and structures with negative Poisson's ratio. **I E E E Journal of Microelectromechanical Systems**, v. 6, n. 2, p. 99–106, 1997. ISSN 10577157.

LARSEN, Ulrik Darling; SIGMUND, Ole; BOUWSTRA, Siebe. On the design of compliant mechanisms using topology optimization. **Mechanics of Structures and Machines**, v. 25, n. 4, p. 493–524, 1997. ISSN 08905452.

LE, Chau et al. Stress-based topology optimization for continua. **Structural and Multidisciplinary Optimization**, v. 41, n. 4, p. 605–620, Apr 2010. ISSN 1615-1488.

LEE, Hyun-Ah; PARK, Gyung-Jin. Nonlinear dynamic response topology optimization using the equivalent static loads method. **Computer Methods in Applied Mechanics and Engineering**, Elsevier BV, v. 283, p. 956–970, jan. 2015.

LIANG, Yuang; SUN, Kai; CHENG, Geng Dong. Discrete variable topology optimization for compliant mechanism design via Sequential Approximate Integer Programming with Trust Region (SAIP-TR). **Structural and Multidisciplinary Optimization**, Structural and Multidisciplinary Optimization, v. 62, n. 6, p. 2851–2879, 2020. ISSN 16151488.

MA, Z. D.; KIKUCHI, N.; HAGIWARA, I. Structural topology and shape optimization for a frequency response problem. **Computational Mechanics**, v. 13, n. 3, p. 157–174, 1993. ISSN 01787675.

MARSDEN, Jerrold E.; HUGHES, Thomas J.R. **Mathematical Foundations of Elasticity**. [S.l.]: Dover Publications, INC, 1994.

MIN, S. et al. Optimal topology design of structures under dynamic loads. **Structural Optimization**, v. 17, n. 2, p. 208–218, 1999. ISSN 09344373.

MIYAJIMA, Ken; NOGUCHI, Yuki; YAMADA, Takayuki. Optimal design of compliant displacement magnification mechanisms using stress-constrained topology optimization based on effective energy. Elsevier B.V., jul 2022.

MONTERO, Diego Schmitt. **Topology optimization of continuum structures subjected to harmonic loads with local stress constraints**. 2019.

MONTERO, Diego Schmitt; SILVA, Olavo M.; CARDOSO, Eduardo Lenz. Topology optimization for harmonic vibration problems using a density-weighted norm objective function. **Structural and Multidisciplinary Optimization**, Springer Science and Business Media Deutschland GmbH, v. 62, n. 6, p. 3301–3327, dec 2020. ISSN 16151488.

MURPHY, Morgan D.; MIDHA, A.; HOWELL, Larry L. The topological synthesis of compliant mechanisms. **Elsevier Science Ltd**, v. 31, n. 2, p. 185–199, 1996.

NEVES, M M; RODRIGUES, H; GUEDES, M. Technical Papers Generalized topology criterion design of structures with a buckling load. **Structural Optimization**, v. 10, p. 71–78, 1995.

NISHIWAKI, Shinji et al. Topology optimization of compliant mechanisms using the homogenization method. **International Journal for Numerical Methods in Engineering**, v. 42, n. 3, p. 535–559, 1998. ISSN 00295981.

OLHOFF, Niels; DU, Jianbin. On topological design optimization of structures against vibration and noise emission. **CISM International Centre for Mechanical Sciences, Courses and Lectures**, v. 505, n. 1988, p. 217–276, 2009. ISSN 23093706.

PARK, Gyung-Jin. Technical overview of the equivalent static loads method for non-linear static response structural optimization. **Structural and Multidisciplinary Optimization**, Springer Science and Business Media LLC, v. 43, n. 3, p. 319–337, jul. 2010.

PEREIRA, Alexandre; CARDOSO, Eduardo Lenz. On the influence of local and global stress constraint and filtering radius on the design of hinge-free compliant mechanisms. **Structural and Multidisciplinary Optimization**, Structural and Multidisciplinary Optimization, v. 58, n. 2, p. 641–655, 2018. ISSN 16151488.

PEREIRA, ALEXANDRE DE ASSIS. **On the Influence of Stress Constraint and Filtering Hinge-Free Compliant Mechanisms**. 2017.

RACKAUCKAS, Christopher. **LinearSolve.jl: because A̲is not good enough**. figshare, 2022. Disponível em: <https://figshare.com/articles/presentation/LinearSolve_jl_because_A_b_is_not_good_enough/20380809/1>.

RODRIGUEZ, Thibaut et al. Structural Displacement Requirement in a Topology Optimization Algorithm Based on Isogeometric Entities. **Journal of Optimization Theory and Applications**, Springer US, v. 184, n. 1, p. 250–276, 2020. ISSN 15732878.

SELTMANN, Stephanie; HASSE, Alexander. Topology optimization of compliant mechanisms with distributed compliance (hinge-free compliant mechanisms) by using stiffness and adaptive volume constraints instead of stress constraints. **Mechanism and Machine Theory**, Elsevier Ltd, v. 180, n. October 2022, p. 105133, 2023. ISSN 0094114X.

SENNE, Thadeu A.; GOMES, Francisco A.M.; SANTOS, Sandra A. Inexact Newton method with iterative combined approximations in the topology optimization of geometrically nonlinear elastic structures and compliant mechanisms. **Optimization and Engineering**, Springer US, n. 0123456789, 2022. ISSN 15732924.

SHU, Lei et al. Level set based structural topology optimization for minimizing frequency response. **Journal of Sound and Vibration**, Elsevier, v. 330, n. 24, p. 5820–5834, 2011. ISSN 0022460X.

SIGMUND, Ole. Morphology-based black and white filters for topology optimization. **Structural and Multidisciplinary Optimization**, v. 33, n. 4-5, p. 401–424, 2007. ISSN 1615147X.

SIGMUND, Ole. Manufacturing tolerant topology optimization. **Acta Mechanica Sinica/Lixue Xuebao**, v. 25, n. 2, p. 227–239, 2009. ISSN 05677718.

SILVA, Olavo M. **Otimização Topológica em Problemas de Vibrações Harmônicas Utilizando Potência de Entrada**. Tese (Ph.D Thesis) — Universidade Federal de Santa Catarina, 2017.

SILVA, Olavo M.; NEVES, Miguel M.; LENZI, Arcanjo. A critical analysis of using the dynamic compliance as objective function in topology optimization of one-material structures considering steady-state forced vibration problems. **Journal**

of Sound and Vibration, v. 444, p. 1–20, 2019. ISSN 0022-460X. Disponível em: <https://www.sciencedirect.com/science/article/pii/S0022460X18308563>.

STANKIEWICZ, Gabriel; DEV, Chaitanya; STEINMANN, Paul. Geometrically nonlinear design of compliant mechanisms: Topology and shape optimization with stress and curvature constraints. **Computer Methods in Applied Mechanics and Engineering**, Elsevier B.V., v. 397, p. 115161, 2022. ISSN 00457825.

SURHONE, L.M.; TIMPLEDON, M.T.; MARSEKEN, S.F. **Von Mises Yield Criterion**. [S.l.]: VDM Publishing, 2010. ISBN 9786131129438.

SVANBERG, K. The method of moving asymptotes - a new method for structural optimization. **International Journal for Numerical Methods in Engineering.**, v. 24, n. October 1985, p. 359–373, 1987.

SVANBERG, Krister. A class of globally convergent optimization methods based on conservative convex separable approximations. **SIAM Journal on Optimization**, v. 12, n. 2, p. 555–573, 2002.

TCHERNIAK, Dmitri. Topology optimization of resonating structures using SIMP method. **International Journal for Numerical Methods in Engineering**, v. 54, n. 11, p. 1605–1622, 2002. ISSN 00295981.

VALENTINI, Fernando; SILVA, Olavo M.; CARDOSO, Eduardo Lenz. Robust topology optimization for harmonic displacement minimization of structures subjected to uncertainty in the excitation frequency. **Computer Methods in Applied Mechanics and Engineering**, v. 379, p. 113767, 2021. ISSN 0045-7825.

VENINI, Paolo. Dynamic compliance optimization: Time vs frequency domain strategies. **Computers & Structures**, Elsevier BV, v. 177, p. 12–22, dez. 2016.

WANG, Fengwen; LAZAROV, Boyan Stefanov; SIGMUND, Ole. On projection methods, convergence and robust formulations in topology optimization. **Structural and Multidisciplinary Optimization**, v. 43, n. 6, p. 767–784, 2011. ISSN 16151488.

YANG, Xiongwei; LI, Yueming. Topology optimization to minimize the dynamic compliance of a bi-material plate in a thermal environment. **Structural and Multidisciplinary Optimization**, Springer Science and Business Media LLC, v. 47, n. 3, p. 399–408, aug 2012.

YANG, Xiongwei; LI, Yueming. Structural topology optimization on dynamic compliance at resonance frequency in thermal environments. **Structural and Multidisciplinary Optimization**, Springer Science and Business Media LLC, v. 49, n. 1, p. 81–91, jul 2013.

ZHAN, Junjie; LUO, Yangjun. Robust topology optimization of hinge-free compliant mechanisms with material uncertainties based on a non-probabilistic field model. **Frontiers of Mechanical Engineering**, v. 14, n. 2, p. 201–212, 2019. ISSN 20950241.

ZHANG, Weisheng; ZHONG, Wenliang; GUO, Xu. An explicit length scale control approach in SIMP-based topology optimization. **Computer Methods in Applied Mechanics and Engineering**, Elsevier B.V., v. 282, p. 71–86, 2014. ISSN 00457825.

ZHANG, Xiaopeng; KANG, Zhan; ZHANG, Wenbo. Robust topology optimization for dynamic compliance minimization under uncertain harmonic excitations with inhomogeneous eigenvalue analysis. **Structural and Multidisciplinary Optimization**, Structural and Multidisciplinary Optimization, v. 54, n. 6, p. 1469–1484, 2016. ISSN 16151488.

ZHAO, D.; WANG, H. Topology Optimization of Compliant Mechanisms Considering Manufacturing Uncertainty, Fatigue, and Static Failure Constraints. **Processes**, v. 11, n. 2914, p. 1–22, 2023. ISSN 16151488.

ZHU, Benliang et al. Design of compliant mechanisms using continuum topology optimization: A review. **Mechanism and Machine Theory**, Elsevier Ltd, v. 143, 2020. ISSN 0094114X.

ZHU, Mu et al. Topology optimization for linear stationary stochastic dynamics. **Structural Safety**, Elsevier BV, v. 67, p. 116–131, jul. 2017.

APPENDIX A – PHASE CONSTRAINT

Starting from Eq. (77), the value of the output displacement can be represented by its magnitude, which is given by its absolute value. However, applying the absolute value to the output displacement would eliminate the directional information from the movement. If this option is chosen, to align with an inverter mechanism, it becomes necessary to include a constraint that carries the directional information for the formulation

$$
\begin{cases}
\min \quad -|u_{out}(\mathbf{x})|, \\
S.t. \\
\quad \mathbf{K_D}(\mathbf{x})\mathbf{U}(\mathbf{x}) = \mathbf{F}(\mathbf{x}) \\
\quad g_{in}(\mathbf{x}) \leq 0 \\
\quad g_v(\mathbf{x}) \leq 0 \\
\quad g_{\sigma_{e,k}}(\mathbf{x}) \leq 0 \\
\quad g_\phi(\mathbf{x}) \leq 0 \\
\quad \underline{\mathbf{x}} \leq \mathbf{x} \leq \bar{\mathbf{x}}
\end{cases}
\tag{144}
$$

where

$$
g_\phi(\mathbf{x}) = \frac{\cos\phi(\mathbf{x}) - \bar{c}_\phi}{|\bar{c}_\phi|}
\tag{145}
$$

is the proposed phase constraint. The (cosine of the) phase angle ϕ between the input and the output displacements is given by the definition of the inner product

$$
\langle u_{in}, u_{out} \rangle = \cos(\phi)|u_{in}||u_{out}|
\tag{146}
$$

such that

$$
\cos\phi = \frac{u_{out_R}u_{in_R} + u_{out_I}u_{in_I}}{|u_{out}||u_{in}|},
\tag{147}
$$

and $\bar{c}_\phi$ is the cosine of the limit angle for the phase constraint.

Although the definition given in Eq. (146) gives ϕ in the continuous range $[0, 2\pi)$ the input and the output displacements in Fig. 8 are co-linear. This fact makes this measure discontinuous since both vectors can only be either in the same direction ($\cos\phi = 1$) or in the opposite directions ($\cos\phi = -1$).

APPENDIX B – DEFINITION OF THE AJOINT PROBLEM

Let $\Phi(\mathbf{U}(\rho), \rho)$ be a function

$$\Phi(\mathbf{U}(\rho), \rho) = \mathscr{L}(\mathbf{U}(\rho), \rho) + \frac{\boldsymbol{\lambda}_1^T}{2}(\mathbf{K}_D(\rho)\mathbf{U}(\rho) - \mathbf{F}(\rho)) + \frac{\boldsymbol{\lambda}_2^T}{2}(\mathbf{K}_D^*(\rho)\mathbf{U}^*(\rho) - \mathbf{F}^*(\rho)). \quad (148)$$

Assuming that $\mathbf{K}_D$ does not depend on $\mathbf{U}$ and $\mathbf{U}$ is a vector of complex numbers,

$$\mathbf{U} = \mathbf{U}_R + i\mathbf{U}_I, \quad (149)$$

the derivative of Φ with respect to ρ_m is given by

$$\frac{d\Phi}{d\rho_m} = \frac{\partial \mathscr{L}}{\partial \rho_m} + \frac{\partial \mathscr{L}}{\partial \mathbf{U}_R}^T \frac{d\mathbf{U}_R}{d\rho_m} + \frac{\partial \mathscr{L}}{\partial \mathbf{U}_I}^T \frac{d\mathbf{U}_I}{d\rho_m} +$$
$$\frac{\boldsymbol{\lambda}_1^T}{2}\left(\frac{d\mathbf{K}_D}{d\rho_m}\mathbf{U}_R + i\frac{d\mathbf{K}_D}{d\rho_m}\mathbf{U}_I + \mathbf{K}_D\frac{d\mathbf{U}_R}{d\rho_m} + i\mathbf{K}_D\frac{d\mathbf{U}_I}{d\rho_m} - \frac{d\mathbf{F}}{d\rho_m}\right) +$$
$$\frac{\boldsymbol{\lambda}_2^T}{2}\left(\frac{d\mathbf{K}_D^*}{d\rho_m}\mathbf{U}_R - i\frac{d\mathbf{K}_D^*}{d\rho_m}\mathbf{U}_I + \mathbf{K}_D^*\frac{d\mathbf{U}_R}{d\rho_m} - i\mathbf{K}_D^*\frac{d\mathbf{U}_I}{d\rho_m} - \frac{d\mathbf{F}^*}{d\rho_m}\right). \quad (150)$$

Grouping by common terms

$$\frac{d\Phi}{d\rho_m} = \frac{\partial \mathscr{L}}{\partial \rho_m} + \left[\frac{\partial \mathscr{L}}{\partial \mathbf{U}_R}^T + \frac{\boldsymbol{\lambda}_1^T}{2}\mathbf{K}_D + \frac{\boldsymbol{\lambda}_2^T}{2}\mathbf{K}_D^*\right]\frac{d\mathbf{U}_R}{d\rho_m} +$$
$$\left[\frac{\partial \mathscr{L}}{\partial \mathbf{U}_I}^T + i\frac{\boldsymbol{\lambda}_1^T}{2}\mathbf{K}_D - i\frac{\boldsymbol{\lambda}_2^T}{2}\mathbf{K}_D^*\right]\frac{d\mathbf{U}_I}{d\rho_m} + \frac{\boldsymbol{\lambda}_1^T}{2}\left(\frac{d\mathbf{K}_D}{d\rho_m}\mathbf{U}_R + i\frac{d\mathbf{K}_D}{d\rho_m}\mathbf{U}_I - \frac{d\mathbf{F}}{d\rho_m}\right) +$$
$$\frac{\boldsymbol{\lambda}_2^T}{2}\left(\frac{d\mathbf{K}_D^*}{d\rho_m}\mathbf{U}_R - i\frac{d\mathbf{K}_D^*}{d\rho_m}\mathbf{U}_I - \frac{d\mathbf{F}^*}{d\rho_m}\right). \quad (151)$$

The main advantage of using the adjoint problem is to avoid computing the derivative of $\frac{d\mathbf{U}}{d\rho_m}$ at each iteration, which would significantly increase computational cost. Thus, we set the terms multiplying the derivatives of $\frac{d\mathbf{U}_R}{d\rho_m}$ and $\frac{d\mathbf{U}_I}{d\rho_m}$ to zero, resulting in two coupled adjoint problems

$$\frac{\partial \mathscr{L}}{\partial \mathbf{U}_R}^T + \frac{\boldsymbol{\lambda}_1^T}{2}\mathbf{K}_D + \frac{\boldsymbol{\lambda}_2^T}{2}\mathbf{K}_D^* = \mathbf{0}^T,$$
$$\frac{\partial \mathscr{L}}{\partial \mathbf{U}_I}^T + i\frac{\boldsymbol{\lambda}_1^T}{2}\mathbf{K}_D - i\frac{\boldsymbol{\lambda}_2^T}{2}\mathbf{K}_D^* = \mathbf{0}^T. \quad (152)$$

Isolating $\frac{1}{2}\boldsymbol{\lambda}_1^T\mathbf{K}_D$ in the first line

$$\frac{1}{2}\boldsymbol{\lambda}_1^T\mathbf{K}_D = -\frac{\partial \mathscr{L}}{\partial \mathbf{U}_R}^T - \frac{1}{2}\boldsymbol{\lambda}_2^T\mathbf{K}_D^* \quad (153)$$

and substituting in the second equation

$$i\left(-\frac{\partial \mathscr{L}^T}{\partial \mathbf{U}_R} - \frac{1}{2}\boldsymbol{\lambda}_2^T \mathbf{K}_D^*\right) - i\frac{1}{2}\boldsymbol{\lambda}_2^T \mathbf{K}_D^* = -\frac{\partial \mathscr{L}^T}{\partial \mathbf{U}_I} \ . \tag{154}$$

Multiplying by i

$$i^2\left(-\frac{\partial \mathscr{L}^T}{\partial \mathbf{U}_R} - \frac{1}{2}\boldsymbol{\lambda}_2^T \mathbf{K}_D^*\right) - i^2\frac{1}{2}\boldsymbol{\lambda}_2^T \mathbf{K}_D^* = -i\frac{\partial \mathscr{L}^T}{\partial \mathbf{U}_I} \tag{155}$$

rearranging we have

$$\boldsymbol{\lambda}_2^T \mathbf{K}_D^* = -i\frac{\partial \mathscr{L}^T}{\partial \mathbf{U}_I} - \frac{\partial \mathscr{L}^T}{\partial \mathbf{U}_R} \ . \tag{156}$$

Substituting this expression into Eq. 153

$$\frac{1}{2}\boldsymbol{\lambda}_1^T \mathbf{K}_D = -\frac{\partial \mathscr{L}^T}{\partial \mathbf{U}_R} - \frac{1}{2}\left(-i\frac{\partial \mathscr{L}^T}{\partial \mathbf{U}_I} - \frac{\partial \mathscr{L}^T}{\partial \mathbf{U}_R}\right) \tag{157}$$

such that

$$\boldsymbol{\lambda}_1^T \mathbf{K}_D = i\frac{\partial \mathscr{L}^T}{\partial \mathbf{U}_I} - \frac{\partial \mathscr{L}^T}{\partial \mathbf{U}_R} \ . \tag{158}$$

Using the fact that $\mathbf{K}_D$ is Hermitian (conjugate transpose is equal to the matrix itself) and comparing Eqs. (156) and (153)

$$\mathbf{K}_D \boldsymbol{\lambda}_1 = -\mathbf{A}^* \tag{159}$$

and

$$\mathbf{K}_D^* \boldsymbol{\lambda}_2 = -\mathbf{A}. \tag{160}$$

Thus, solving each of the equations we obtain

$$\boldsymbol{\lambda}_1 = -\mathbf{K}_D^{-1}\mathbf{A}^* \tag{161}$$

and

$$\boldsymbol{\lambda}_2 = -\mathbf{K}_D^H \mathbf{A} \tag{162}$$

which shows us that $\boldsymbol{\lambda}_1$ and $\boldsymbol{\lambda}_2$ are conjugates. Another way to show would be isolating $\mathbf{A}^*$ in the first equation

$$\mathbf{A}^* = -\mathbf{K}_D \boldsymbol{\lambda}_1 \tag{163}$$

such that, applying the adjoint operator on both sides

$$(\mathbf{A}^*)^* = \mathbf{A} = -\mathbf{K}_D^* \boldsymbol{\lambda}_1^* \tag{164}$$

and if we insert this expression into the second equation

$$\boldsymbol{\lambda}_2 = \mathbf{K}_D^H \mathbf{K}_D^* \boldsymbol{\lambda}_1^* = \mathbf{I} \boldsymbol{\lambda}_1^*. \tag{165}$$

In this way, we can only solve the following expression

$$\mathbf{K}_D \boldsymbol{\lambda}_1 = i\frac{\partial \mathscr{L}}{\partial \mathbf{U}_I} - \frac{\partial \mathscr{L}}{\partial \mathbf{U}_R}. \tag{166}$$

Returning to the Eq. (167)

$$\frac{d\Phi}{d\rho_m} = \frac{\partial \mathscr{L}}{\partial \rho_m} + \frac{\boldsymbol{\lambda}_1^T}{2}\left(\frac{d\mathbf{K}_D}{d\rho_m}\mathbf{U}_R + i\frac{d\mathbf{K}_D}{d\rho_m}\mathbf{U}_I - \frac{d\mathbf{F}}{d\rho_m}\right) + \frac{\boldsymbol{\lambda}_2^T}{2}\left(\frac{d\mathbf{K}_D^*}{d\rho_m}\mathbf{U}_R - i\frac{d\mathbf{K}_D^*}{d\rho_m}\mathbf{U}_I - \frac{d\mathbf{F}^*}{d\rho_m}\right). \tag{167}$$

It is interesting to expand all terms (except the partial derivative of $\mathscr{L}$ with respect to ρ_m, which is real) into their real and complex parts.

For the remaining terms (which depend on the adjoint) and using

$$\boldsymbol{\lambda}_1^T = \boldsymbol{\lambda}^T = \boldsymbol{\lambda}_R^T + i\boldsymbol{\lambda}_I^T, \tag{168}$$

$$\boldsymbol{\lambda}_2^T = (\boldsymbol{\lambda}_1^T)^* = \boldsymbol{\lambda}_R^T - i\boldsymbol{\lambda}_I^T, \tag{169}$$

we have

$$\begin{aligned}
\frac{1}{2}\Bigg(& \boldsymbol{\lambda}_R^T \frac{d\mathbf{K}_{D_R}}{d\rho_m}\mathbf{U}_R + i\boldsymbol{\lambda}_R^T \frac{d\mathbf{K}_{D_I}}{d\rho_m}\mathbf{U}_R + i\boldsymbol{\lambda}_I^T \frac{d\mathbf{K}_{D_R}}{d\rho_m}\mathbf{U}_R - \boldsymbol{\lambda}_I^T \frac{d\mathbf{K}_{D_I}}{d\rho_m}\mathbf{U}_R + \\
& i\boldsymbol{\lambda}_R^T \frac{d\mathbf{K}_{D_R}}{d\rho_m}\mathbf{U}_I - \boldsymbol{\lambda}_R^T \frac{d\mathbf{K}_{D_I}}{d\rho_m}\mathbf{U}_I - \boldsymbol{\lambda}_I^T \frac{d\mathbf{K}_{D_R}}{d\rho_m}\mathbf{U}_I - i\boldsymbol{\lambda}_I^T \frac{d\mathbf{K}_{D_I}}{d\rho_m}\mathbf{U}_I - \\
& \boldsymbol{\lambda}_R^T \frac{d\mathbf{F}_R}{d\rho_m} - i\boldsymbol{\lambda}_R^T \frac{d\mathbf{F}_I}{d\rho_m} - i\boldsymbol{\lambda}_I^T \frac{d\mathbf{F}_R}{d\rho_m} + \boldsymbol{\lambda}_I^T \frac{d\mathbf{F}_I}{d\rho_m} + \\
& \boldsymbol{\lambda}_R^T \frac{d\mathbf{K}_{D_R}}{d\rho_m}\mathbf{U}_R - i\boldsymbol{\lambda}_R^T \frac{d\mathbf{K}_{D_I}}{d\rho_m}\mathbf{U}_R - i\boldsymbol{\lambda}_I^T \frac{d\mathbf{K}_{D_R}}{d\rho_m}\mathbf{U}_R - \boldsymbol{\lambda}_I^T \frac{d\mathbf{K}_{D_I}}{d\rho_m}\mathbf{U}_R - \\
& i\boldsymbol{\lambda}_R^T \frac{d\mathbf{K}_{D_R}}{d\rho_m}\mathbf{U}_I - \boldsymbol{\lambda}_R^T \frac{d\mathbf{K}_{D_I}}{d\rho_m}\mathbf{U}_I - \boldsymbol{\lambda}_I^T \frac{d\mathbf{K}_{D_R}}{d\rho_m}\mathbf{U}_I + \boldsymbol{\lambda}_I^T \frac{d\mathbf{K}_{D_I}}{d\rho_m}\mathbf{U}_I - \\
& \boldsymbol{\lambda}_R^T \frac{d\mathbf{F}_R}{d\rho_m} + i\boldsymbol{\lambda}_R^T \frac{d\mathbf{F}_I}{d\rho_m} + i\boldsymbol{\lambda}_I^T \frac{d\mathbf{F}_R}{d\rho_m} + \boldsymbol{\lambda}_I^T \frac{d\mathbf{F}_I}{d\rho_m}\Bigg),
\end{aligned} \tag{170}$$

$$\frac{1}{2}\left(\boldsymbol{\lambda}_R^T\frac{d\mathbf{K}_{D_R}}{d\rho_m}\mathbf{U}_R + i\boldsymbol{\lambda}_R^T\frac{d\mathbf{K}_{D_I}}{d\rho_m}\mathbf{U}_R + i\boldsymbol{\lambda}_I^T\frac{d\mathbf{K}_{D_R}}{d\rho_m}\mathbf{U}_R - \boldsymbol{\lambda}_I^T\frac{d\mathbf{K}_{D_I}}{d\rho_m}\mathbf{U}_R + \right.$$

$$i\boldsymbol{\lambda}_R^T\frac{d\mathbf{K}_{D_R}}{d\rho_m}\mathbf{U}_I - \boldsymbol{\lambda}_R^T\frac{d\mathbf{K}_{D_I}}{d\rho_m}\mathbf{U}_I - \boldsymbol{\lambda}_I^T\frac{d\mathbf{K}_{D_R}}{d\rho_m}\mathbf{U}_I - i\boldsymbol{\lambda}_I^T\frac{d\mathbf{K}_{D_I}}{d\rho_m}\mathbf{U}_I - $$

$$\boldsymbol{\lambda}_R^T\frac{d\mathbf{F}_R}{d\rho_m} - i\boldsymbol{\lambda}_R^T\frac{d\mathbf{F}_I}{d\rho_m} - i\boldsymbol{\lambda}_I^T\frac{d\mathbf{F}_R}{d\rho_m} + \boldsymbol{\lambda}_I^T\frac{d\mathbf{F}_I}{d\rho_m} + $$

$$\boldsymbol{\lambda}_R^T\frac{d\mathbf{K}_{D_R}}{d\rho_m}\mathbf{U}_R - i\boldsymbol{\lambda}_R^T\frac{d\mathbf{K}_{D_I}}{d\rho_m}\mathbf{U}_R - i\boldsymbol{\lambda}_I^T\frac{d\mathbf{K}_{D_R}}{d\rho_m}\mathbf{U}_R - \boldsymbol{\lambda}_I^T\frac{d\mathbf{K}_{D_I}}{d\rho_m}\mathbf{U}_R - $$

$$i\boldsymbol{\lambda}_R^T\frac{d\mathbf{K}_{D_R}}{d\rho_m}\mathbf{U}_I - \boldsymbol{\lambda}_R^T\frac{d\mathbf{K}_{D_I}}{d\rho_m}\mathbf{U}_I - \boldsymbol{\lambda}_I^T\frac{d\mathbf{K}_{D_R}}{d\rho_m}\mathbf{U}_I + i\boldsymbol{\lambda}_I^T\frac{d\mathbf{K}_{D_I}}{d\rho_m}\mathbf{U}_I - $$

$$\left.\boldsymbol{\lambda}_R^T\frac{d\mathbf{F}_R}{d\rho_m} + i\boldsymbol{\lambda}_R^T\frac{d\mathbf{F}_I}{d\rho_m} + i\boldsymbol{\lambda}_I^T\frac{d\mathbf{F}_R}{d\rho_m} + \boldsymbol{\lambda}_I^T\frac{d\mathbf{F}_I}{d\rho_m}\right). \tag{171}$$

hence, we observe that the terms containing i cancel each other out (resulting purely in real values). The remaining terms are

$$\boldsymbol{\lambda}_R^T\frac{d\mathbf{K}_{D_R}}{d\rho_m}\mathbf{U}_R - \boldsymbol{\lambda}_I^T\frac{d\mathbf{K}_{D_I}}{d\rho_m}\mathbf{U}_R - \boldsymbol{\lambda}_R^T\frac{d\mathbf{K}_{D_I}}{d\rho_m}\mathbf{U}_I - \boldsymbol{\lambda}_I^T\frac{d\mathbf{K}_{D_R}}{d\rho_m}\mathbf{U}_I + \boldsymbol{\lambda}_R^T\frac{d\mathbf{F}_R}{d\rho_m} + \boldsymbol{\lambda}_I^T\frac{d\mathbf{F}_I}{d\rho_m}, \tag{172}$$

that is equivalent to the operation

$$\Re\left(\boldsymbol{\lambda}^T\frac{d\mathbf{K}_D}{d\rho_m}\mathbf{U} + \boldsymbol{\lambda}^T\frac{d\mathbf{F}^*}{d\rho_m}\right). \tag{173}$$

Thus, we obtain

$$\frac{d\Phi}{d\rho_m} = \frac{\partial\mathscr{L}}{\partial\rho_m} + \Re\left(\boldsymbol{\lambda}^T\frac{d\mathbf{K}_D}{d\rho_m}\mathbf{U} + \boldsymbol{\lambda}^T\frac{d\mathbf{F}^*}{d\rho_m}\right). \tag{174}$$

APPENDIX C – TOPOLOGIES AND DISTRIBUTION OF STRESS CONSTRAINTS WITH ADAPTIVE VOLUME CONSTRAINT

Table 18 – Topologies and distribution of stress constrains with excitation frequency of 0 Hz.
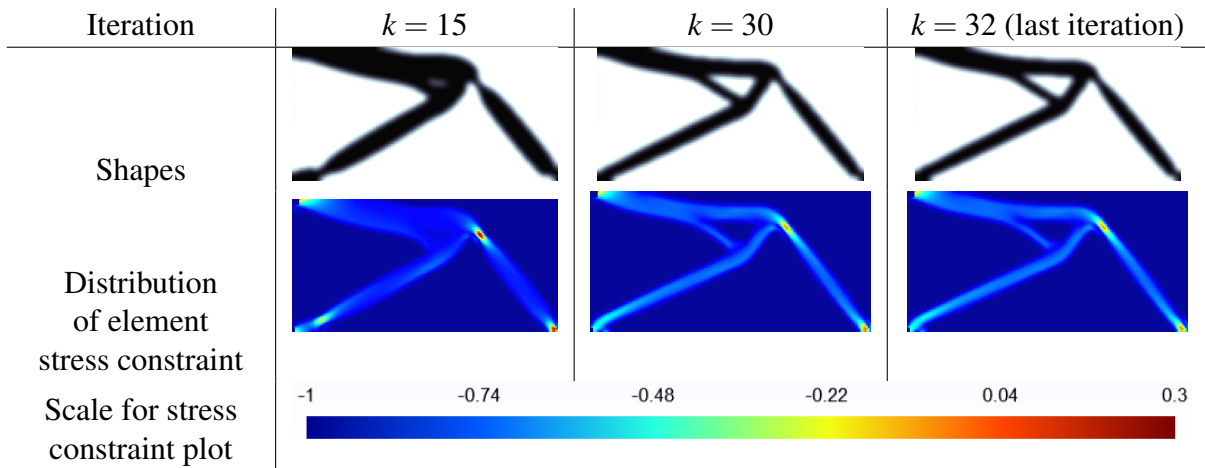

Table 19 – Topologies and distribution of stress constrains with excitation frequency of 100 Hz.
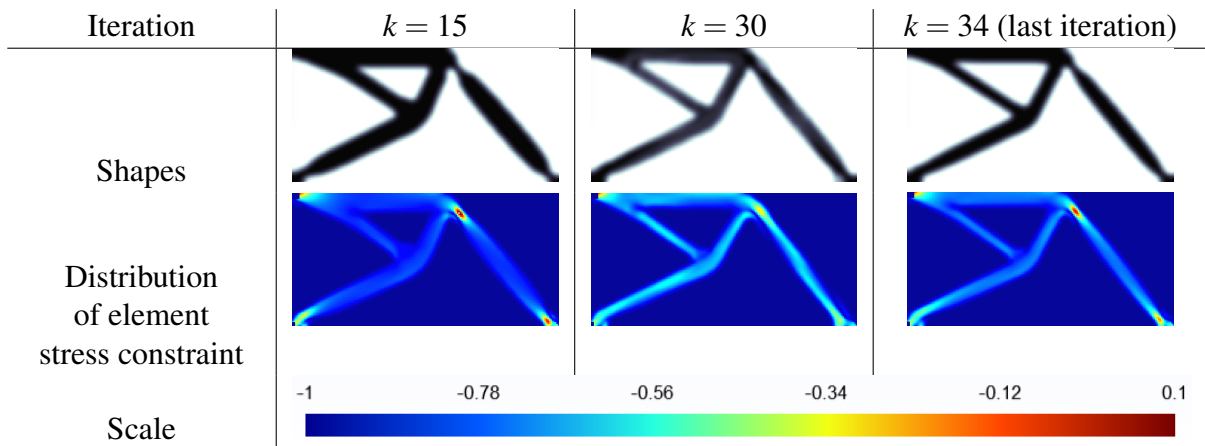

Table 20 – Topologies and distribution of stress constrains with excitation frequency of 200 Hz.
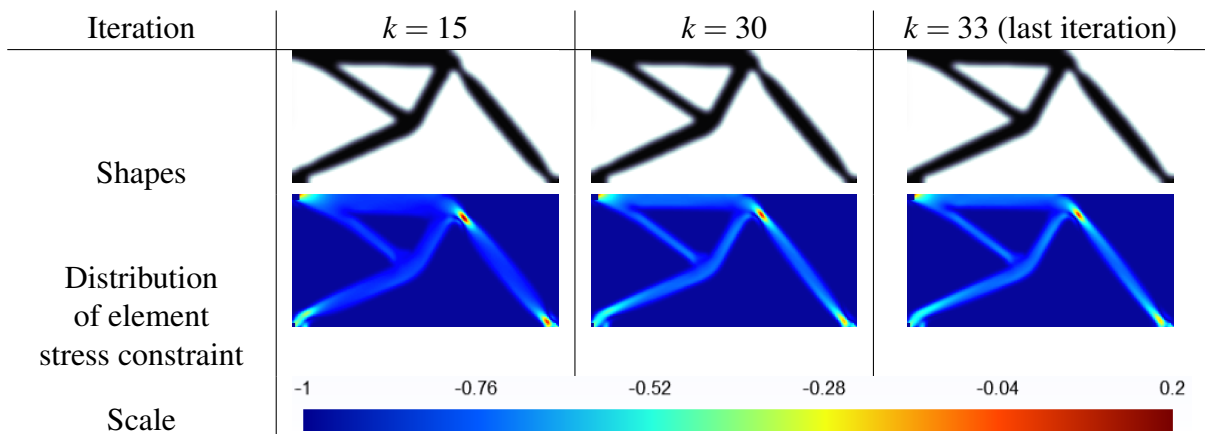
Table 21 – Topologies and distribution of stress constrains with excitation frequency of 300 Hz.
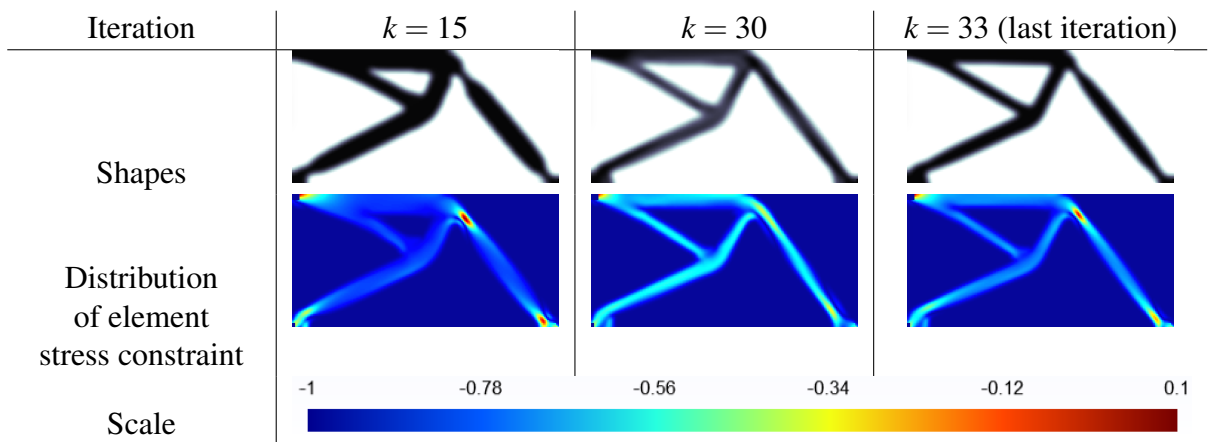
Iteration	$k = 15$	$k = 30$	$k = 33$ (last iteration)
Shapes			
Distribution of element stress constraint			
Scale			

Table 22 – Topologies and distribution of stress constrains with excitation frequency of 400 Hz.

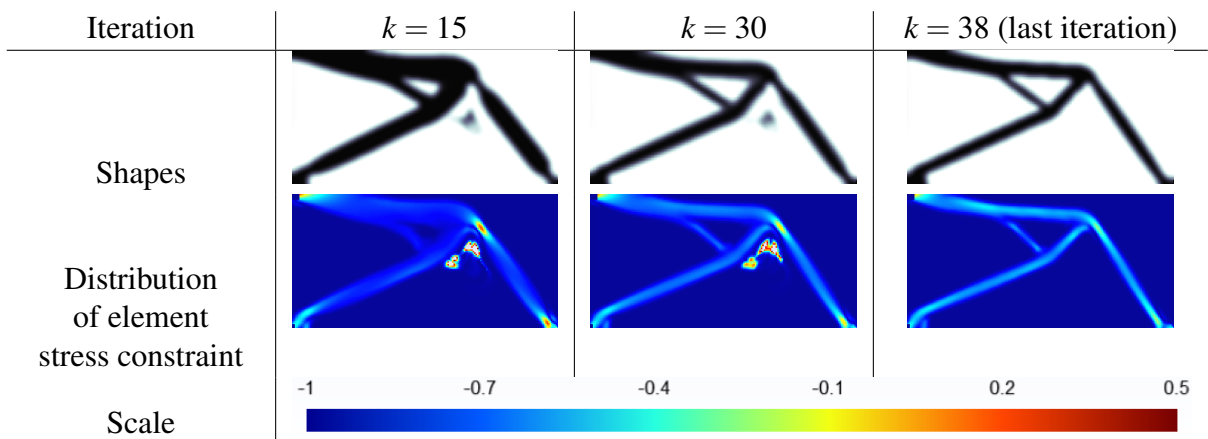| Iteration	$k = 15$	$k = 30$	$k = 38$ (last iteration)
Shapes			
Distribution of element stress constraint			
Scale			

Table 23 – Topologies and distribution of stress constrains with excitation frequency of 500 Hz and different volume constraints.

Iteration	$k = 15$	$k = 30$	$k = 33$ (last iteration)
Shapes			
Distribution of element stress constraint			
Scale			